Incorporation of Various Turbulence Models into a Flow Solver for Unstructured Grids

Armin Javadi

Submitted to the
Institute of Graduate Studies and Research
in partial fulfillment of the requirements for the Degree of

Master of Science
in
Mechanical Engineering

Eastern Mediterranean University
September 2014
Gazimağusa, North Cyprus

Approval of the Institute of Graduate Studies and Research

Prof. Dr. Elvan Yılmaz
Director

I certify that this thesis satisfies the requirements as a thesis for the degree of Master of Science in Mechanical Engineering.

Prof. Dr. Uğur Atikol
Chair, Department of Mechanical Engineering

We certify that we have read this thesis and that in our opinion it is fully adequate in scope and quality as a thesis for the degree of Master of Science in Mechanical Engineering.

Prof. Dr. Ibrahim Sezai
Supervisor

Examining Committee

1. Prof. Dr. Fuat Egelioğlu

2. Prof. Dr. Ibrahim Sezai

3. Assoc. Prof. Dr. Hasan Hacışevki

ABSTRACT

Considering two types of turbulent separating and impinging internal forced convection flows, the main goal of this study is to evaluate the performance of various two-equation turbulent models. For this aim, the most applied Low Reynolds Number $k-\varepsilon$ and $k-\omega$ models are implemented. A comparison of the appropriateness of different Low Reynolds $k-\varepsilon$ and $k-\omega$ models is carried out. Among the internal forced convection flow models, backward-facing step and confined impinging slot jet models are studied. Using different global parameters such as Nusselt number, skin friction coefficient and the position of the reattachment point, the results are compared with those of experimental data available in the relevant literature.

Governing partial differential equations are transformed to algebraic equations by finite-volume method over unstructured grids. Semi-Implicit Method for Pressure Linked Equations (SIMPLE) is used to solve pressure-velocity coupling fields. In addition Linear Upwind Difference (LUD) and Upwind differencing schemes are used to solve convection terms. The results indicate that Menter-SST $k-\omega$ model is superior among the implemented models.

Keywords: Turbulence modeling, Backward facing step, Impinging jet, Heat transfer, Nusselt number, Skin friction coefficient, Lam & Bremhorst, Wilcox, Menter SST.

ÖZ

Bu çalışmanın asıl amacı, farklı iki denklemli türbülans modellerinin performansını, türbülanslı zorlanmış konveksiyon akımları içeren uygulamalar için incelemektir. Bu amaç için, en fazla kullanılan düşük Reynolds sayılı $k-\varepsilon$ ve $k-\omega$ modelleri incelenmıştır. Farklı düşük Reynolds sayılı $k-\varepsilon$ ve $k-\omega$ modellerinin uygunluğunun belirlenmesi için bir karşılaştırma yapılmıştır. İç zorlanmış konveksiyon akım modeller arasında, geriye bakan basamaktan akım ile sınırlandırılmış jet akımı üzerinde çalışılmıştır. Elde edilen sonuçlar Nusselt sayısı, sürtünme katsayısı ve yatışma noktası konumunu kullanarak, literatürdeki mevcut deneysel verilerle karşılaştırılmıştır.

İlgili kısmi diferansiyel denklemler yapılandırılmamış ızgaralar üzerinde sonlu hacim yöntemi ile cebirsel denklemlere dönüştürülmüştür. Hız-basınç bağlantılı denklemler SIMPLE metodu kullanılarak çözülmüştür. Konveksiyon ile ilgili terimler lineer upwind farkı (LUD) yöntemi ile ayrıklaştırılmıştır. Sonuçlar, Menter-SST $k-\omega$ modelinin, uygulanan diğer modellerden daha üstün olduğunu göstermiştir.

Anahtar Kelimeler: Türbülans modelleme, Geri dönük adım, Çarpmalı jet, Isı transferi, Nusselt sayısı, Cilt sürtünme katsayısı, Lam ve Bremhorst, Wilcox, Menter-SST.

DEDICATION

To my beloved family

ACKNOWLEDGMENT

The road to completion of the following dissertation consumed so much time learning, coding and debugging which would be impossible to achieve the required results without continuous support of my dear supervisor Prof. Dr. Ibrahim Sezai to whom I would like to express my deepest gratitude. With his patience, enthusiasm, motivation, and immense knowledge he managed to veer my work in the right direction. This comes among the background that I am a novice researcher.

Besides my advisor, I would like to thank Prof. Dr. Fuat Egelioğlu and Assoc. Prof. Dr. Hasan Hacışevki as my thesis committee members for their insightful comments and participating in my defense.

My sincere thanks also goes to my best friends and colleagues, Nima Agh, Vahid Emad, who were always helping and cheering me up during our studies abroad.

Last but not least I would like to express my deepest gratitude to my family who encouraged me with their best wishes, supported me financially and spiritually throughout my studies; without their help and support I would not be at this point right now.

TABLE OF CONTENTS

LIST OF TABLES

LIST OF FIGURES

LIST OF SYMBOLS

C_p	Specific heat at constant pressure (J/kg.k)
C_μ, C_1, C_2	$k-\varepsilon$ Turbulence model constants
f_μ, f_1, f_2	$k-\varepsilon$ Turbulence model damping functions
h	heat transfer coefficient (W/m^2.k)
H	Height (m)
I	Turbulent intensity
k	Turbulent kinetic energy (m^2/s^2)
K	Thermal conductivity (W/m.k)
l	length scale of turbulence (m)
L	Length (m)
p	Pressure (Pa)
Pr	Prandtl number (ν/α)
q	Heat flux (W/m^2)
S	Source term
S_{ij}	Mean strain rate tensor
S_p, S_c	Linearized source term coefficients
T	Temperature
T_i	Turbulence intensity
u_i, u_j	Velocity component in x and y directions
U_i, U_j	Time-averaged velocity component in x and y direction
v_j	Jet velocity component in y direction

W	Slot width
y	minimum distance to the nearest wall
Greek symbols	
φ	General variable, u,v,p,T
β, β_0, β^*	$k-\omega$ Turbulence model constants
γ	$k-\omega$ Turbulence model constant
κ	Von Karman's constant, $\kappa = 0.41$
μ, μ_t	Laminar and turbulent eddy viscosities, $(kg/m.s)$
μ_{eff}	Effective turbulent eddy viscosity $\mu_{eff} = \mu + \mu_t$
ρ	Density (kg/m^3)
ε	Dissipation rate of turbulent kinetic energy (m^2/s^3)
σ	Molecular Prandtl number, $(\sigma = \mu C_p / k)$
$\sigma_t, \sigma_k, \sigma_\varepsilon, \sigma_\omega$	Turbulent Prandtl numbers
τ	Shear stress (N/m^2)
θ	Dimensionless temperature
ω	Specific dissipation rate (1/s)
Dimensionless group	
C_f	Skin friction coefficient
Re_W	Jet Reynolds number based on jet inlet velocity and hydraulic diameter $\mathrm{Re}_W = \rho v_j W / \mu$
Re_H	Backward facing step Reynolds number based on inlet velocity and step height $\mathrm{Re}_H = \rho v_i H / \mu$

$\mathrm{Re}_T, \mathrm{Re}_y$	$k-\varepsilon$ Model Turbulence Reynolds number
Nu	Nusselt number, Nu=hL/k
Subscripts	
avg	Average
i,j,k	indices for tensor notation
j	Jet inlet
imp	Impinging surface
in	inlet
ref	reference
wall	Wall boundary variable
Superscripts	
'	Fluctuation
cd	Cross derivative

Chapter 1

INTRODUCTION

1.1 Computational Fluid Dynamics

Computational fluid dynamics (CFD) is an area of fluid mechanics that deals with algorithms and numerical methods to solve and study the fluid flows. Computers are used to perform the calculations required to simulate the interaction of liquids and gases with surfaces defined by boundary conditions. With high-speed supercomputers, better solutions can be achieved. Ongoing research yields software that improves the speed and accuracy of complex simulation scenarios such as turbulent or transonic flows.

One of the advantages of CFD is that it is a very convincing, non-intrusive, virtual modeling technique with powerful visualization capabilities. Moreover, engineers can calculate the performance of a wide range of different system configurations on the computer without having to go the physical site, thereby saving much time and money.

CFD has seen dramatic development through the last several decades. This technology has been applied to various engineering applications such as oceanography, aircraft and automobile design, civil engineering and weather science. Today, the HVAC/IAQ industry is one such field that has initiated utilizing CFD techniques widely and rigorously in its design.

1.2 Turbulence modeling

In fluid dynamics, turbulence is a flow regime, characterized by chaotic property changes, which include momentum diffusion, convection and rapid variation of pressure and velocity in space and time.

Laminar flow is a condition where kinetic energy extinct due to the action of fluid molecular viscosity. Although there is no theorem relating the non-dimensional Reynolds number (*Re)* to turbulence, flows at *Re* greater than 5,000 are typically (but not necessarily) turbulent, while those at lower Reynolds numbers *Re*<5,000 usually remain laminar.

In turbulent flow, unsteady vortices appear on numerous scales and interact with each other. Drag increases due to boundary layer skin friction. The structure and location of boundary layer separation often change which sometimes reduces the overall drag. Although Reynolds number does not govern laminar-turbulent transition, it occurs if the density of the fluid is increased or the size of the object is gradually increased, or the viscosity of the fluid is decreased. Nobel Laureate Richard Feynman (2006) described turbulence as "the most important unsolved problem of classical physics."

Turbulence modeling is of the three crucial elements in Computational Fluid Dynamics (CFD). Accurate mathematical theories have been developed for the other key elements: algorithm development and grid generation. Since it is creating a mathematical model that approximates the physical behavior of turbulent flows, far

less precision is achieved in turbulence modeling. It is not a surprising incident since the objective has been to approximate very complicated phenomenon.

In the following sections, an overview of the subject is presented, covering the relevant studies of various flows.

1.3 Impinging Jet Flows

Impinging Jets (IJ) became a well-established object of investigation during recent years for their reason of increasing importance in both fundamental and applied fluid mechanics.

Impinging jets have been frequently used in industrial heat and mass transfer applications for improving or damping localized heat transfer rates where high rates of convective heat transfer is necessary. Also, it is very useful since it can be quickly moved to the location of interest with minimum cost. In a turbulent flow, thin boundary layers are located inside the stagnation zone, helping for further cooling, heating or drying processes.

Applications of such systems include tempering and melting of some non-ferrous metals and glass, Gas turbine components cooling and the outer wall of electronic equipment and combustors. Other applications of IJs are in freezing of tissue, surface coating, cleaning, metal cutting and forming, veneer, paper and film materials, fire testing, building materials and aircraft wings heating application. They also have been used in aerospace applications e.g. VTOL (Vertical Takeoffs and Landing) aircraft and lubrication. Effective designs can be achieved for engineering systems in such applications if the necessary knowledge for this kind of flow is well-understood.

Rapid cooling is mostly achieved by forced cooling systems. This method increases components safety and improves the efficiency of the components. Heat transfer coefficient (*h*-value) has to be the highest possible amount to reduce the cooling time. High transfer rates may further enhance by the use of through flow at the impingement surface, which may involve the application of suction beneath this surface. The combination of both impinging jets and through flow demonstrated for the drying of newsprint in a pilot plant and a full-size mill in Canada (Burgess et al. 1972a)

Recently, many researches have carried out experimental and numerical investigations of impinging jet under various conditions like Single or multiple jets with cross-sections of round, annulus or slot-jets with or without confinement surface, which depending on the application can be selected. Likewise, alternate designs for the flow of the spent fluid from the system after impingement provide a further design parameter.

To enhance the global transfer rates, often, banks of nozzles are used in the industry. To avoid high pressure in the impingement region, Low Reynolds Number (LRN) jets are preferred. Moreover, impinging jets offer the potential of fine and fast control of local transfer rates by varying the jet velocity, size of the nozzle opening and the impingement distance.

1.3.1 Description of impinging jets

'Impingement' means 'collision' that the coolant flow strikes into the target surface and creates a thin stationary boundary layer at the stagnant core for coolant hitting the hot surface without damping.

Impinging jet is a high-velocity coolant mass which is driven out from a slot or a different shape hole and impinges on the desired heat transfer surface; as a result, it gives a concentrated high-value rate of heat transfer between the fluid and the wall. (Figure 1.1)

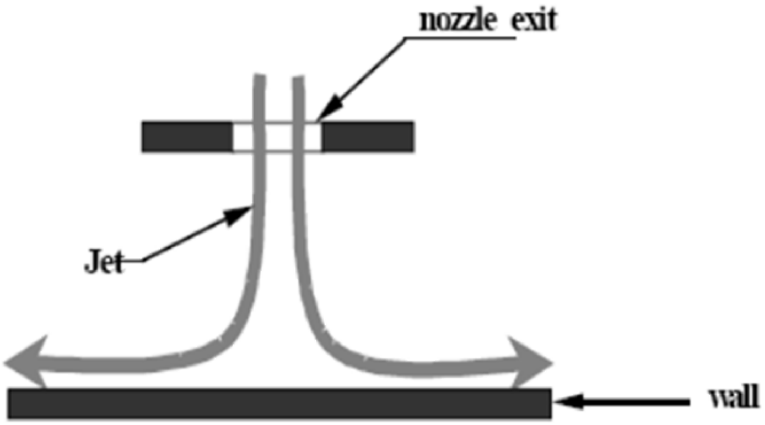

Figure 1.1: An impingement jet (Osama M. A. Al-aqal, 2003)

Although the geometry of jet impingement heat transfer is simple, physics of the flow is complex due to the shear-layer development at the free jet and wall boundaries, boundary-layer development at the impingement surface, and very high streamline curvature near the impingement location. Due to the complex interaction of the flow entrainment and vortex formation, flow separation along the surface, vortex breakdown and high streamline curvature, numerical modeling of jet impingement flow and heat transfer is very challenging. Consequently, the choice of the turbulence model is vital in the numerical analysis of the impinging jet heat transfer process.

Drying paper and textiles by jets involves the use of jets which are confined by a hood, which is also the nozzle plate. Geometric and process variables direct the design of such a confined IJ system. Geometric variables include the shape, size,

pitch, and spacing of Nozzles, the distance between the nozzle exit and the impingement surface, exhaust port location, turbulence generation and confinement type. Important process variables are jet Reynolds number (Re_w), jet to impingement surface (H/W), temperature differential (ΔT), jet humidity, speed of the impingement surface i.e. of the wet sheet relative to the jets and fluid properties.

1.3.2 Configuration of impinging jets

Two types of flow configurations are considered in impinging jets: submerged and free impinging jets (Figure 1.2). In submerged impinging jets, the exiting fluid from the nozzle is the same as the surrounding fluid; however, in free impinging jets the fluids are different.

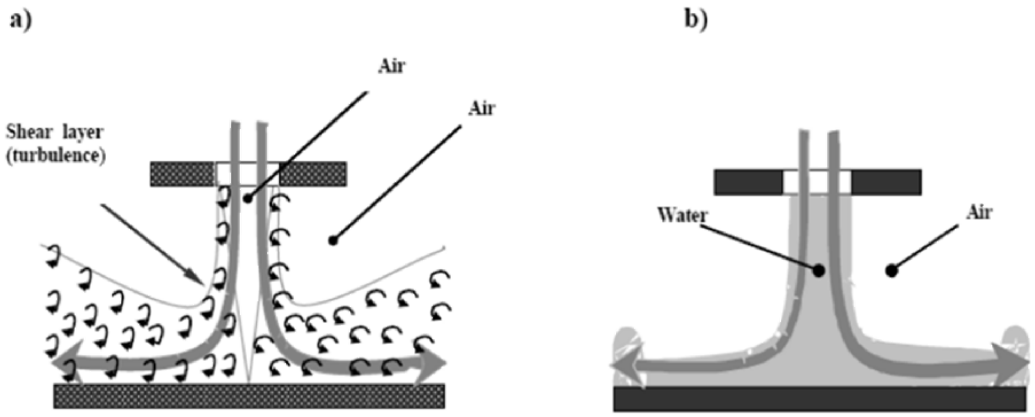

Figure 1.2: a) a submerged jet; b) a free impinging jet (Osama M. A. Al-aqal, 2003)

There are also different types of jets in regards of geometry: a planar case with jet exiting from a slot and an axisymmetric case with a round nozzle. Similarly, other geometries are also possible, like jets issuing from square, elliptical, rectangular nozzles or oblique jets. The nozzle geometry is believed to have a significant effect on the heat transfer to the IJs. Several studies attribute inconsistencies between reported data and their research to slight differences in the nozzle geometries. For this reason, the effect of nozzle geometry on heat transfer has attracted much

research. An important aspect of the nozzle geometry is confinement. An unconfined IJ is when a nozzle issuing a jet into an open space, though, it is called semi-confined in a case when a nozzle is machined into the plate. Confined jets that are popular in industrial applications cause the recalculation of the flow around the jet (Figure 1.3).

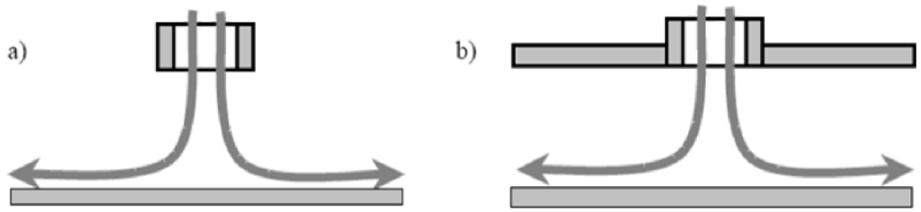

Figure 1.3: a) an unconfined impinging jet; b) a confined impinging jet (Osama M. A. Al-aqal, 2003)

1.3.3 Characteristic zones

The flow field can be separated in three characteristic regions (Figure 1.4): impingement, the free jet and wall jet regions. Furthermore, the free jet consists of two parts: the stagnation zone, jet zone, and the wall jet zone.

The jet zone is located directly underneath the nozzle. The fluid entering from the nozzle combines with the motionless surrounding fluid and creates a flow field. In most applications, the nozzle-to-plate distance is very small to develop the jet flow condition. A shear layer forms around the jet and its properties depend strongly on the nozzle type. The shear layer thickness becomes comparable with the jet diameter downstream, and the behavior of the layer changes significantly.

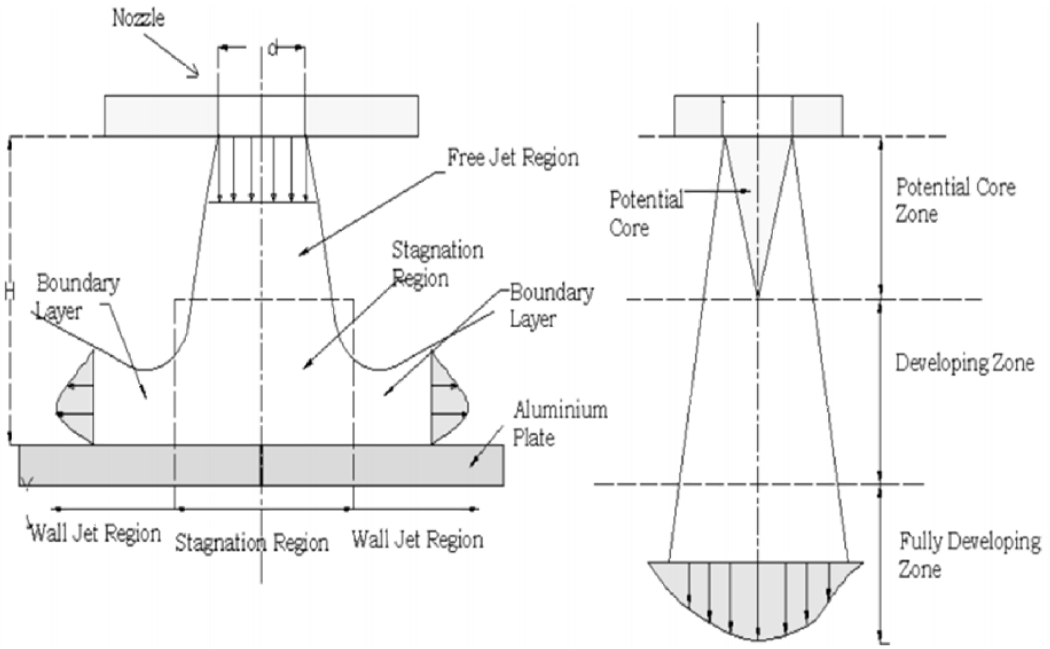

Figure 1.4: Characteristic zones in impinging jets (Osama M. A. Al-aqal, 2003)

Depending on Reynolds number and the type of the nozzle, the flow entering from the nozzle is either laminar or turbulent. The initial laminar flow experiences transition to turbulent flow. The transition begins in the unstable shear layer. The vortices are conveyed downstream by the flow. They lose symmetry, grow pair and finally break up in eddies, and turbulent flow is developed.

A potential core is formed in the center of the jet when the velocity profile in the nozzle exit is sufficiently flat. It is the flow region, in which the mean velocity is still the same as that at the nozzle exit. In this part, the fluid inside the core has not yet transferred its momentum to the surroundings. In the core region, stagnation Nusselt number increases slightly by increasing in H/W ratio for different values of Reynolds number. The potential core flow is inviscid that can be solved by used potential flow theories.

1.3.4 Heat and mass transfer

The impinging jet heat transfer distribution (quantified by the Nusselt number, Nu) is strongly influenced by the dynamics of the unsteady velocity field. The transfer of heat to the wall may be divided into contributions from (1)The mean flow, (2)chaotic structures (turbulence), (3)molecular diffusion and (4)coherent structures. If the flow is strongly convective (diffusion being negligible) heat behaves as a tracer. Under these circumstances, smoke visualizations can be used to characterize the dynamics of the flow. If diffusive effects need to be accounted for, i.e. diffusive time-scale comparable to the convective, smoke visualizations do not provide the correct picture of the flow. It is the case also in the wall region of convection dominated flows, where diffusive effects are dominant.

Promotion of vortex pairing resulted in shorter potential core and thus higher Nu for small H/D and lower Nu for large H/D. Suppression of vortex pairing gave the opposite effect. Furthermore, the secondary maximum (for H/D = 4) moved downstream as vortex pairing was suppressed.

As described before about Nu number, the geometrical parameter H/D is of great importance. If the spacing is greater than the length of the potential core, a fully developed jet will impinge onto the wall, i.e. turbulent jet impingement. Maximum heat transfer is achieved at the stagnation point Due to a high level of turbulent kinetic energy (k) within the center region of the axial jet. Downstream the stagnation point, Nu decreases monotonically. If the potential core is longer than H/D, the initial region of the wall jet becomes laminar-like, including small values of k. Thus, Nu experiences a local minimum at the stagnation point. As the laminar-like wall jet accelerates wall shear increases, due to thinning of the velocity boundary

layer, and a local maximum skin friction coefficient (C_f) is obtained at approximately r/D=1/2. The maximum in wall friction is accompanied by a maximum in wall heat transfer since the flow is laminar. Downstream this maximum, the Nu decreases. Furthermore, the ranges of scales grow large, and the wall jet becomes turbulent. This results in a second maximum of Nusselt number. In addition, the second maximum is influenced by large organized structures. Maximum stagnation heat transfer is attained when the H/D is about 6-8 nozzle diameters long.

A change in Reynolds number for small H/D has a greater influence on wall heat transfer than for large H/D. As shown by Angioletti et al. (2003) when Re was changed from 1500 to 4000 for H/D=4.5, stagnation point heat transfer increased by 15% and for H/D=2 resulted in a 56% increase. A second peak of Nu was only obtained for the higher Reynolds case.

In order to assess high wall heat transfer, it is important to pay attention to the inflow conditions (disturbances and mean profile) and the nozzle-to-plate spacing of the impinging jet. Further improvements of the wall heat transfer can be achieved by installing perforated plates prior to impingement or modification of the surface conditions. The shape of the outlet nozzle also has a major effect on the wall heat transfer, mostly for small H/D.

1.4 Separated flows

Flow separation and following reattachment of a sudden expansion or compression in the flow channels such as backward and forward facing steps, play an important role in the design of a variety of engineering applications where heating or cooling is required. These heat transfer applications appear in cooling systems for combustion

chambers, electronic equipment, energy systems equipment and chemical processes, cooling passages in turbine blades, high-performance heat exchangers and environmental control systems. Mixing of high and low energy fluid occurs in the reattached flow region of these devices that affect their heat transfer performance. For this reason, the problem of laminar and turbulent flow over forward and backward-facing step geometries in natural, forced, and mixed convection have been widely investigated numerically and experimentally.

Separation, recirculation and reattachment occur whenever a fast-flowing fluid is required to bypass an obstacle or when a confining wall undergoes a rapid change in orientation to form a strongly curved convex surface.

The objectives followed in different studies have varied significantly. However, the emphasis has been on understanding and capturing the separation process. Particularly on resolving recirculation zone, the structure of the separated shear layer it envelops, describing the location of reattachment, understanding and predicting the processes governing the flow recovery in the wake region following reattachment. All these issues are sufficiently important to be familiar to the most of practical and idealized laboratory flows, and therefore studies tended to concentrate only because of the availability of experimental data suitable for validation. For example, Kim et al. (1980), Eaton & Johnston (1980) and Driver & Seegmiller (1985) have obtained particularly widespread and precise experimental data for backward-facing step flow.

The discovery of boundary layer theory by Ludwig Prandtl in the early twentieth century was the beginning to the extensive research on separated flows. Separated flows are common in numerous engineering applications such as turbine and

compressor blades, buildings or cars, aircraft wings, diffusers and over airfoils, suddenly expanding pipes and combustors. Flow recirculation is also used as an efficient way to stabilize flames in premixed combustion. The characteristics of a separated flow have been studied for decades by experimentalists to understand the physics of the separated shear layers and their instability mechanisms. The instabilities in the free shear layers are the source to distinctly visible large coherent structures. The existence of coherent structures in almost every turbulent flow has been well documented, and this makes it even more interesting to study such separated shear flows.

Besides the academic interests, knowledge of separated flows can also be applied to many practical applications. Two of their main applications include the automobile and aircraft industries, which are developing fuel efficient designs to reduce consumption of the rapidly-depleting non-renewable resource and minimize greenhouse gas emission. In an aerodynamic perspective, drag is considered as one of the primary reason for inefficient fuel consumption. Studies by Roos and Kegelman (1986) demonstrated that by actively controlling the flow at separation, characteristics of the coherent structures can be modified and consequently alter the drag characteristics. These aspects of the flow make it necessary to understand the instabilities and characteristics of coherent structures for controlling flow dynamics to achieve significant drag reduction or lift enhancement. Apart from drag reduction, understanding the fluid-structure interactions of these separated shear layer instabilities can be very useful in controlling the noise and vibration characteristics of such flows.

1.4.1 Characteristics of separating flows

Among the internal separated flows, the backward-facing step (BFS) flow has received much attention over the past decades, and it has served as a test case for numerical methods. BFS flow was chosen because it has a simple geometry, but contains many flow regimes relevant to practical engineering. In addition, the BFS has perhaps the most extensive literature base of any benchmark flow, with several reliable datasets for comparison.

Flow over a backward-facing step produces recirculation zones where the fluid separates and forms vortices. For turbulent flow, the fluid separates at the step and reattaches downstream, as shown in Figure 1.5. Only a single recirculation zone develops for turbulent flow, and the reattachment point is believed to be independent of the Reynolds number and depend only on the ratio of inlet height to outlet height.

To simplify the flow characteristics, researchers conducted experiments on various geometries, which include fence, rib, suddenly expanding pipes, bluff body with a splitter plate or blunt leading edges, cavities, forward and backward facing steps.

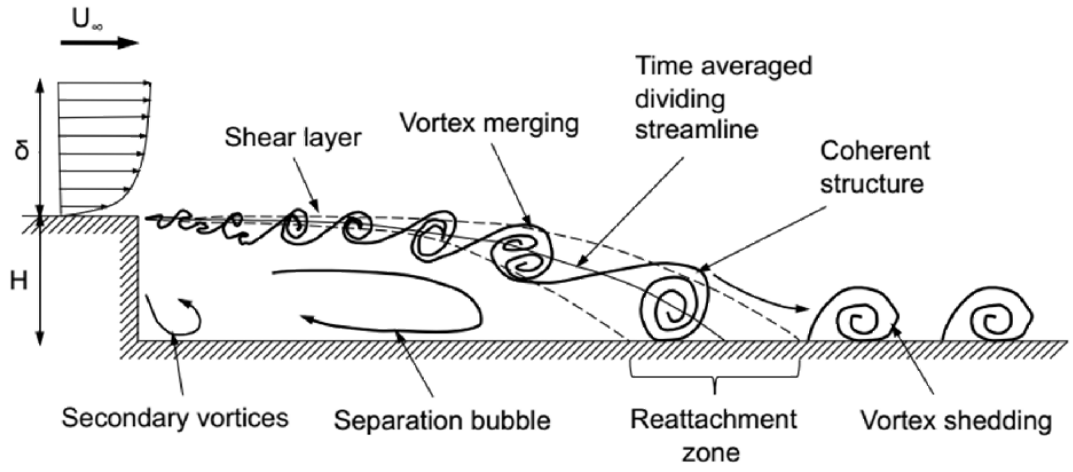

Figure 1.5: Flow characteristics behind a BFS (Driver et al. 1987)

The backward-facing step is considered as the ideal official separated flow geometry due to its single fixed separation point and the wake dynamics that are not affected by the downstream disturbances. A diagram of the wake characteristics behind a backward-facing step is shown in Figure 1.6.

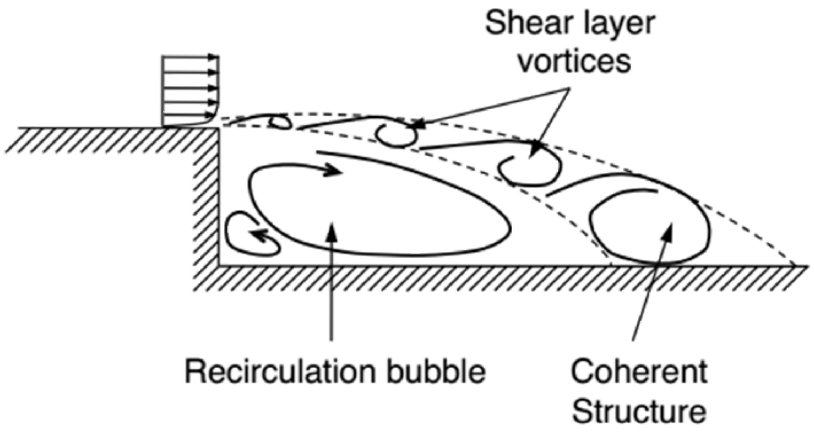

Figure 1.6: Backward-facing step flow features (J. Rajasekaran 2011)

The wake of a backward-facing step has unique features mainly in two regions: the free shear layer and low-velocity re-circulating bubble. Due to instabilities, the vortices in the shear layer roll up and pair with the adjacent vortices to form larger coherent structure. These vortices entrain fluid from the region below and trigger the recirculation. The free shear layer reattaches at the bottom wall due to adverse pressure gradient in the wake of the step.

In the separation of the flow, a curved and highly turbulent free shear layer composes first. In this layer, turbulence anisotropy will not normally be as large as in the boundary layer prior to separation, yet it can have a greater effect on mean flow characteristics than that in the parent boundary layer. Curvature tends to reduce the shear stress and hence the level of fluid entrainment into the shear layer with an

interaction that dictates the intensity of curvature in the shear layer and hence the reattachment position. Additionally, gradients of normal stresses contribute significantly to momentum transport. As the flow approaches reattachment, it is subjected to severe average strain, yet this can be shown not to contribute measurably to the turbulence-generation process; here too, normal-stress anisotropy plays a crucial role. Apart from provoking severe flow curvature, associated with the impingement process, the wall tends to attenuate turbulent fluctuations normal to it and to enhance wail-parallel components, the result being an unusually high level of normal-stress anisotropy. Finally, within the recirculation zone, curvature is high and affects the turbulence structure through the same mechanism identified above in relation to the free shear layer following separation.

1.5 Objective and Overview of the Thesis Work

The objective of the current study is to investigate the heat transfer and flow characteristics of impinging slot jet and backward-facing step flows by using various two-equation turbulence models.

The fluid-thermal and skin friction characteristics of the two cases of jet impingement and a backward-facing step model are investigated numerically, utilizing a finite volume method based FORTRAN unstructured code with a low Reynolds version of $k-\varepsilon$ and three versions of $k-\omega$ turbulence models. Through numerical analyses, a detailed description of two-dimensional fluid flow pattern is obtained. The distribution of Nusselt number and skin friction are calculated on the bottom surface and the reattachment points are calculated for the backward-facing step case in addition. These numerical results are validated with experimental data

obtained from literature. The effect of the Turbulence intensity variation on the heat transfer and flow characteristics of test cases is also reported.

Nusselt number and skin friction distribution are compared for two cases of impinging jets with different Reynolds numbers of 10,400 and 8,100. Skin friction and reattachment length are computed for a backward-facing step model with Reynolds number 28,000.

Chapter 2

LITERATURE SURVEY

2.1 Impinging slot jet flow

During the past years, various experimental and numerical models have been studied on jet impingement flow structure or heat and mass transfer procedure. Considerable effort has been devoted toward the development of efficient cooling schemes while attempting to understand the related flow and transfer mechanisms. Gardon and Akfirat (1966), Sparrow and Wong (1975) achieved the most wide-ranging experimental data on submerged, confined jet impingement. Their heat and mass transfer data for two-dimensional slot jets impinging normally on a flat plate of constant temperature are still commonly used. The primary concerns in the design of an impinging jets system are the regime of flow, flow rate, jet configuration, jet-to-target surface, spacing and any other geometric parameters. Gordon and Akfirat (1966) presented pressure and heat transfer coefficient distribution along the impingement solid surface for jet Reynolds number ranging from 450 up to more than 20,000 and with nozzle-to-wall spacing H/W from 2 to 32. Sparrow and Wong (1975) focused on laminar slot jets and reported mass transfer rates in addition to heat transfer coefficients. Both papers have demonstrated that transfer rates decrease as H/W increases and increase as Reynolds number increases, consistent with the understanding that transfer rates are enhanced when there is greater flux. Meanwhile, the later paper also concluded that velocity profile has a significant effect on the

transfer characteristics near the impinging region, although the total transfer coefficient along the wall is mostly unaltered.

Martin (1977) provided the first summary review of the studies on impinging gas jets. The report covered basic topics such as hydrodynamics of impingement flow, definition of local properties of jets, influences of boundary conditions, turbulence promotes and swirling jets. There were also brief comments on complex geometries and angled impingement in that paper. There have been many subsequent experimental results for either laminar or turbulent regular impinging jets. They reproduce the heat transfer rates reported by Gardon and Akfirat (1966). It is observed that transfer coefficients show a secondary local peak at some distance downstream the stagnation point by the time the Reynolds number is greater than a certain value, typically 900, in comparison with the monotonic distribution along the wall for lower Reynolds jet flow. Stevens and Webb (1991) have reported this secondary peak at high Re as well. Downs and James (1987) has presented a detailed literature survey of impingement jet experiments, in which research findings related to jet impingement characteristics were summarized and significant physical, as well as geometric parameters examined in earlier studies, were classified and listed.

Aside from the experimental studies, a number of efforts have also been devoted to numerical computation of jet impingement. The essential tasks have been to predict jet impingement and the induced recirculation flow structure: and to calculate the heat transfer rate along the impingement wall. Varieties of schemes have been implemented for turbulent and laminar jet flow. Primary studies have been concerned with normal impingement, either with or without confinement. Looney and Walsh (1984) have investigated mean-flow and turbulent characteristics of free and

impinging jet flows numerically by solving Navier-Stokes equations first two-dimensional model of laminar and turbulent IJ for altered ratios (H/W) of the nozzle height (H) to nozzle width (W). A correlation between stagnation Nusselt number, Reynolds number and H/W has been proposed for stagnation zone heat transfer.

Polat et al. (1989) have carried out a detailed review of the numerical methods and computational results for flow and heat transfer under jet impingement on flat surfaces. Mostly, the computations can capture some of the measured quantities reasonably well, such as the distribution of pressure and Nusselt number Nu nearby the impingement region and the velocity profiles along the jet axis. However, unresolved issues remain. Only a couple of studies report computations for large nozzle-to-wall spacing, either clue to numerical instability or the steady flow assumption; numerical results never reveal the secondary peak of Nusselt number along the wall as reported in experiments at higher jet Reynolds numbers. This later problem still exists even when different turbulence models are implemented for turbulent jet flow. In addition, since there is a lack of flow field measurements inside a jet impingement system sometimes numerical computations from various studies present contradictory predictions particularly about the secondary recirculation bubble off the impingement wall downstream of the primary recirculating vortex. According to Polat et al. (1989), a recirculating bubble may act as an insulator between the jet flow and the plate, therefore causing a drastic reduction in heat transfer. Meanwhile, others argued that the local hump corresponds to the point at which turbulence has been fully developed (Liu et al. 1991), or it is attributed to the transition from a laminar to turbulent boundary layer in the parallel flow region along the plate.

Polat et al. (1989) gave a comprehensive literature review in experimental and numerical aspects of impingement heat transfer, highlighting that the standard $k-\varepsilon$ model with different wall functions fails to predict the stagnation heat transfer accurately.

Yin et al. (1990) developed a model that was originally based on low-Reynolds number $k-\varepsilon$ model to predict turbulent natural convection boundary layers. In the model, they divided the velocity into two components, i.e., a forced convection component and a buoyancy-influenced component. A two-equation model for the energy equation by Nagano and Kim (1988) has been used for the calculation of the temperature field. They found that the combination of the modified low-Reynolds number $k-\varepsilon$ and the two-equation model for the energy equation be the best way to predict natural convection.

Heyrichs. K., Pollard. A (1995) have investigated heat transfer in separating and impinging turbulent flows. The performance of $k-\varepsilon$ and $k-\omega$ turbulence models is evaluated, especially the low Reynolds number regions. In the $k-\varepsilon$ model, six low Reynolds number and three wall functions assessed. The results indicate that the $k-\omega$ model is numerically is easy to implement and reveals better performance for prediction of convection heat transfer in complex turbulent flows.

Hosseinalipour and Mujumdar (1995) performed a comparative assessment of various turbulent models for a confined impingement configuration with an aspect ratio of H/W=1.5. Concluded that the predicted local Nusselt numbers achieved using low Reynolds number $k-\varepsilon$ models in the stagnation region are in good

agreement with the experimental data, but the stagnation zone is difficult to predict accurately with any $k-\varepsilon$ models.

Behnia, M, et al. (1998) have studied on the problem of cooling of a heated plate by an axisymmetric isothermal fully developed turbulent jet. Computations were performed with the normal-velocity relaxation turbulence model (v^2-f model). Local heat transfer predictions were compared to the available experimental data. Computations also performed with the widely used $k-\varepsilon$ model for comparison. The v^2-f heat transfer predictions are in excellent agreement with the experiments whereas the $k-\varepsilon$ model does not adequately resolve the flow features significantly over-predicts the rate of heat transfer and produces physically unrealistic behaviors.

Behnia, M. et al. (1999) have studied on an elliptic relaxation turbulence model (v^2-f model) to simulate the flow and heat transfer in circular confined and unconfined impinging jet configurations. The model has been validated against available experimental data sets. Results have been obtained for a range of jet Reynolds numbers and jet-to-target distances. The effect of confinement on the local heat transfer behavior has been determined. It has been shown that confinement leads to a decrease in the average heat transfer rates, but the local stagnation heat transfer coefficient is unchanged. The effect of confinement is only significant in very low nozzle-to-plate distances (H/D<0.25). In contrast, the flow characteristic in the nozzle strongly affects the heat transfer rate, especially in the stagnation region. Quantitative (up to 30% difference) and qualitative differences have been obtained when different nozzle velocity profiles were used.

Sezai and Mohamad (1999) have studied the flow and heat transfer characteristics of impinging laminar slot jets issuing from rectangular slots of different aspect ratios numerically through the solution of three-dimensional Navier-Stokes equations in steady state. Furthermore, Soong et al. (1999) have performed time-dependent computations to investigate the flow structure, bifurcation and flow instability involved in confined plate twin-jet flows numerically.

Shi et al. (2002) systematically studied the effects of turbulence models, near wall treatments, turbulent intensity, jet Reynolds number and boundary conditions on the heat transfer under a turbulent slot using the standard $k-\varepsilon$ and RSM (Reynolds Stress Model) models. Their results indicate that both standard $k-\varepsilon$ and RSM models predict the heat transfer rates inadequately, especially for low H/W aspect ratios. For wall-bounded flows, large gradients of velocity, temperature and turbulent scalar quantities exist in the near wall region and thus to incorporate the viscous effects it is necessary to integrate equations through the viscous sublayer using finer grids with the aid of turbulence models.

S.J. Wang, A.S. Mujumdar (2005) have compared Five versions of low Reynolds number $k-\varepsilon$ models with the available experimental data for the prediction of the heat transfer under a two- dimensional turbulent slot. A correction model proposed which was named as "Yap correction" for reducing the turbulence length scale in the near wall region. This correction was tested with low Reynolds number $k-\varepsilon$ models and found that for most of the models it is capable of improving the predicted local Nusselt number in a good agreement with the experimental data in wall jet and stagnation regions. Effects of the magnitudes of the turbulence model constants were

also carried out for two low Reynolds number $k-\varepsilon$ models. They found that the set of model constants identical to those in the high Reynolds number $k-\varepsilon$ model performs better than the original ones for jet impingement configurations.

M. A. R. Sharif and K. K. Mothe (2009) have evaluated the performance of several turbulence models in prediction of impingement slot jet onto flat and concave cylindrical surfaces, against experimental data. The accuracy of heat transfer prediction near the impingement region depends greatly on the jet-to-target surface distance. When the impingement surface is within the potential core of the jet, the turbulence models grossly overpredict the Nusselt number in the impingement region, but in the wall jet region the Nusselt number prediction is fairly accurate. The two-layer near-wall treatment significantly improves the Nusselt number prediction accuracy compared to the equilibrium wall function approach. Overall, M. A. R. Sharif and K. K. Mothe (2009) concluded that the RNG $k-\varepsilon$ model with the two-layer near-wall treatment and the Menter-SST $k-\omega$ model predict the Nusselt number distribution better than the other models for the flat plate as well as for the concave surface impingement cases.

2.2 Backward facing step flow

The BFS flow has been studied intensively for at least four decades and is possibly the most popular benchmark flow. Literature is extensive, with contributions from experimental, theoretical and computational fluid dynamics. Eaton and Johnston (1981) explain that the BFS is popular because it is the "simplest reattaching flow with a region of separation and reversed flow". Despite this geometric simplicity, the BFS flow is complex and composed of many regions of different flow regimes that make for a thorough test of PIV and CFD techniques, particularly turbulence models.

Thangam and Hur (1991) note that "the BFS is often used for analyzing the efficiency of CFD algorithms and turbulence models, since it embodies several crucial aspects of turbulent separated flows".

Understanding of the BFS flow has improved with advances in fluid measurement technology. The recirculating and highly unsteady BFS flow presents a considerable challenge for most experimental techniques (Adams and Eaton 1988). Early studies relied on flow visualization methods, such as oil, smoke, ink or tufts (Armaly et al. 1983, Kim et al. 1978) and experiments were limited to low speed laminar regions. A few studies investigated the turbulent BFS, but measurements were limited to low turbulence regions outside of the recirculation region (Kline 1959, Kim et al. 1980, Bradshaw and Wong 1972). PIV has recently revealed the global BFS flow, at higher resolution than previously possible (Scarano and Riethmuller 1999, Shen and Ma 1996, Kasagi and Matsunaga 1995).

Reliable CFD routines, such as Large Eddy Simulation (LES) and Direct Numerical Simulation (DNS) are also contributing to BFS research. They are revealing the behavior of the complex, unsteady, 3D BFS flow structures (Le et al. 1997, Kobayashi et al. 1992). BFS knowledge is well-summarized in the reviews by Eaton and Johnston 1981, Eaton and Johnston 1980, Adams et al. 1984, Simpson 1996, Kim et al. 1978.

A detailed experimental study for an expansion ratio close to 2 and a downstream aspect ratio close to 18, also raising the question of three-dimensionality of step flow, was conducted by Armaly et al. (1983). Three dimensionality manifests itself in a discrepancy in primary recirculation zone length between experiments and two-

dimensional simulations for Reynolds numbers above Re ≈ 400. As, at this Reynolds number range, a secondary recirculation region appears at the channel upper wall, Armaly et al. (1983) suggested that the discrepancy in primary recirculation zone length could be attributed to the secondary recirculation region destroying the two-dimensional character of the flow.

Numerical simulation studies of step flow including sidewalls started about a decade ago (see Jiang et al. 1993, and references therein). More recently, Williams & Baker (1997) performed three-dimensional numerical simulations of laminar flow over a step, with sidewalls, for the same geometry as in Armaly et al. (1983) and for Reynolds numbers up to 800. They found that the presence of sidewalls results in the formation of a wall-jet, located at the channel lower wall and pointing from the sidewall towards the channel mid-plane. This wall-jet is already present at low Reynolds numbers (Re = 100), its strength increasing with Reynolds number. Chiang & Sheu (1999) performed detailed three-dimensional simulations of laminar flow, for the same expansion ratio as Armaly et al. (1983), for various Reynolds number and aspect ratio values. They found that at Re = 800, the flow structure in the channel mid-plane is similar to that of two-dimensional flow only for outflow channel aspect ratios of the order of 50 and higher. Chiang & Sheu (1999) also gave a discussion of streamwise vortex development. Barkley et al. (2002) have shown that, for an expansion ratio of 2 and in the absence of sidewalls, the flow structure becomes three-dimensional (and steady) around Re=1000, due to a three-dimensional instability. Flat streamwise rolls lying within the primary recirculation zone characterize the critical eigenmode responsible for this three-dimensional transition.

Thangam & Knight (1989) investigated the influence of the step expansion ratio on the reattachment length of laminar flow, $33 \leq Re \leq 600$. The expansion ratios considered were in the range $1.33 \leq r \leq 4$, where r is defined as the ratio of the outflow channel height to the height of the inlet channel. It was found that the non-dimensional (normalized by the step height H) reattachment length increases at increasing expansion ratio. For Re=200, an approximately 65% longer reattachment length was reported for r=4, compared to r=1.49. Interestingly enough, the dependence of normalized reattachment length on expansion ratio followed the opposite trend in the turbulent regime. This was observed in the experiments of Ötügen (1991), who conducted experiments in closed backward-facing step geometry with varying expansion ratios, while keeping the inflow conditions unaltered. The Reynolds number was 16,600 based on free stream velocity and inflow channel height. Most measurements were done at expansion ratios of r=1.5, 2.0, and 3.13. Ötügen (1991) observed an increase in turbulence intensity at increasing expansion ratio; thus, Ötügen concluded that the observed decrease in normalized reattachment length with expansion ratio is the consequence of higher turbulence intensities. Based on a review of the literature on turbulent flow over a step, Eaton & Johnston (1981) summarized five parameters which, to a large extent, define the flow structure downstream of the sudden expansion: (i)freestream turbulence level, (ii)aspect ratio of the channel, (iii)initial boundary layer state, (iv)pressure gradient and (v)initial boundary layer thickness. Isomoto & Honami (1989) have since confirmed a strong negative correlation of the recirculation region length with maximum turbulence intensity near the wall at separation. For the fully turbulent flow, Papadopoulos & Ötügen (1995) report an aspect ratio (AR) invariant reattachment length for AR>10. However, spanwise-dependent flow in terms of

velocity and wall pressure was observed downstream of reattachment, even for larger aspect ratios. This observation was attributed to the presence of a streamwise vortex close to each channel sidewall.

Several experimental studies have been reported in the last decades. For example, those carried out by Eaton and Johnston (1980), Vogel and Eaton (1985), Kim et al. (1980) and Driver and Seegmiller (1985). Most of them have then been numerically simulated. For example, Heyerichs and Pollard (1996) studied the configuration of Vogel and Eaton (1985), and presented results for global parameters i.e. Nusselt and Stanton number for several linear eddy viscosity models. Park and Sung (1995) applied a new model to this case and compared mean velocity, normal turbulent stresses at two positions and skin friction coefficient along step wall. Thangam and Speziale (1992) used the experimental data by Kim et al. (1980) to evaluate standard $k-\varepsilon$ and (Nonlinear Eddy Viscosity Model) NLEVM models with different approaches near solid walls. They presented results for mean velocity, shear stress and global variables.

Eaton & Johnston (1980), Westphal et al. (1984), Adams & Johnston (1988), and Driver & Seegmiller (1985) all measured the skin friction coefficient C_f on the step wall. Although there is a large variation in Reynolds number and expansion ratio among these experiments, they all reported a high level of skin friction magnitude $\left|C_f\right|$ in the recirculation region. The present study showed that the peak value of $\left|C_f\right|$ can be significantly higher at low Reynolds numbers. This finding prompted a companion experimental investigation at the same Reynolds number and expansion ratio as the present numerical study (Jovic & Driver 1994).

Kuehn (1980), Durst & Tropea (1981), Ötügen (1991), and Ra & Chang (1990) studied the effects of expansion ratio (ER) on the reattachment length. The reattachment length was found to increase with ER in these studies. Armaly et al. (1983) studied the effect of Reynolds number on the reattachment length. They found that reattachment length increased with Reynolds number up to $\mathrm{Re}_H \approx 1200$ (Reynolds number based on step height and inlet free-stream velocity U_0), then decreased in the transitional range $1200 < \mathrm{Re}_H < 6600$, and remained relatively constant when the flow became fully turbulent at $\mathrm{Re}_H > 6600$. Their findings agreed well with experiments by Durst & Tropea (1981) and Sinha, Gupta & Oberai (1981). Other parameters affecting reattachment length were also investigated: upstream boundary layer profile (Adams et al. 1984), inlet turbulence intensity (Isomoto & Honami 1989), and downstream duct angle (Westphal el al. 1984).

Investigations of the flow velocity profiles and turbulence intensities in the recovery region were conducted by Bradshaw & Wong (1972), Kim, Kline & Johnston (1978), Westphal et al.(1984), and Adams et al.(1984). These experiments showed that, even though the mean streamwise velocity profiles were not fully recovered at more than 50 step heights behind the separation, a full recovery of the log-law profile near the wall was attained as early as 6 step heights after the reattachment.

Several numerical simulations of the backward-facing step flow were also conducted, but largely confined to two-dimensional calculations (Armaly et al. 1983; Durst & Pereira 1988; Kaiktsis et al. 1991). Three-dimensional calculations were also performed by Kaiktsis et al. (1991) and by Friedrich & Arnal (1990) using the large-eddy simulation technique.

Chapter 3

UNSTRUCTURED DISCRETIZATION OF NAVIER-STOKES EQUATION

3.1 Introduction

Many engineering problems involve complex geometries that do not fit exactly in Cartesian co-ordinates or one of the other systems. When the flow boundary does not coincide with the co-ordinate lines of a structured grid, it could be proceeded by approximating the geometry. For most of the complex geometries, it may be required to use many cells, and the logical extension of this idea is the unstructured grid. This gives infinite geometric flexibility and uses the computing resources efficiently for complex flows, so this technique is now widely used in industrial CFD. An unstructured grid can be thought of as a limiting case of a multi-block grid where each individual cell is treated as a block. The advantage of such an arrangement is that the grid imposes no implicit structure of co-ordinate lines – hence the name unstructured – and the mesh can be easily concentrated where necessary without wasting computer storage. Moreover, control volumes may have different shapes, and there are no restrictions on the number of neighboring cells. In practical CFD, triangles or quadrilaterals are most often used for 2D problems and tetrahedral or hexahedral elements in 3D ones. Figure 3.1 shows a triangular unstructured mesh for the calculation of a 2D flow over an airfoil.

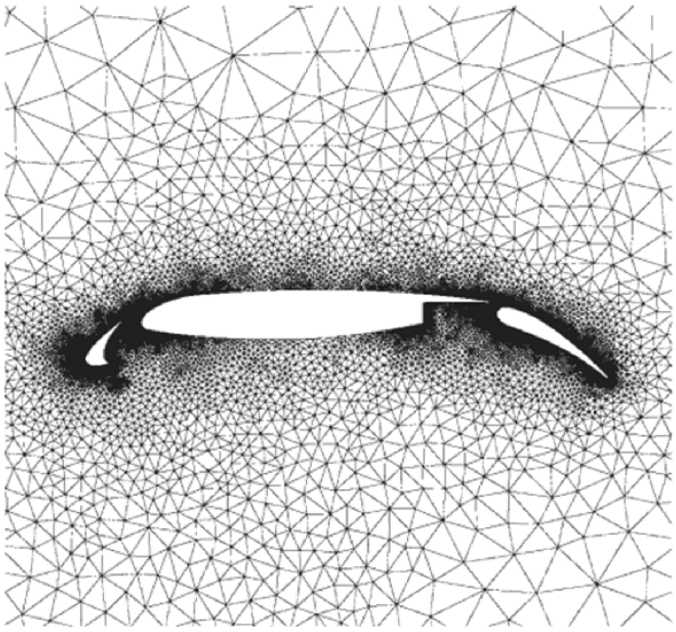

Figure 3.1: A triangular grid for a three-element airfoil (Versteeg 2007)

The best advantage of the unstructured mesh is that it allows the calculation of flows in or around geometrical features of arbitrary complexity without spending a long time on mesh generation and mapping. Grid generation is fairly straightforward (especially with triangular and tetrahedral grids), and automatic generation techniques, originally developed for finite element methods, are now widely available. Furthermore, mesh refinement and adaption (semi-automatic mesh refinement to improve resolution in regions with large gradients) are much easier in unstructured meshes. In the following sections, the unstructured methodology is explored in more detail as it is now the most popular technique and included in all commercial CFD codes on the market today.

3.2 Discretization in unstructured grids

Unstructured grids are the most general form of grid arrangement for most complex geometries. In the cell-centered method the nodes are placed at the centroid of the control volume as shown in Figure 3.2a. In the vertex-centered method, the nodes are placed on the vertices of the grid. This is followed by a process known as median-

dual tessellation, whereby sub-volumes are formed by joining centroids of the elements and midpoints of the edges, as illustrated in Figure 3.2b. The sub-volume surrounding a node then forms the control volume for discretization. Both cell-centered and vertex-centered methods are used in practice. Developing the ideas of discretization in unstructured grids for the cell-centered method, which is simpler to understand, and, since a control volume always has more vertices than centroids, it has slightly lower storage requirements than the vertex-centered method.

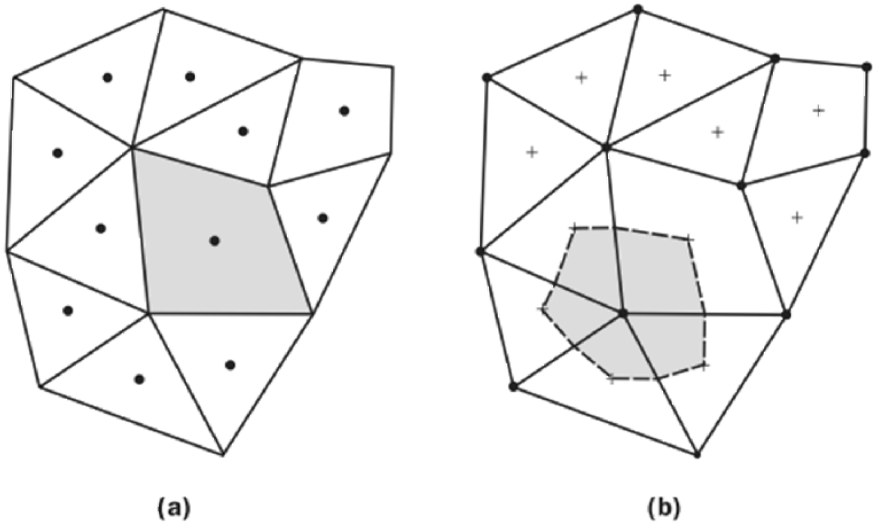

Figure 3.2: Control volume construction in 2D unstructured meshes:
(a) cell-centered control volumes; (b) vertex-based control volumes

A brief summary of the discretization process used in the original code is given below. Detailed information can be found in the lecture notes of I. Sezai (2013).

The discretization in unstructured meshes can be developed from the general steady state transport equation which is given by:

$$div(\rho\phi\mathbf{v}) = div(\Gamma\, grad\, \phi) + s_\phi + s_\phi^{cd} \tag{2.1}$$

where s_ϕ is the source term due to body forces and pressure for the case of momentum equations, or energy generation per unit volume in the case of energy equation. In general, it can be written in linearized form as

$$s_\phi = s_c^{eqn} + s_p^{eqn}\phi \tag{2.2}$$

The term s_ϕ^{cd} is the diffusion source terms involving cross derivatives in the momentum equations. The cross derivative source terms s_ϕ^{cd} are zero for incompressible fluids if μ is constant.

Integrating and applying the Gauss' divergence theorem gives

$$\underbrace{\oint_A (\rho\phi\mathbf{v})\cdot d\mathbf{A}}_{\text{Convection term}} = \underbrace{\oint_A (\Gamma\, grad\,\phi)\cdot d\mathbf{A}}_{\text{Diffusion term}} + \underbrace{\int_{CV} s_\phi dV}_{\text{Source term}} + \underbrace{\oint_A (\mu grad\mathbf{u}\cdot\mathbf{e}_i)\cdot\mathbf{n}dA}_{\text{Cross derivative diffusion term}} \tag{2.3}$$

where $\mathbf{e}_i$ is the unit vector in direction i, ($\mathbf{e}_x$, $\mathbf{e}_y$, $\mathbf{e}_z$ for x-, y- and z-momentum equations, respectively).

Approximating the surface integrals in terms of summations gives

$$\underbrace{\sum_{f=1}^{n_{fP}} \dot{m}_f\phi_f}_{\text{Convection term}} - \underbrace{\sum_{f=nb(P)} \Gamma_f \nabla\phi_f.\mathbf{A}_f}_{\text{Diffusion term}} = \underbrace{\int_{CV} s_\phi dV}_{\text{Source term}} + S_\phi^{cd} \tag{2.4}$$

Or

$$\sum_{f=1}^{n_{fP}} J_f^{conv} + \sum_{f=nb(P)} J_f^{dif} = \int_{CV} s_\phi dV + S_\phi^{cd} \tag{2.5}$$

where the cross derivative diffusion source term S_ϕ^{cd} are:

$$\begin{aligned}
S_u^{cd} &= \int_S (\mu\nabla^x\mathbf{u})\cdot\mathbf{n}dA \approx \sum_{f=nb(P)} (\mu\nabla^x u)_f A_f^x + (\mu\nabla^x v)_f A_f^y + (\mu\nabla^x w)_f A_f^z \\
S_v^{cd} &= \int_S (\mu\nabla^y\mathbf{u})\cdot\mathbf{n}dA \approx \sum_{f=nb(P)} (\mu\nabla^y u)_f A_f^x + (\mu\nabla^y v)_f A_f^y + (\mu\nabla^y w)_f A_f^z \\
S_w^{cd} &= \int_S (\mu\nabla^z\mathbf{u})\cdot\mathbf{n}dA \approx \sum_{f=nb(P)} (\mu\nabla^z u)_f A_f^x + (\mu\nabla^z v)_f A_f^y + (\mu\nabla^z w)_f A_f^z
\end{aligned} \tag{2.6}$$

where, A_f^x, A_f^y and A_f^z are the *x*, *y* and *z*- components of the surface area vector. The convective flux at the cell faces $J_f^{conv} = \dot{m}_f \phi_f$ can be written as the sum of the upwind value and other higher order terms (i.e. LUD) which are evaluated at the previous iteration *n*–1 as

$$J_f^{conv} = \dot{m}_f \phi_f = \dot{m}_f \left[\phi_f^U + (\phi_f^H - \phi_f^U)^{n-1} \right] \tag{2.7}$$

where ϕ_f^H is the face value of ϕ obtained from a higher order method and $\dot{m}_f \phi_f^U$ is found from upwind method expressed in a compact form as:

$$\dot{m}_f \phi_f^U = \max(\dot{m}_f, 0.)\phi_P + \min(\dot{m}_f, 0.)\phi_N \tag{2.8}$$

Substituting $\dot{m}_f \phi_f^U$ from Equation (2.8) into Equation (2.7)

$$\begin{aligned} J_f^{conv} &= \max(\dot{m}_f, 0.)\phi_P + \min(\dot{m}_f, 0.)\phi_N \\ &+ \left[\dot{m}_f \phi_f^H - \max(\dot{m}_f, 0.)\phi_P - \min(\dot{m}_f, 0.)\phi_N \right]^{old} \end{aligned} \tag{2.9}$$

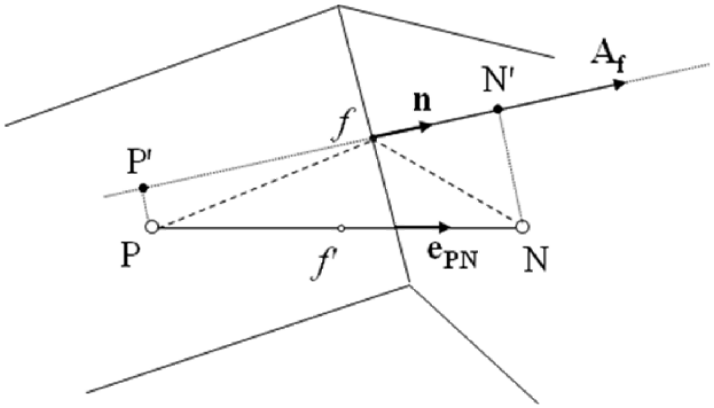

Figure 3.3: Diffusion flux across a surface (Sezai I. 2013)

The calculation of the diffusion flux at an internal face is given by

$$J_f^{dif} = -\Gamma_f \nabla \phi_f . \mathbf{A}_f = \underbrace{-\Gamma_f \frac{\phi_N - \phi_P}{d_{PN}} A_f^d}_{\text{orthogonal term}} \underbrace{- \Gamma_f \frac{\nabla \phi_N \cdot \mathbf{NN'} - \nabla \phi_P \cdot \mathbf{PP'}}{d_{PN}} A_f^d}_{\text{non-orthogonal term}} \tag{2.10}$$

according to Figure 3.3:

$$\frac{A_f^d}{d_{PN}} = \frac{\mathbf{A}_f \cdot \mathbf{A}_f}{\mathbf{A}_f \cdot \mathbf{PN}}$$
$$\mathbf{PP'} = \mathbf{Pf} - (\mathbf{Pf} \cdot \mathbf{n}_f)\mathbf{n}_f \tag{2.11}$$
$$\mathbf{NN'} = \mathbf{Nf} - (\mathbf{Nf} \cdot \mathbf{n}_f)\mathbf{n}_f$$

The orthogonal term is treated implicitly whereas the non-orthogonal term is treated explicitly.

Writing the convection and the diffusion terms in a deferred correction manner, Equation (2.4) can be written as

$$\sum_{f=1}^{n_f(P)} \max(\dot{m}_f, 0.)\phi_P + \sum_{f=1}^{n_f(P)} \min(\dot{m}_f, 0.)\phi_N$$
$$-\sum_{f=1}^{n_f(P)} \frac{\Gamma_F A_d}{d_{PN}}(\phi_N - \phi_P) = \sum_{f=1}^{n_f(P)} \left[\frac{\Gamma_F A_d}{d_{PN}} \left(\nabla\phi_N \cdot \mathbf{NN'} - \nabla\phi_P \cdot \mathbf{PP'} \right) \right]^{n-1} \tag{2.12}$$
$$-\sum_{f=1}^{n_f(P)} \left[\dot{m}_f \phi_f^H - \max(\dot{m}_f, 0.)\phi_P - \min(\dot{m}_f, 0.)\phi_N \right]^{n-1} + s_\phi V_P + S_\phi^{cd}$$

which can be written in the general form of:

$$a_P \phi_P + \sum_{N=nb(P)} a_N \phi_N = S \tag{2.13}$$

where

$$S = s_c^{eqn} V_P + S^{dc} + S^{pres} + S^{cd}$$

$$a_N = -\frac{\Gamma_f A_d}{d_{PN}} + \min\left[\dot{m}_f, 0 \right], \qquad a_P = \sum_{N=nb(P)} -a_N + a_P^o - s_p^{eqn} V_P,$$

$$S^{dc} = -\sum_{f=1}^{n_f(P)} \left[\dot{m}_f \phi_f^H - \max(\dot{m}_f, 0.)\phi_P - \min(\dot{m}_f, 0.)\phi_N \right]^{n-1}$$
$$+ \sum_{f=1}^{n_f(P)} \left[\frac{\Gamma_F A_d}{d_{PN}} \left(\nabla\phi_N \cdot \mathbf{NN'} - \nabla\phi_P \cdot \mathbf{PP'} \right) \right]^{n-1}$$

$$S^{pres} = \begin{cases} = \underbrace{-(\nabla p)_P^x V_P}_{\text{non-conservative}} = \underbrace{-\sum_{f=1}^{n_f} p_f \mathbf{A}_f^x}_{\text{conservative}} & \text{for } x\text{-momentum equation} \\ = \underbrace{-(\nabla p)_P^y V_P}_{\text{non-conservative}} = \underbrace{-\sum_{f=1}^{n_f} p_f \mathbf{A}_f^y}_{\text{conservative}} & \text{for } y\text{-momentum equation} \end{cases}$$

S_ϕ^{cd} = cross derivative diffusion term defined in Equations (2.6).

s_ϕ = source terms per unit volume in the differential equation
= body forces per unit volume in momentum equations
= energy generation rate per unit volume in energy equation

$nb(P)$ → refers to the neighbor nodes of node P,

$n_f(P)$ → neighbor faces of the control volume of node P,

dc → deferred correction (diffusion and convection source terms resulting from the deferred correction procedure used during discretization of the differential equation)

$pres$ → pressure

$(n-1)$ → previous iteration

Generally, the source terms are linearized as in equation $S = S_c + S_p\phi$ where S_c is added to S and $(-S_p)$ is added to a_P.

In order to improve the convergence characteristics of the steady flow equations underrelaxation is usually applied. After relaxation, Equation (2.13) becomes

$$\frac{1}{\alpha} a_P \phi_P + \sum_{N=nb(P)} a_N \phi_N = S + \frac{1-\alpha}{\alpha} a_P \phi_P^n \tag{2.14}$$

where ϕ_P^n is the previous iteration value of ϕ.

Calculation of ϕ_f for Convection Terms:

Upwind difference method (UD):

$$\begin{aligned} \phi_f &= \phi_P \quad \text{for} \quad \dot{m}_f > 0 \\ \phi_f &= \phi_N \quad \text{for} \quad \dot{m}_f < 0 \end{aligned} \tag{2.15}$$

Linear Upwind Difference Scheme (LUD) 2nd order Upwind Difference Scheme (SOU):

LUD formulation along a line in 1-D is:

$$\phi_f = \phi_f^U + \left(\frac{\phi_P - \phi_U}{\Delta x} \right) \frac{1}{2} \Delta x \tag{2.16}$$

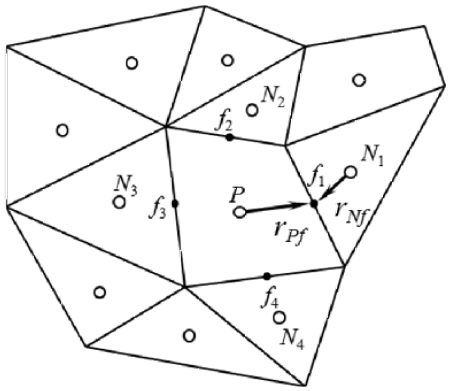

Figure 3.4: Linear Upwind Difference Scheme (LUD) illustration (Sezai I. 2013)

where subscript U refers to upwind node and it is illustrated in Figure 3.4. This can be extended to 3D space using Taylor series expansion around point U:

$$\phi_f = \phi_f^U + \nabla \phi_U \cdot \mathbf{r}_U \tag{2.17}$$

according to Figure 3.4

$$\begin{aligned} &\phi_f^U = \phi_P, \ \ \nabla \phi_U = \nabla \phi_P, \ \ \mathbf{r}_U = \mathbf{r}_{Pf} = \mathbf{r}_f - \mathbf{r}_P \quad \text{for} \ \ \dot{m} > 0 \\ &\phi_f^U = \phi_N, \ \ \nabla \phi_U = \nabla \phi_N, \ \ \mathbf{r}_U = \mathbf{r}_{Nf} = \mathbf{r}_f - \mathbf{r}_N \quad \text{for} \ \ \dot{m} < 0 \end{aligned}$$

or

$$\phi_f = \phi_P + \nabla\phi_P \cdot \mathbf{r}_{Pf} \quad \text{for } \dot{m} > 0$$
$$\phi_f = \phi_N + \nabla\phi_N \cdot \mathbf{r}_{Nf} \quad \text{for } \dot{m} < 0 \tag{2.18}$$

The pressure correction equation can be written as:

$$a_P^{p'} p'_P = \sum_{N=nb(P)} a_N^{p'} p'_N + b_P^{p'}$$
$$a_N^{p'} = \rho_f \frac{(\mathbf{D}_f \mathbf{A}_f) \cdot \mathbf{A}_f}{\mathbf{A}_f \cdot \mathbf{PN}}$$
$$a_P^{p'} = \sum_{N=nb(P)} a_N^{p'} \tag{2.19}$$
$$b_P^{p'} = -\frac{(\rho_P - \rho_P^o)}{\Delta t} V_P - \sum_{f=nb(P)} \dot{m}_f^* + \sum_{f=nb(P)} \rho_f \mathbf{D}_f \overline{\nabla p'_f} \cdot (\mathbf{A}_t)_f$$
$$+ \sum_{f=nb(P)} \rho_f \frac{(\mathbf{D}_f \mathbf{A}_f) \cdot \mathbf{A}_f}{\mathbf{A}_f \cdot \mathbf{PN}} (\nabla p'_N - \nabla p'_P) \cdot \mathbf{PP}'$$

Mass correction given can be written as

$$\dot{m}'_f = -a_N^{p'}(p'_N - p'_P) - a_N^{p'}(\nabla p'_N \cdot \mathbf{NN}' - \nabla p'_P \cdot \mathbf{PP}') \tag{2.20}$$

After solving the p' field from Equation (2.19) the mass flow rate at the surfaces are corrected by using Equation (2.20)

$$\dot{m}_f = \dot{m}_f^* - a_N^{p'}(p'_N - p'_P) - a_N^{p'}(\nabla p'_N \cdot \mathbf{NN}' - \nabla p'_P \cdot \mathbf{PP}') \tag{2.21}$$

The nodal velocities are corrected as:

$$\mathbf{v}_P = \mathbf{v}_P^* + \mathbf{v}'_P = \mathbf{v}_P^* - \mathbf{D}_P \nabla p'_P \tag{2.22}$$

Pressure field is corrected by using:

$$p_P = p_P^* + \alpha_p p'_P \tag{2.23}$$

α_P = pressure under-relaxation factor

SIMPLE Algorithm:

The SIMPLE algorithm, which was implemented in the code, is using the following steps for solving pressure-velocity fields coupling:

Step 1: Solve the discretized transport Equation (2.14) for $\phi = u$ and $\phi = v$

$$\frac{a_P}{\alpha}\phi_P = \sum_{N=nb(P)} a_N\phi_N + S + (1-\alpha)\frac{a_P}{\alpha}\phi_P^{n-1}$$

Step 2: Calculate mass flow rate at cell faces:

$$\dot{m}_f = \rho_f \overline{\mathbf{v}_f} \cdot \mathbf{A}_f + \rho_f \overline{\mathbf{D}}_f \overline{(\nabla p)_f} \cdot \mathbf{A}_f - a_N^{p'}\left(p_N - p_P\right) - a_N^{p'}(\nabla P_N \cdot \mathbf{NN}' - \nabla P_P \cdot \mathbf{PP}')$$

Step 3: Solve pressure correction Equation (2.19)

$$a_P^{p'} p'_P = \sum_{N=nb(P)} a_N^{p'} p'_N + b_P^{p'}$$

Step 4: Correct velocities and pressure at points P using Equations (2.22) and (2.23)

$$\mathbf{v}_P = \mathbf{v}_P^* + \mathbf{v}'_P = \mathbf{v}_P^* - \mathbf{D}_P \nabla p'_P \qquad p_P = p_P^* + \alpha_p p'_P$$

Step 5: Correct mass flow rate using Equation (2.21)

$$\dot{m}_f = \dot{m}_f^* - a_N^{p'}(p'_N - p'_P) - a_N^{p'}(\nabla p'_N \cdot \mathbf{NN}' - \nabla p'_P \cdot \mathbf{PP}')$$

Step 6: Solve the discretized transport Equation (2.14) for other unknowns (i.e. for ϕ = Temperature)

$$\frac{a_P}{\alpha}\phi_P = \sum_{N=nb(P)} a_N\phi_N + S + (1-\alpha)\frac{a_P}{\alpha}\phi_P^{n-1}$$

Step 7: Repeat steps 1 to 6 until convergence.

Chapter 4

TURBULENCE MODELING EQUATIONS

4.1 Introduction

The ability to predict turbulent flow and associated heat transfer by mathematical modelling is of considerable practical value. Lately, there has been extensive improvement in Computational Fluid Dynamics (CFD), where it is possible to predict the performance of the system and optimize its goals efficiently by solving numerical computation with fewer experiments.

In general terms, the criteria for a nice turbulence model are: (1)minimum complexity (i.e. contain a minimum number of differential equations; (2)empirical constants and functions but still provide sufficiently accurate and physically realistic results); (3)robustness (i.e. promote stable convergence and not have difficulty resolving the steep gradients in near-wall regions); (4)possess extensive universality (i.e. can be applied to a large variety of flows without adjusting the empirical constants). For practical engineering calculations, two-equation turbulence models have become the most popular since they are relatively simple to program and place much lower requirements on computer resources than other more complicated models (e.g. algebraic and Reynolds stress models). Consequently, when cost effective, timely solutions of flows spanning large domains with complicated geometries are required, only two-equation models are currently practical. The main difference between two-equation models is the treatment of near-wall regions and

choice of the length scale variable, the equation for the transport of turbulence kinetic energy (k) being common to all. As well, a significant problem with the selection of a turbulence model is that it is often difficult to assess those models available since they have been tested on different test cases using a variety of grid sizes and numerical schemes. Therefore, it is not clear which proposed models provide the best performance, especially in the case of complex flows that involve impingement or boundary separation and reattachment.

This dissertation attempts to resolve small part of this issue by applying and comparing various two-equation turbulent models to different test cases (impinging and separating flows), which all use a standard numerical scheme and identifying preferred methods of predicting various cases performance.

4.2 Momentum Transport Governing Equation

The Reynolds number of a flow gives a measure of the relative importance of inertia forces (associated with convective effects) and viscous forces. In experiments on fluid systems, it is observed that at values below the so-called critical Reynolds number Re_{crit} the flow is smooth and adjacent layers of fluid slide past each other in an orderly fashion. If the applied boundary conditions do not change with time the flow is steady. This regime is called laminar flow.

At values of the Reynolds number above Re_{crit} a complicated series of events takes place which eventually leads to a radical change of the flow character. In the final state the flow behavior is random and chaotic. The motion becomes intrinsically unsteady even with constant imposed boundary conditions. The velocity and all other flow properties vary in a random and chaotic way. This regime is called turbulent

flow. The characteristics of turbulence are diffusive, random, dissipative and three-dimensional. Figure 4.1 shows the time history of turbulent velocity.

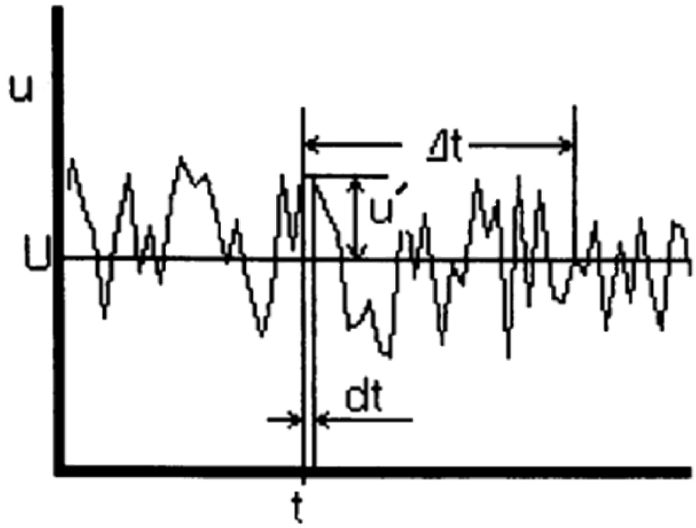

Figure 4.1: Typical point velocity measurement in turbulent flow (Versteeg 2007)

The random nature of a turbulent flow precludes an economical description of the motion of all the fluid particles. Instead, the velocity in Figure 4.1 is decomposed into summation of a steady mean value U with a fluctuating component $u'(t)$ superimposed on it.

$$u(t) = U + u'(t) \tag{3.1}$$

This is called the Reynolds decomposition. A turbulent flow can be considered as the sum of mean values of flow properties (U, V, W, P etc.) and some statistical properties of their fluctuations (u′, v′, w′, p′ etc.).

By assuming that fluid density ρ is constant, the instantaneous continuity and steady Navier-Stokes equations (1827 & 1845) in Cartesian co-ordinate system can be defined as:

$$\text{Continuity} \qquad \frac{\partial u_i}{\partial x_i} = 0$$

$$\text{Momentum} \qquad \frac{\partial(\rho u_i u_j)}{\partial x_i} = -\frac{\partial p}{\partial x_i} + \frac{\partial}{\partial x_i}\left[\mu\left(\frac{\partial u_i}{\partial x_j} + \frac{\partial u_j}{\partial x_i}\right)\right] \tag{3.2}$$

where $p = P + p'$ is the instantaneous pressure and μ is dynamic viscosity.

Since it is necessary to investigate the effects of fluctuations on the mean flow using the Reynolds decomposition given in Equation (3.2) and replace the flow variables *u* (hence also *u*, *v* and *w*) and *p* by the sum of a mean and fluctuating component. Thus by substituting the variables $\mathbf{u} = \mathbf{U} + \mathbf{u}'; u = U + u', v = V + v', w = W + w', p = P + p'$ into Equation (3.2) and time averaging individual terms in momentum equations, it finally yields the time-averaged momentum equations and placing these terms on the right hand side gives the following equations for continuity and momentum:

$$\text{Continuity} \qquad \frac{\partial U_i}{\partial x_i} = 0$$

$$\text{Momentum} \qquad \frac{\partial(\rho U_i U_j)}{\partial x_i} = -\frac{\partial P}{\partial x_i} + \frac{\partial}{\partial x_j}\left[\mu\left(\frac{\partial U_i}{\partial x_j} + \frac{\partial U_j}{\partial x_i}\right) - \rho\overline{u_i' u_j'}\right] \tag{3.3}$$

The extra stress terms $-\overline{u_i' u_j'}$ results from six other stresses, three normal stresses, and three shear stresses. These additional turbulent stresses are termed the Reynolds stresses, which are all non-zero and appears because of the nonlinearity of the Navier-Stokes equation.

The primary task of turbulence modeling is to develop computational procedures to predict these extra terms. (Reynolds stresses and scalar transport terms).

To compute the Reynolds stresses with the turbulent $k-\varepsilon$ model, Boussinesq relationship (1877) is used which indicates that Reynolds stresses might be proportional to mean rates of deformation:

$$\text{Reynolds stress} \qquad -\rho\overline{u_i'u_j'} = \mu_t\left(\frac{\partial U_i}{\partial x_j}+\frac{\partial U_j}{\partial x_i}\right)-\frac{2}{3}\rho k\delta_{ij} \tag{3.4}$$

where, k represents turbulent kinetic energy and δ_{ij} represents the Kronecker delta function.

Substituting Equation (3.4) into Equation (3.3) derives final Turbulent Momentum Equation:

$$\frac{\partial(\rho U_i U_j)}{\partial x_i} = \frac{\partial}{\partial x_j}\left[(\mu+\mu_t)\left(\frac{\partial U_i}{\partial x_j}+\frac{\partial U_j}{\partial x_i}\right)\right]-\frac{\partial P^*}{\partial x_i} \tag{3.5}$$

while $P^* = P+\frac{2}{3}\rho k$.

Applying dimensional analysis, the eddy viscosity can be specified with a relation between turbulent viscosity μ_t to the turbulence kinetic energy, *k*, and the turbulence dissipation rate, ε using equation below:

$$\text{Turbulent viscosity} \qquad \mu_t = \rho C_\mu \frac{k^2}{\varepsilon} \tag{3.6}$$

where C_μ is a dimensionless constant and considered as constant for high Reynolds number. For a simple flow, such as pipe flow or channel flow, the Reynolds stress term can be modeled by a simple Prandtl mixing length model called zero-equation model. The zero-equation model can be modeled directly without any additional differential equations. However, more general and complex flow needs to have a

more sophisticated model that includes k and ε. This is referred to as the second-order closure problem.

4.3 Energy Transport Governing Equation

Similar to the momentum equation, the energy equation has an extra term which is called Reynolds flux:

$$\frac{\partial(\rho U_i T)}{\partial x_i} = \frac{\partial}{\partial x_i}\left[\frac{\mu}{\sigma}\frac{\partial T}{\partial x_i} - \rho\overline{u_i' T'}\right] \tag{3.7}$$

The turbulent heat flux can be obtained using a gradient diffusion model:

$$\rho\overline{u_i' T'} = -\frac{\mu_t}{\sigma_t}\frac{\partial T}{\partial x_i} \tag{3.8}$$

Using the Equation (3.8) the steady-state Reynolds averaged energy equation can be derived as follow:

$$\frac{\partial(\rho U_i T)}{\partial x_i} = \frac{\partial}{\partial x_i}\left[\left(\frac{\mu}{\sigma} + \frac{\mu_t}{\sigma_t}\right)\frac{\partial T}{\partial x_i}\right] \tag{3.9}$$

This energy equation is strongly coupled with the momentum equation so that all the numerical calculations for the governing equations can be performed simultaneously.

4.4 Standard $k-\varepsilon$ models

The standard $k-\varepsilon$ model (originally developed by Launder and Spalding 1974) is the most popular used and approved turbulence model, which has achieved great successes in calculating thin shear layer and recirculating flows without the requirement of individual adjustment of the model constants. It performs particularly well in confined flows where the Reynolds shear stresses are most important. This includes a wide range of flows with industrial engineering applications, which explains its popularity.

As previously mentioned in Equation (3.6), kinetic energy and its dissipation rate are introduced to calculate eddy viscosity. The standard $k-\varepsilon$ model has been applied to many different flows, such as plane jets, mixing layer, boundary layer flows, and so forth. Despite the existence of more advanced turbulent models, such as Direct Numerical Simulation (DNS), Large Eddy Simulation (LES) or Reynolds Stress Model (RSM), the standard $k-\varepsilon$ model has been studied by many researchers because of its easy adaptivity and smaller computational cost. This model was developed on the assumption that the flow is fully turbulent and there is a local equilibrium where rate of production of turbulent stress, P_k, equals rate of turbulent dissipation rate, ε, near the wall. The assumption of fully turbulent flow requires the local turbulent Reynolds number $\mathrm{Re}_t = \rho k^2 / \mu\varepsilon$, to be high. For this reason, the standard $k-\varepsilon$ model is sometimes called the high-Reynolds number $k-\varepsilon$ model, compared to the low-Reynolds number $k-\varepsilon$ model in which calculation is carried out up to the wall including the viscous sublayer. It is necessary for standard $k-\varepsilon$ model to have the first calculation point far away from the wall where the local Reynolds number is large enough to satisfy the above assumption.

In spite of the numerous successes, the standard $k-\varepsilon$ model shows only moderate agreement in unconfined flows. The model is reported not to perform well in weak shear layers (far wakes and mixing layers), and the spreading rate of axisymmetric jets in stagnant surroundings is severely over predicted. In large parts of these flows the rate of production of turbulent kinetic energy is much less than the rate of dissipation and the difficulties can only be overcome by making ad hoc adjustment to model constants.

The turbulent model, including buoyancy term, originally developed by Launder and Spalding (1974), is described by the following equations:

$$\frac{\partial(\rho U_j \mathrm{k})}{\partial x_j} = \frac{\partial}{\partial x_j}\left[(\mu + \frac{\mu_t}{\sigma_k})\frac{\partial k}{\partial x_j}\right] + \rho P_k - \rho\varepsilon \tag{3.10}$$

$$\frac{\partial(\rho U_j \varepsilon)}{\partial x_j} = \frac{\partial}{\partial x_j}\left[(\mu + \frac{\mu_t}{\sigma_\varepsilon})\frac{\partial \varepsilon}{\partial x_j}\right] - \rho C_{1\varepsilon}\frac{\varepsilon}{k} - \rho C_{2\varepsilon}\frac{\varepsilon^2}{k} \tag{3.11}$$

where

$$P_k = \frac{\mu_t}{\rho}\left(\frac{\partial U_i}{\partial x_j} + \frac{\partial U_j}{\partial x_i}\right)\frac{\partial U_i}{\partial x_j}$$

The empirical constants are assigned their usual values, these are

$C_{1\varepsilon} = 0.09$, $C_{2\varepsilon} = 1.44$, $\mathrm{C}_\mu = 1.92$, $\sigma_k = 1.0$, $\sigma_\varepsilon = 1.3$

Equations (3.10) and (3.11) are valid only in high Reynolds number regions. They are not applicable in regions close to solid walls where viscous effects predominate over turbulent ones. Usually Two methods are used in dealing with near-wall regions: low Reynolds number modeling or wall functions. Of interest is the low Reynolds number modeling since wall functions are not recommended for impinging jets and they all perform poorly in the stagnation region where the assumptions used in their derivation are certainly not valid (Heyerichs and Pollard 1996).

4.4.1 Low Reynolds Number (LRN) $k-\varepsilon$ modeling

Efforts have been made in the past for better approximation of refining the near-wall grids without using a wall function. This led to the development of the Low Reynolds versions of $k-\varepsilon$ model. A summary in presented by Patel et al. (1985), compared nine different versions for performance comparison.

The Reynolds number is based on the distance from the wall. In the near-wall region, the flow velocity and distance to the wall are low and the result is a low Reynolds number. Then, low Reynolds number models refer to turbulence models that can simulate the flow in near-wall region where the viscous effects dominate, by integrating the equations right to the wall, without resorting to wall functions.

In low Reynolds number flows, very rapid changes occur in the distribution of k and ε by reaching the buffer layer between the viscous sublayer and fully turbulent region. To force the rapid changes to k and ε, the constants of the high Reynolds number model are multiplied by exponential damping functions which require large number of grid points to resolve the changes. As a result, the system of equations becomes stiff which makes the numerical solution difficult to converge.

Jones and Launder (1972) proposed the first LRN $k-\varepsilon$ model. This model includes damping functions based on the local turbulent Re number. The attempt has been made to predict the appropriate values of the eddy viscosity and the dissipation near the wall where turbulent Reynolds number is small. LRN $k-\varepsilon$ by Lam and Bremhorst (1981), Abid (1993), and Lars Davidson (1990) developed new models to investigate the proper behavior of the turbulent shear stress and the kinetic energy and its dissipation near a solid wall. Chien (1982) was one of the researchers who improved the LRN $k-\varepsilon$ model by applying the Taylor series expansion technique to investigate the proper behavior of the turbulent shear stress and the kinetic energy and its dissipation near a solid wall. Craft et al. (1996) proposed a non-linear LRN model that has a nonlinear relation between strain-stress and vorticity that includes quadratic and cubic terms. Nagano and Tagawa (1990) developed the LRN $k-\varepsilon$

model to satisfy the physical requirements of wall and free turbulence. Chang et al. (1995) developed the LRN $k-\varepsilon$ model to satisfy the physical requirements of wall and free turbulence. For a flow over backward-facing step, experimental data by Kim et al. (1987), Driver and Seegmiller (1985), and Vogel and Eaton (1985) are frequently used to verify the models. For an impinging jet flow, experimental data by Van Heiningen (1982), is frequently used to verify the models. Unlike experimental data, DNS data are often used to develop new turbulence models because of its detailed information of flow quantities even very close to the wall.

For the time being Lam and Bremhorst (1981) model will be discussed which is mainly preferable and popular for a number of reasons. First, it has seen application to a variety of different flows by a number of independent researchers. Also comparing with other LRN $k-\varepsilon$ models, tests have shown that it is among the best at predicting the characteristics of fully turbulent flow.

The general forms of $k-\varepsilon$ group of models are:

$$\frac{\partial(\rho u_j \mathrm{k})}{\partial x_j} = \frac{\partial}{\partial x_j}\left[(\mu + \frac{\mu_t}{\sigma_k})\frac{\partial k}{\partial x_j}\right] - \rho\overline{u_i' u_j'}\frac{\partial u_i}{\partial x_j} - \rho\varepsilon \tag{3.12}$$

$$\frac{\partial(\rho u_j \varepsilon)}{\partial x_j} = \frac{\partial}{\partial x_j}\left[(\mu + \frac{\mu_t}{\sigma_\varepsilon})\frac{\partial \varepsilon}{\partial x_j}\right] - f_1\rho C_{1\varepsilon}\frac{\varepsilon}{k}\overline{u_i' u_j'}\frac{\partial u_i}{\partial x_j} - f_2\rho C_{2\varepsilon}\frac{\varepsilon^2}{k} \tag{3.13}$$

The steady state equations of the $k-\varepsilon$ group of models are defined in Equations (3.12) and (3.13).

The coefficients, wall damping functions and constants used for the Lam & Bremhorst model are defined below:

Turbulent viscosity $\mu_t = \rho C_\mu f_\mu \frac{k^2}{\varepsilon}$ (3.14)

Damping functions
$$\begin{cases} f_\mu = \left[1-\exp(-0.0165 Re_y)\right]^2 \left(1+\frac{20.5}{Re_t}\right) \\ f_1 = 1+\left(\frac{0.05}{f_\mu}\right)^3 \quad f_2 = 1-\exp(-Re_t^2) \end{cases} \quad (3.15)$$

$C_\mu = 0.09, \quad \sigma_t = 0.9, \quad \sigma_k = 1.00, \quad \sigma_\varepsilon = 1.30, \quad C_{1\varepsilon} = 1.44, \quad C_{2\varepsilon} = 1.92$

$Re_t = \frac{\rho k^2}{\varepsilon \mu} \quad Re_y = \frac{\rho \sqrt{k}\, y}{\mu}$

where y is the minimum distance to the nearest wall.

Defining the boundary conditions, for inlet in internal flows, if no k and ε are available, crude approximations could be attained from the Characteristic length L (equivalent pipe diameter) and Turbulence intensity T_i which are defined in Table 4.1:

Table 4.1: Boundary Conditions in Lam & Bremhost model

Inlet	$k_{in} = \frac{3}{2}\left(U_{ref} T_i\right)^2$ and $\varepsilon_{in} = C_\mu^{3/4} \frac{k^{3/2}}{\ell}, \ell = 0.07L$
Outlet or symmetry axis	$\frac{\partial k}{\partial n} = 0$ *and* $\frac{\partial \varepsilon}{\partial n} = 0$
Solid walls	$k_{wall} = 0$ *and* $\frac{\partial \varepsilon}{\partial y} = 0$

The low Reynolds number $k-\varepsilon$ model equations can be written in generic form:

$$\frac{\partial(\rho\phi)}{\partial t} + div(\rho\phi \mathbf{v}) = div(\Gamma grad\,\phi) + s_\phi + s_\phi^{cd} \quad (3.16)$$

In Equation (3.16) s_ϕ is the source term due to body forces and pressure for the case of momentum equations, or energy generation per unit volume in the case of energy equation. The term s_ϕ^{cd} is the diffusion source terms involving cross derivatives in the momentum equations.

The variables (ϕ, Γ and S_ϕ) for Momentum, Energy, k and ε equations are shown in Table 4.2.

Table 4.2: Low Reynolds Number equations (Generic form)

Equation	ϕ	Γ	S_ϕ
Continuity	1	0	0
X-Momentum	U	μ_{eff}	$\frac{\partial}{\partial x}\left(\mu_{eff}\frac{\partial U}{\partial x}\right)+\frac{\partial}{\partial y}\left(\mu_{eff}\frac{\partial V}{\partial x}\right)+\frac{\partial}{\partial z}\left(\mu_{eff}\frac{\partial W}{\partial x}\right)-\frac{\partial P^*}{\partial x}$
Y-Momentum	V	μ_{eff}	$\frac{\partial}{\partial x}\left(\mu_{eff}\frac{\partial U}{\partial y}\right)+\frac{\partial}{\partial y}\left(\mu_{eff}\frac{\partial V}{\partial y}\right)+\frac{\partial}{\partial z}\left(\mu_{eff}\frac{\partial W}{\partial y}\right)-\frac{\partial P^*}{\partial y}$
Z-Momentum	W	μ_{eff}	$\frac{\partial}{\partial x}\left(\mu_{eff}\frac{\partial U}{\partial z}\right)+\frac{\partial}{\partial y}\left(\mu_{eff}\frac{\partial V}{\partial z}\right)+\frac{\partial}{\partial z}\left(\mu_{eff}\frac{\partial W}{\partial z}\right)-\frac{\partial P^*}{\partial z}$
Energy	T	$\frac{\mu}{\sigma}+\frac{\mu_t}{\sigma_t}$	0
Turbulence	K	$\mu+\frac{\mu_t}{\sigma_k}$	$P_k-\rho\varepsilon$
Dissipation	ε	$\mu+\frac{\mu_t}{\sigma_\varepsilon}$	$C_{1\varepsilon}f_1\frac{\varepsilon}{k}P_k-C_{2\varepsilon}f_2\rho\frac{\varepsilon^2}{k}$

$$S_{ij}S_{ij}=\left(\frac{\partial U}{\partial x}\right)^2+\left(\frac{\partial V}{\partial y}\right)^2+\left(\frac{\partial W}{\partial z}\right)^2+\frac{1}{2}\left(\frac{\partial U}{\partial y}+\frac{\partial V}{\partial x}\right)^2+\frac{1}{2}\left(\frac{\partial W}{\partial x}+\frac{\partial U}{\partial z}\right)^2+\frac{1}{2}\left(\frac{\partial V}{\partial z}+\frac{\partial W}{\partial y}\right)^2$$

$$\mu_{eff}=\mu+\mu_t \qquad \mu_t=\rho C_\mu f_\mu\frac{k^2}{\varepsilon} \qquad P^*=P+\left(\frac{2}{3}\right)\rho k \qquad P_k=2\mu_t S_{ij}S_{ij}$$

$$Re_t=\frac{\rho k^2}{\varepsilon\mu} \qquad Re_y=\frac{\rho\sqrt{k}\,y}{\mu} \qquad \sigma=Pr=\frac{\mu C_p}{k}$$

Linearization of source terms:

One of the basic rules require that when the source term is linearized as

$$S = S_C + S_P \phi_P \tag{3.17}$$

The quantity S_P must not be positive for a convergent iterative solution, which ensures diagonal dominance of the coefficient matrix. However S_C must be positive to obtain all positive ϕ values. Often source terms are the cause of divergence of iterations and that proper linearization of the source term frequently holds the key to the attainment of a converged solution.

When source S depends on ϕ, the dependence is expressed in a linear form given by Equation (3.17). This is done because first, our nominally linear framework would allow only a formally linear dependence, then the incorporation of linear dependence is better than treating S as a constant.

When S is a nonlinear function of ϕ, it must be linearized, i.e. specify the values of S_C and S_P which may themselves depend on ϕ. During each iteration cycle, S_C and S_P would then be recalculated from the new values of ϕ. The linearization of S should be a good representation of S and ϕ relationship.

Both k and ε are strictly positive quantities. So, to obtain always positive results for k and ε, the source terms should be formulated such that S_C is positive and S_P is negative for k and ε equations.

For k equation source term by inserting equation $\varepsilon = \rho C_\mu f_\mu \frac{k^2}{\mu_t}$ in the turbulent source term:

$$S_k = P_k - \rho\varepsilon = P_k - \frac{\rho^2 C_\mu f_\mu}{\mu_t} k^2 \tag{3.18}$$

$$\text{Kinetic energy source terms} \begin{cases} S_{Ck} = P_k \\ S_{Pk} = -\frac{\rho^2 C_\mu f_\mu}{\mu_t} k \end{cases} \tag{3.19}$$

For ε source term:

$$S_\varepsilon = C_{1\varepsilon} f_1 P_k \frac{\varepsilon}{k} - C_{2\varepsilon} f_2 \rho \frac{\varepsilon^2}{k} \tag{3.20}$$

Rewriting source terms in terms of eddy viscosity μ_t :

$$\mu_t = \frac{\rho C_\mu f_\mu k^2}{\varepsilon} \rightarrow \frac{\varepsilon}{k} = \frac{\rho C_\mu f_\mu k}{\mu_t}, \frac{\varepsilon^2}{k} = \frac{\rho C_\mu f_\mu k \varepsilon}{\mu_t}$$

Gives:

$$\text{Dissipation source terms} \begin{cases} S_{C\varepsilon} = C_{1\varepsilon} f_1 P_k \frac{\rho C_\mu f_\mu k}{\mu_t} \\ S_{P\varepsilon} = -C_{2\varepsilon} f_2 \rho \frac{\rho C_\mu f_\mu k}{\mu_t} \end{cases} \tag{3.21}$$

In order to avoid negative values for k and ε, and division by zero, μ_t is limited to a small fraction of laminar viscosity μ_l by using:

$$\text{Turbulent viscosity limitation} \qquad \mu_t = \max\left(\rho C_\mu f_\mu \frac{k^2}{\varepsilon}, 10^{-4} \mu_l \right) \tag{3.22}$$

4.5 Wilcox $k-\omega$ models (2006)

The standard $k-\omega$ model was originally proposed and developed by Wilcox. In this model, two transport equations for the kinetic energy of turbulence *k* and its specific dissipation rate ω are solved. One major advantage of the $k-\omega$ model are that the

transport equations for k and ω are solved right across the boundary layer, all the way to the wall, through the viscous sublayer, and a low Reynolds number modification using an extra damping term is not required. However, the original $k-\omega$ model of Wilcox has one main drawback: the results depend on the free-stream value of the turbulence variables (in particular ω) even at very low free-stream eddy-viscosity levels. This free-stream dependence seems to be the strongest for free shear layers, but is also significant for boundary layers, whereas the $k-\varepsilon$ model is insensitive to the free-stream turbulence.

As described above, the $k-\omega$ turbulence model is similar to the low Reynolds number $k-\varepsilon$ model with ε replaced by ω which represents the frequency of the vorticity fluctuations and the relation defined by Wilcox (2006) is given below:

$$\varepsilon = \beta^* \omega k \tag{3.23}$$

It is initially attracted attention because it does not require wall-damping functions nor the computation of wall distances, and it is less stiff than $k-\varepsilon$ models in the near-wall region.

The turbulent eddy viscosity μ_t is expressed in terms of ω as:

$$\mu_t = \frac{\rho k}{\hat{\omega}} \tag{3.24}$$

This Equation shows that the eddy viscosity μ_t is indeterminate or infinite as $\omega \to 0$, so a small non-zero value of ω must be specified.

$$\hat{\omega} = \max\left[\omega, C_{\lim}\sqrt{\frac{2\bar{S}_{ij}\bar{S}_{ij}}{\beta^*}}\right] \tag{3.25}$$

$$\overline{S}_{ij} = S_{ij} - \frac{1}{3}\frac{\partial u_k}{\partial x_k}\delta_{ij} \tag{3.26}$$

The Reynolds stresses are computed from Boussinesq expression:

$$\tau_{ij} = -\rho\overline{u_i' u_j'} = 2\mu_t S_{ij} - \frac{2}{3}\rho k\delta_{ij} = \mu_t\left(\frac{\partial U_i}{\partial x_j} + \frac{\partial U_j}{\partial x_i}\right) - \frac{2}{3}\rho k\delta_{ij} \tag{3.27}$$

The transport equations for k-ω steady state turbulent flows are:

$$\frac{\partial(\rho U_j k)}{\partial x_j} = P - \beta^*\rho\omega k + \frac{\partial}{\partial x_j}\left[\left(\mu + \sigma_k\frac{\rho k}{\omega}\right)\frac{\partial k}{\partial x_j}\right] \tag{3.28}$$

$$\frac{\partial(\rho U_j \omega)}{\partial x_j} = \frac{\gamma\omega}{k}P - \beta\rho\omega^2 + \frac{\partial}{\partial x_j}\left[\left(\mu + \sigma_\omega\frac{\rho k}{\omega}\right)\frac{\partial\omega}{\partial x_j}\right] + \frac{\rho\sigma_d}{\omega}\frac{\partial k}{\partial x_j}\frac{\partial\omega}{\partial x_j} \tag{3.29}$$

$$P = \tau_{ij}\frac{\partial U_i}{\partial x_j} = 2\mu_t S_{ij}S_{ij} - \frac{2}{3}\rho k\frac{\partial U_i}{\partial x_j}\delta_{ij}$$

The model constants and equations are described below:

$$\begin{aligned}
&\sigma_k = 0.6,\ \ \sigma_\omega = 0.5,\ \ \gamma = \frac{13}{25},\ \ \beta^* = 0.09,\ \ C_{\lim} = \frac{7}{8}\\
&\beta = \beta_0 f_\beta,\ \ \ \beta_0 = 0.0708,\ \ f_\beta = \frac{1+85\chi_\omega}{1+100\chi_\omega},\ \ \chi_\omega = \left|\frac{\Omega_{ij}\Omega_{jk}\hat{S}_{ki}}{\left(\beta^*\omega\right)^3}\right|\\
&\hat{S}_{ki} = S_{ki} - \frac{1}{2}\frac{\partial u_m}{\partial x_m}\delta_{ki},\ \ \sigma_d = \begin{cases} 0 & \frac{\partial k}{\partial x_j}\frac{\partial\omega}{\partial x_j} \le 0 \\ \frac{1}{8} & \frac{\partial k}{\partial x_j}\frac{\partial\omega}{\partial x_j} > 0 \end{cases}\\
&S_{ij} = \frac{1}{2}\left(\frac{\partial u_i}{\partial x_j} + \frac{\partial u_j}{\partial x_i}\right),\ \ \Omega_{ij} = \frac{1}{2}\left(\frac{\partial u_i}{\partial x_j} - \frac{\partial u_j}{\partial x_i}\right)
\end{aligned} \tag{3.30}$$

The tensors Ω_{ij} and S_{ij} are the mean-rotation and mean-strain-rate tensors. As can be easily verified the quantity χ_ω is zero for two-dimensional flows.

For the boundary conditions, many CFD codes employ the approximate ω wall boundary condition from Menter for this model (Equation (3.56)) which is defined in Table 4.3 again.

At inlet boundaries the values of k and ω can be obtained from characteristic length L (pipe diameter) and turbulence intensity T_i.

Table 4.3: Boundary Conditions in Wilcox $k-\omega$ model (2006)

Inlet	$k_{in}=\frac{3}{2}\left(U_{ref}T_i\right)^2$ and $\varepsilon_{in}=C_\mu^{3/4}\frac{k^{3/2}}{\ell}, \ell=0.07L$ $\omega_{in}=\frac{\varepsilon_{in}}{0.09k_{in}}$
Outlet or symmetry axis	$\frac{\partial k}{\partial n}=0$ *and* $\frac{\partial \omega}{\partial n}=0$
Solid walls	$k_{wall}=0$ *and* $\omega_{wall}=10\frac{6\mu}{0.075\rho(\Delta y_1)^2}$

as $\Delta y_1 \to 0$, where Δy_1 is the distance to the nearest wall.

In Table 4.4 the Wilcox $k-\omega$ (2006) model equations are written in generic form.

Table 4.4: Wilcox $k-\omega$ model (2006) equations (generic form)

Equation	ϕ	Γ	S_ϕ
Continuity	1	0	0
X-Momentum	U	μ_{eff}	$\frac{\partial}{\partial x}\left(\mu_{eff}\frac{\partial U}{\partial x}\right)+\frac{\partial}{\partial y}\left(\mu_{eff}\frac{\partial V}{\partial x}\right)+\frac{\partial}{\partial z}\left(\mu_{eff}\frac{\partial W}{\partial x}\right)-\frac{\partial P^*}{\partial x}$
Y-Momentum	V	μ_{eff}	$\frac{\partial}{\partial x}\left(\mu_{eff}\frac{\partial U}{\partial y}\right)+\frac{\partial}{\partial y}\left(\mu_{eff}\frac{\partial V}{\partial y}\right)+\frac{\partial}{\partial z}\left(\mu_{eff}\frac{\partial W}{\partial y}\right)-\frac{\partial P^*}{\partial y}$
Z-Momentum	W	μ_{eff}	$\frac{\partial}{\partial x}\left(\mu_{eff}\frac{\partial U}{\partial z}\right)+\frac{\partial}{\partial y}\left(\mu_{eff}\frac{\partial V}{\partial z}\right)+\frac{\partial}{\partial z}\left(\mu_{eff}\frac{\partial W}{\partial z}\right)-\frac{\partial P^*}{\partial z}$
Energy	T	$\frac{\mu}{\sigma}+\frac{\mu_t}{\sigma_t}$	0
Turbulence	K	$\mu+\sigma_k\frac{\rho k}{\omega}$	$2\mu_t S_{ij}S_{ij}-\frac{2}{3}\rho k(\frac{\partial U}{\partial X}+\frac{\partial V}{\partial Y})-\beta^*\rho\omega k$
Dissipation	ω	$\mu+\sigma_\omega\frac{\rho k}{\omega}$	$\frac{\gamma\omega}{k}P-\beta\rho\omega^2+\frac{\rho\sigma_d}{\omega}(\frac{\partial k}{\partial X}\frac{\partial \omega}{\partial X}+\frac{\partial k}{\partial Y}\frac{\partial \omega}{\partial Y})$

$$\mu_{eff} = \mu + \mu_t \qquad P^* = P + \left(\frac{2}{3}\right)\rho k \qquad P = 2\mu_t S_{ij} S_{ij}$$

Linearization of the source terms according to the Equation (3.17) is as follows:

k equation:

$$S_k = 2\mu_t S_{ij} S_{ij} - \frac{2}{3}\rho k\left(\frac{\partial U}{\partial X} + \frac{\partial V}{\partial Y}\right) - \beta^* \rho \omega k \tag{3.31}$$

The linearized source terms are:

$$S_{ck} = 2\mu_t S_{ij} S_{ij} - \frac{2}{3}\rho k\left(\frac{\partial U}{\partial X} + \frac{\partial V}{\partial Y}\right) \tag{3.32}$$

$$S_{pk} = -\beta^* \rho \omega \tag{3.33}$$

and for ω equation:

$$S_\omega = \frac{\gamma\omega}{k} P - \beta\rho\omega^2 + \frac{\rho\sigma_d}{\omega}\left(\frac{\partial k}{\partial X}\frac{\partial \omega}{\partial X} + \frac{\partial k}{\partial Y}\frac{\partial \omega}{\partial Y}\right) \tag{3.34}$$

The linearized source terms are:

$$S_{c\omega} = \frac{\gamma\omega}{k} P + \frac{\rho\sigma_d}{\omega}\left(\frac{\partial k}{\partial X}\frac{\partial \omega}{\partial X} + \frac{\partial k}{\partial Y}\frac{\partial \omega}{\partial Y}\right) = 2\mu_t S_{ij} S_{ij}\frac{\gamma\omega}{k} + \frac{\rho\sigma_d}{\omega}\left(\frac{\partial k}{\partial X}\frac{\partial \omega}{\partial X} + \frac{\partial k}{\partial Y}\frac{\partial \omega}{\partial Y}\right) \tag{3.35}$$

$$S_{p\omega} = -\beta\rho\omega \tag{3.36}$$

4.5.1 Low Reynolds Number version of Wilcox (2006)

This model is the same as Wilcox (2006) model with the minor changes which is named as Wilcox2006-LRN.

In constants of Equation (3.30), instead of $\beta^* = 0.09$ following is used:

$$\beta^* = 0.09\left(\frac{100\beta_0/27 + \left(\mathrm{Re}_T/R_\beta\right)^4}{1 + \left(\mathrm{Re}_T/R_\beta\right)^4}\right) \tag{3.37}$$

where $\mathrm{Re}_T = \dfrac{\rho k}{\mu\omega}$, $R_\beta = 8$ and $\beta_0 = 0.0708$.

also, the same applies to $\gamma = \frac{13}{25}$ which is replaced by

$$\gamma = \frac{13}{25}\left(\frac{\alpha_0 + \mathrm{Re}_T / R_\omega}{1 + \mathrm{Re}_T / R_\omega}\right)\left(\alpha^*\right)^{-1} \tag{3.38}$$

where $\alpha^* = \frac{\alpha_0^* + \mathrm{Re}_T / R_k}{1 + \mathrm{Re}_T / R_k}$, $\alpha_0^* = \beta_0 / 3$, $\alpha_0 = \frac{1}{9}$, $R_\omega = 2.61$ and $R_k = 6$.

Instead of $\mu_t = \frac{\rho k}{\hat{\omega}}$ following will be used

$$\mu_t = \alpha^* \frac{\rho k}{\hat{\omega}} \tag{3.39}$$

Replacing Equation (3.25) $\hat{\omega}$ with $\hat{\omega} = \max\left[\omega, C_{\lim}\sqrt{\frac{2\bar{S}_{ij}\bar{S}_{ij}}{\beta_0^* / \alpha^*}}\right]$

while $\beta_0^* = 0.09$

Finally in Equations (3.28) and (3.29) instead of k and ω diffusion terms $\left(\mu + \sigma_k \frac{\rho k}{\omega}\right)$ and $\left(\mu + \sigma_\omega \frac{\rho k}{\omega}\right)$ following will be replaced:

$$\left(\mu + \sigma_k \alpha^* \frac{\rho k}{\omega}\right) \tag{3.40}$$

$$\left(\mu + \sigma_\omega \alpha^* \frac{\rho k}{\omega}\right) \tag{3.41}$$

4.6 Revised Menter-SST $k-\omega$ model (2003)

In practice, the $k-\varepsilon$ models are generally more accurate in shear type flows and are well behaved in the far field. The $k-\omega$ models are more accurate and much more numerically stable in the near wall region. Recognizing that each model has its strength and weakness and that the forms of the equations are similar, Menter (1992)

noted that the results of the $k-\varepsilon$ model are much less sensitive to the (arbitrary) assumed values in the free stream, but its near-wall performance is unsatisfactory for boundary layers with adverse pressure gradients. He suggested a hybrid model using a transformation of the $k-\varepsilon$ model into $k-\omega$ model in the near-wall region and the standard $k-\varepsilon$ model in the fully turbulent region far from the wall.

Menter (2006) developed the shear-stress transport SST $k-\omega$ model, which effectively blends the robust and accurate formulation of the $k-\omega$ model in the near-wall region with the free-stream independence of the $k-\varepsilon$ model in the far field. To achieve this, the $k-\varepsilon$ model is converted into a $k-\omega$ formulation. The standard $k-\omega$ model and the transformed $k-\varepsilon$ model are both multiplied by a blending function, and the two models are added together. The blending function is designed to be one in the near-wall region, which activates the standard $k-\omega$ model, and zero away from the surface, which activates the transformed $k-\varepsilon$ model. The SST model also incorporates a damped cross-diffusion derivative term in the ω transport equation. The definition of the turbulent viscosity is modified to account for the transport of the turbulent shear stress, and the modeling constants are different. These features make the SST $k-\omega$ model more accurate and reliable for a wider class of flows (e.g., adverse-pressure-gradient flows, airfoils, transonic shock waves) than the standard $k-\omega$ model.

Here, the complete formulation of the latest SST model in steady state is given, with the limited number of modifications to the original model.

$$\frac{\partial(\rho u_i k)}{\partial x_i} = \tilde{P}_k - \beta^* \rho \omega k + \frac{\partial}{\partial x_i}\left[(\mu + \sigma_k \mu_t) \frac{\partial k}{\partial x_i} \right] \tag{3.42}$$

$$\frac{\partial\left(\rho U_i \omega\right)}{\partial x_i} = \frac{\alpha \tilde{P}_k \rho}{\mu_t} - \beta\rho\omega^2 + \frac{\partial}{\partial x_i}\left[\left(\mu + \sigma_{\omega 1}\mu_t\right)\frac{\partial\omega}{\partial x_i}\right] + 2\left(1-F_1\right)\rho\sigma_{\omega 2}\frac{1}{\omega}\frac{\partial k}{\partial x_i}\frac{\partial\omega}{\partial x_i} \tag{3.43}$$

where the blending function F_1 is defined by:

$$F_1 = \tanh\left\{\left\{\min\left[\max\left(\frac{\sqrt{k}}{\beta^*\omega y}, \frac{500\mu}{\rho y^2\omega}\right), \frac{4\rho\sigma_{\omega 2}k}{CD_{k\omega}y^2}\right]\right\}^4\right\} \tag{3.44}$$

with $CD_{k\omega} = \max\left(2\rho\sigma_{\omega 2}\frac{1}{\omega}\frac{\partial k}{\partial x_i}\frac{\partial\omega}{\partial x_i}, 10^{-10}\right)$ and y is the distance to the nearest wall.

F_1 is equal to zero away from the surface ($k-\varepsilon$ model), and switches over to one inside the boundary layer ($k-\omega$ model).

The turbulent eddy viscosity is defined as follows:

$$\mu_t = \frac{\rho a_1 k}{\max\left(a_1\omega, SF_2\right)} \tag{3.45}$$

where

$$\begin{aligned} &S = \sqrt{2S_{ij}S_{ij}}, \quad S_{ij} = \frac{1}{2}\left(\frac{\partial u_i}{\partial x_j} + \frac{\partial u_j}{\partial x_i}\right) \\ &S_{ij}S_{ij} = \left(\frac{\partial U}{\partial x}\right)^2 + \left(\frac{\partial V}{\partial y}\right)^2 + \left(\frac{\partial W}{\partial z}\right)^2 \\ &+\frac{1}{2}\left(\frac{\partial U}{\partial y} + \frac{\partial V}{\partial x}\right)^2 + \frac{1}{2}\left(\frac{\partial W}{\partial x} + \frac{\partial U}{\partial z}\right)^2 + \frac{1}{2}\left(\frac{\partial V}{\partial z} + \frac{\partial W}{\partial y}\right)^2 \end{aligned} \tag{3.46}$$

where S is the invariant measure of the strain rate and F_2 is a second blending function defined by:

$$F_2 = \tanh\left[\left[\max\left(\frac{2\sqrt{k}}{\beta^*\omega y}, \frac{500\mu}{\rho y^2\omega}\right)\right]^2\right] \tag{3.47}$$

A production limiter is used in the SST model to prevent the build-up of turbulence in stagnation regions:

$$P_k = \mu_t \frac{\partial U_i}{\partial x_j}\left(\frac{\partial U_i}{\partial x_j}+\frac{\partial U_j}{\partial x_i}\right) \rightarrow \tilde{P}_k = \min\left(P_k, 10.\beta^*\rho k\omega\right) \tag{3.48}$$

All constants are computed by a blend from the corresponding constants of $k-\varepsilon$ and $k-\omega$ model via $\phi = \phi_1 F_1 + \phi_2\left(1-F_1\right)$ etc.

The constants for this model are:

$$\begin{aligned} &\beta^* = 0.09,\ \alpha_1 = \frac{5}{9},\ \alpha_2 = 0.44,\ \beta_1 = 0.075,\ \beta_2 = 0.0828 \\ &\sigma_{k1} = 0.85,\ \sigma_{k2} = 1,\ \sigma_{\omega 1} = 0.5,\ \sigma_{\omega 2} = 0.856,\ a_1 = 0.31 \end{aligned} \tag{3.49}$$

In Table 4.5 the Revised Menter-SST $k-\omega$ model (2003) equations are written in generic form.

Table 4.5: Revised Menter-SST $k-\omega$ model (2003) equations (generic form)

Equation	ϕ	Γ	S_ϕ
Continuity	1	0	0
X-Momentum	U	μ_{eff}	$\frac{\partial}{\partial x}\left(\mu_{eff}\frac{\partial U}{\partial x}\right)+\frac{\partial}{\partial y}\left(\mu_{eff}\frac{\partial V}{\partial x}\right)+\frac{\partial}{\partial z}\left(\mu_{eff}\frac{\partial W}{\partial x}\right)-\frac{\partial P^*}{\partial x}$
Y-Momentum	V	μ_{eff}	$\frac{\partial}{\partial x}\left(\mu_{eff}\frac{\partial U}{\partial y}\right)+\frac{\partial}{\partial y}\left(\mu_{eff}\frac{\partial V}{\partial y}\right)+\frac{\partial}{\partial z}\left(\mu_{eff}\frac{\partial W}{\partial y}\right)-\frac{\partial P^*}{\partial y}$
Z-Momentum	W	μ_{eff}	$\frac{\partial}{\partial x}\left(\mu_{eff}\frac{\partial U}{\partial z}\right)+\frac{\partial}{\partial y}\left(\mu_{eff}\frac{\partial V}{\partial z}\right)+\frac{\partial}{\partial z}\left(\mu_{eff}\frac{\partial W}{\partial z}\right)-\frac{\partial P^*}{\partial z}$
Energy	T	$\frac{\mu}{\sigma}+\frac{\mu_t}{\sigma_t}$	0
Turbulence	K	$\mu+\sigma_k\mu_t$	$\tilde{P}_k-\beta^*\rho\omega k$
Dissipation	ω	$\mu+\sigma_\omega\mu_t$	$\frac{\rho\alpha\tilde{P}_k}{\mu_t}-\beta\rho\omega^2+2\left(1-F_1\right)\rho\sigma_{\omega 2}\frac{1}{\omega}\frac{\partial k}{\partial x_i}\frac{\partial \omega}{\partial x_i}$

$$\mu_{eff} = \mu + \mu_t \qquad P^* = P + \left(\frac{2}{3}\right)\rho k$$

Linearization of the source terms:

k equation:

$$S_k = \tilde{P}_k - \beta^* \rho \omega k \tag{3.50}$$

The source terms are:

$$S_c = \tilde{P}_k \tag{3.51}$$

$$S_p = -\beta^* \rho \omega \tag{3.52}$$

ω equation:

$$S_\omega = \frac{\rho \alpha \tilde{P}_k}{\mu_t} - \beta \rho \omega^2 + 2(1 - F_1) \rho \sigma_{\omega 2} \frac{1}{\omega} \frac{\partial k}{\partial x_i} \frac{\partial \omega}{\partial x_i} \tag{3.53}$$

Results of the linearization are:

$$S_c = \frac{\rho \alpha \tilde{P}_k}{\mu_t} + 2(1 - F_1) \rho \sigma_{\omega 2} \frac{1}{\omega} \frac{\partial k}{\partial x_i} \frac{\partial \omega}{\partial x_i} \tag{3.54}$$

$$S_p = -\beta \rho \omega \tag{3.55}$$

The recommended boundary conditions for smooth walls are mentioned:

$$\begin{aligned} \omega_{wall} &= 10 \frac{6\mu}{\rho \beta_1 (\Delta y_1)^2} \\ k_{wall} &= 0 \end{aligned} \tag{3.56}$$

as $\Delta y_1 \to 0$, where Δy_1 is the distance to the nearest wall.

Hellsten, A. (1998) has suggested a simplified rotation/curvature model, which is the same as Menter's SST (2003) method except that the destruction term in the ω equation is multiplied by the function F_4 described below:

$$\begin{aligned} F_4 &= \frac{1}{1 + C_{RC} R_i} \\ R_i &= \frac{W}{S} \left(\frac{W}{S} - 1 \right) \end{aligned} \tag{3.57}$$

The strain rate S is defined previously in Equation (3.46).

$$\text{Vorticity magnitude} \quad W = \sqrt{2W_{ij}W_{ij}} \qquad W_{ij} = \frac{1}{2}\left(\frac{\partial u_i}{\partial x_j} - \frac{\partial u_j}{\partial x_i}\right)$$
$$W_{ij}W_{ij} = \frac{1}{2}\left(\frac{\partial U}{\partial y} - \frac{\partial V}{\partial x}\right)^2 + \frac{1}{2}\left(\frac{\partial U}{\partial z} - \frac{\partial W}{\partial x}\right)^2 + \frac{1}{2}\left(\frac{\partial V}{\partial z} - \frac{\partial W}{\partial y}\right)^2 \tag{3.58}$$

$$C_{RC} = 1.4 \tag{3.59}$$

This corrected model is referred as (SST-2003RC-Hellsten).

F. R. Menter (2010) has also developed a model called the scale adaptive simulation model. This model has been derived from the exact transport equation for the correlation *kL* of the turbulence kinetic energy *k* and the integral length scale of turbulence *L*, which offers a profound starting point for the modeling of the relevant terms and finally leads to the introduction of the Von Karman length scale L_{vk} into the turbulence scale equation. Because the turbulence scale equation in statistical two-equation turbulence models can be transformed from one variable to another (e.g., *kL* to specific dissipation rate ω), the new model is transformed into the $k-\omega$ shear stress transport (SST) framework, yielding an additional source term Q_{SAS} in the ω equation:

$$Q_{SAS} = \max\left[\rho\zeta_2 S^2\left(\frac{L}{L_{vk}}\right)^2 - C_{SAS}\frac{2\rho k}{\sigma_\phi}\max\left(\frac{1}{\omega^2}\frac{\partial\omega}{\partial x_j}\frac{\partial\omega}{\partial x_j}, \frac{1}{k^2}\frac{\partial k}{\partial x_j}\frac{\partial k}{\partial x_j}\right), 0\right] \tag{3.60}$$

with the strain rate S defined in Equation (3.46) and the constants $\zeta_2 = 1.47$, $C_{SAS} = 2$ as well as $\sigma_\phi = 2/3$. The turbulence length scale L can be calculated with the help of the two variables of the underlying turbulence model via $L = k^{1/2}/\left(\omega C_\mu^{1/4}\right)$ and the corresponding constant $C_\mu = 0.09$. The generalized formulation of the Von Karman length scale L_{vk} is based on the second derivative of the velocity field and is given by

$$L_{vk} = \kappa \left| \frac{S}{U''} \right|, \qquad U'' = \sqrt{\frac{\partial^2 U_i}{\partial x_k^2} \frac{\partial^2 U_i}{\partial x_k^2}} \tag{3.61}$$

while the Von Karman constant value is $\kappa = 0.41$. If the flow field exhibits sufficient inherent instabilities, the source term will be activated, leading to an increased production of the specific dissipation rate in these areas. This results in lower levels of eddy viscosity and eventually leads to the resolution of turbulent fluctuations. On the other hand, in stable flow regimes such as attached boundary layers, the source term remains inactive, thus allow treating these areas efficiently with the standard RANS capabilities of the SST turbulence model.

Chapter 5

RESULTS AND DISCUSSIONS

5.1 Introduction

In order to solve the governing equations for turbulent flow, turbulence models are written in FORTRAN code and added to an existing unstructured flow solver developed in the Mechanical Engineering Department by I. Sezai. For pressure-velocity decoupling, SIMPLE algorithm is employed, and the turbulence models are solved in conjunction with the Reynolds-averaged momentum and energy equations using a control volume method. In discretization of the convection term, upwind scheme is used for turbulence terms while Linear-Upwind-Differencing (LUD) scheme is used for discretizing momentum convection equations. For better resolution near the wall, nonuniform grids are used so that fine meshing is applied near the walls and stagnation region.

Various turbulence models are applied for two turbulent flows configurations; backward facing step and impinging jet, with altered Reynolds numbers and compared to experimental values. These geometrically simple test cases contain stagnation and recirculation zones, which provide stringent conditions for testing turbulence models.

5.2 Validation

5.2.1 Impinging slot jet

A single turbulent confined impinging air slot jet is numerically studied at two different Reynolds numbers and Nozzle-to-impingement surface spacing (H/W), and the Nusselt number results are compared to experimental values of Van Heiningen (1982).

Figure 5.1 shows the geometric configuration of the problem. Only the flow field of the half domain is solved due to geometric and physical symmetry of the impinging slot jet. The channel length is extended so that the flow variables become fully developed at exit plane.

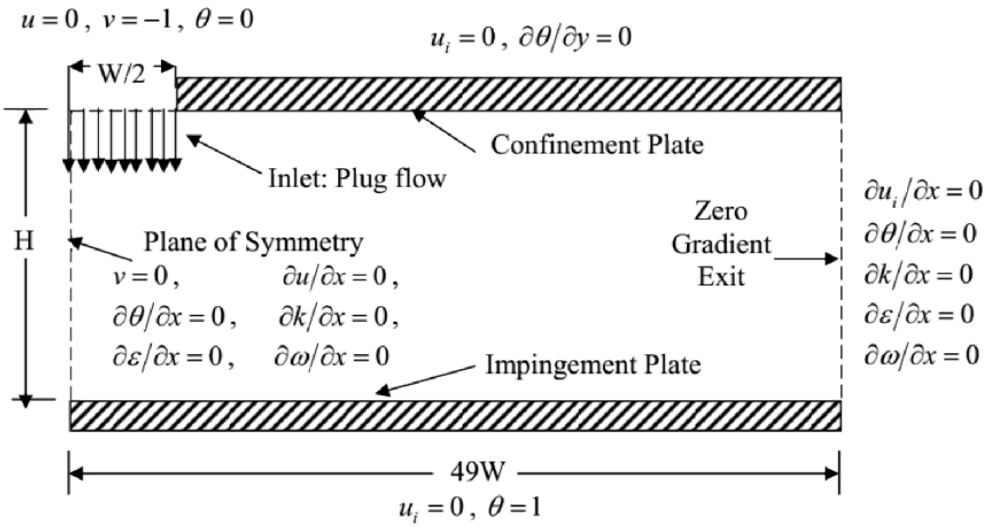

Figure 5.1: The impinging slot jet test case and boundary conditions (Heyerichs 1996)

General boundary conditions are described in Figure 5.1; however, turbulent boundary conditions relating to different models were also described previously. The bottom impinging plate is an isothermal wall of temperature 310k; a constant temperature of 300k was set on the inlet flow and top confinement wall; a uniform

velocity, turbulent kinetic energy, energy dissipation rate and temperature profiles were presumed at the nozzle exit; at outlet and symmetry planes an outflow and symmetry boundary conditions were assumed; at the confinement walls, the no-slip condition was specified. Length scale and Turbulence intensity at the nozzle exit were set to be 0.07W and 2% respectively.

For the accuracy of the results, the convergence criteria were specified as maximum residuals of momentum equations must be 10^{-6} while for turbulence equations (k, ε, ω) is 10^{-5}. To resolve the near wall region with large gradients satisfactorily, finer computational grids were set near the walls. Grid distributions are depicted in Figure 5.2 andFigure 5.3.

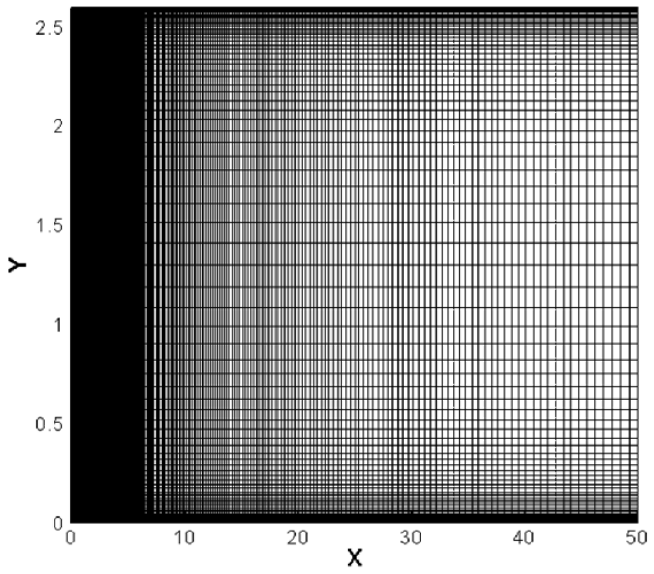

Figure 5.2: Grid distribution for Impinging slot jet H/W=2.6, 216×80 Grids

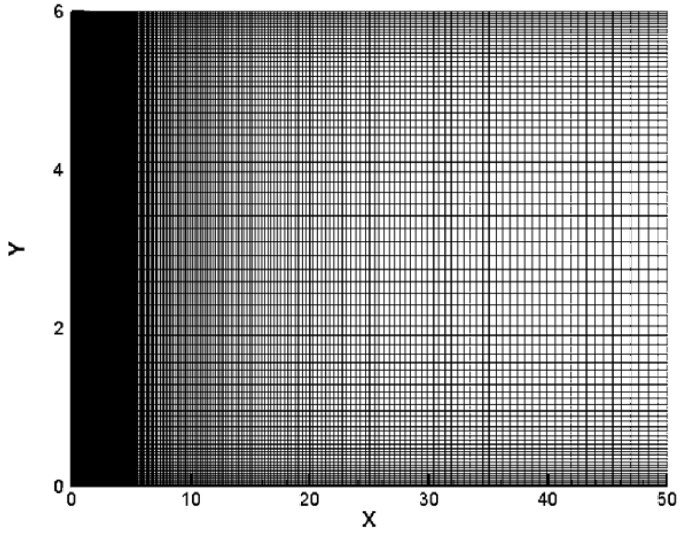

Figure 5.3: Grid distribution for Impinging slot jet H/W=6, 216×80 Grids

5.2.2 Backward facing step

Numerical computation has been performed for turbulent flow over a backward-facing step studied by Vogel and Eaton (1985) which is frequently used in benchmarking the performance of turbulence models for separating and reattaching flows. Besides, it includes a region with adverse pressure gradient and shear-layer mixing process. The computation domain was set to $35H$ in the streamwise direction. The Reynolds number based on the step height for the experiment are given as Re_H =28,000 and the expansion ratio (ER) $outlet/\text{inlet} = 1.33$. The inlet boundary layer is $\delta = 1.1H$ which is shown in Figure 5.4. No-slip condition was specified on the walls. Symmetry boundary condition was assumed at the top. Length scale and Turbulence intensity at the inlet were set to be $0.07W$ and 1% and respectively; at the exit, zero-gradient boundary conditions are assigned for temperature, velocities, and turbulent quantities.

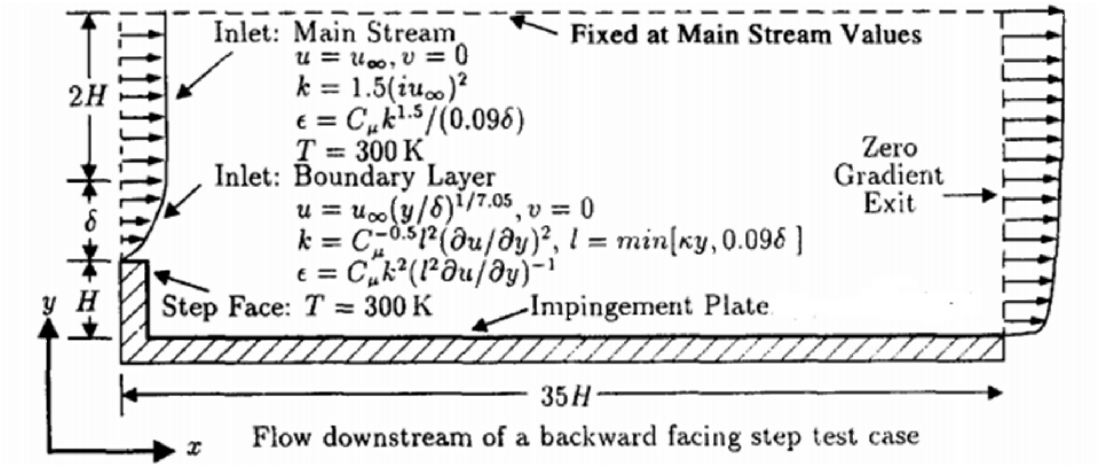

Figure 5.4: Backward facing step test case and boundary conditions (Heyerichs 1996)

For the accuracy of the results, the convergence criteria were specified the same as previous case which maximum residuals of momentum equations must be 10^{-6}, while for turbulent equations (k, ε, ω) is 10^{-5}. To resolve the near wall region with large gradients satisfactorily, the mesh has been clustered near the step end and in the recirculation region. Grid distribution is shown in Figure 5.5.

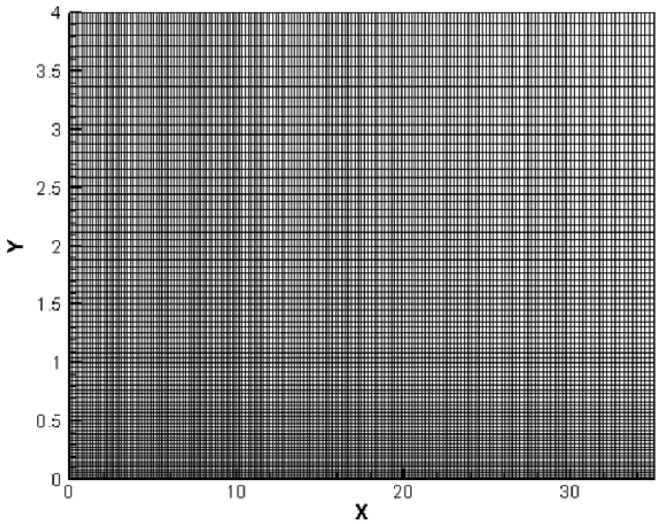

Figure 5.5: Grid distribution for Backward facing step (175×80 Grids)

5.3 Grid sensitivity analysis

To ensure the attainment of grid-independent results, the sensitivities of the numbering grids was tested for each case. Figure 5.6 toFigure 5.15 shows effects of grid sizes on the predicted Nusselt number and skin friction coefficient distribution. Typically, a grid density of 216×80 provides a satisfactory solution for the impinging slot jet model with 17280 vertices and 17573 total elements, and 175×80 is suitable for the backward facing step flow containing 14256 vertices and 14510 total elements.

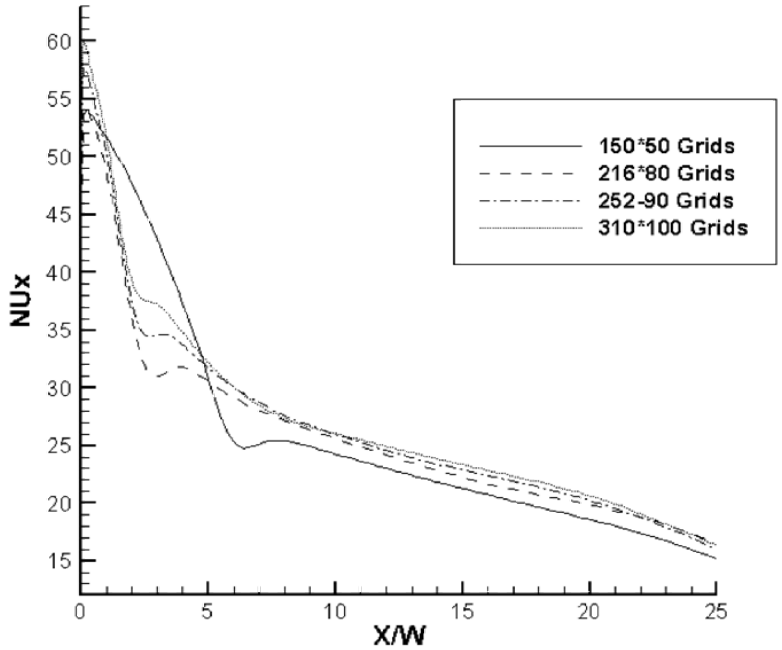

Figure 5.6: Effect of grid size on the predicted Nusselt number for Impinging jet $k-\varepsilon$ model, Re=8,100, H/W=6.

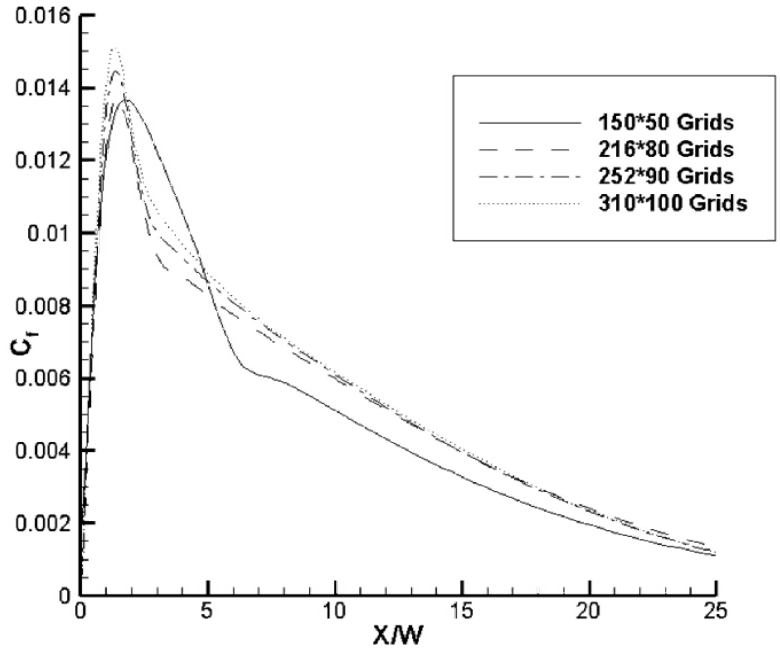

Figure 5.7: Effect of grid size on the predicted skin friction coefficient for Impinging jet $k-\varepsilon$ model, Re=8,100, H/W=6.

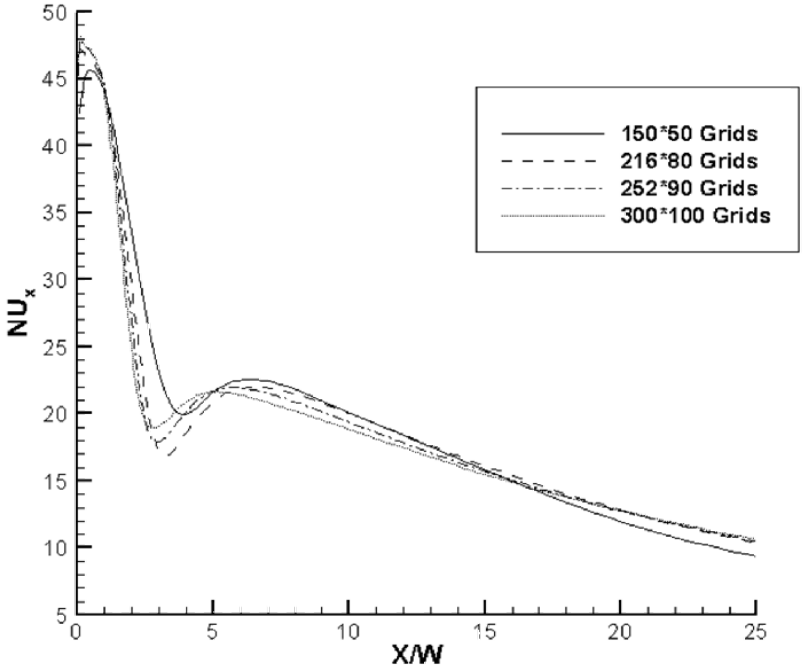

Figure 5.8: Effect of grid size on the predicted Nusselt number for Impinging jet $k-\omega$ model, Re=8,100, H/W=6.

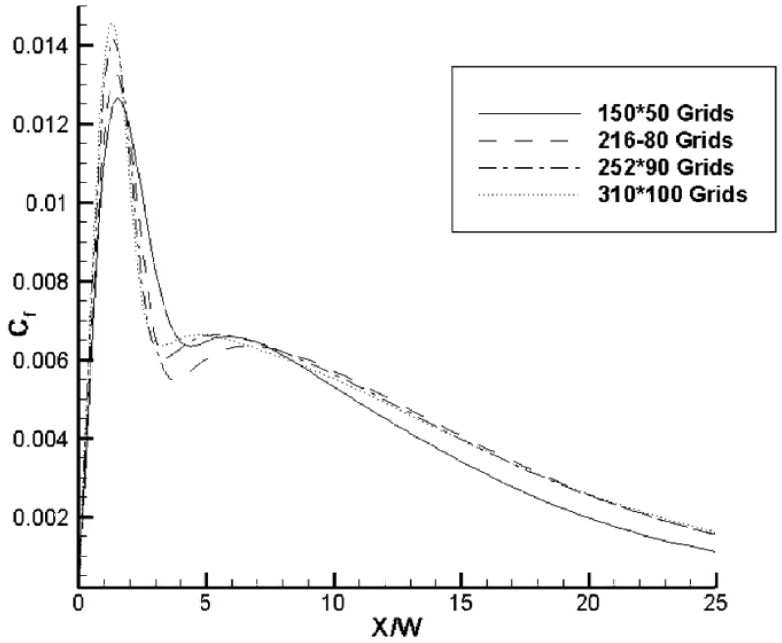

Figure 5.9: Effect of grid size on the predicted skin friction coefficient for Impinging jet $k-\omega$ model, Re=8,100, H/W=6.

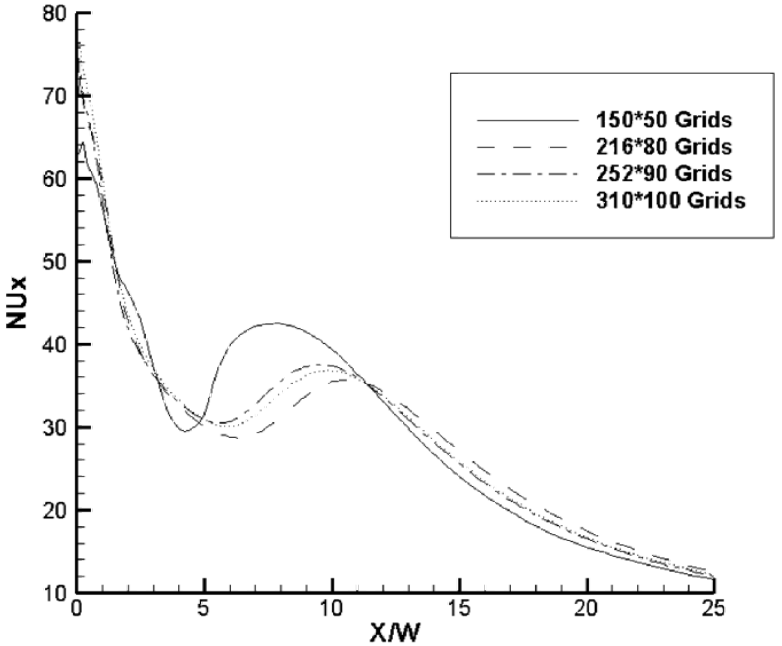

Figure 5.10: Effect of grid size on the predicted Nusselt number for Impinging jet $k-\varepsilon$ model, Re=10,400, H/W=2.6.

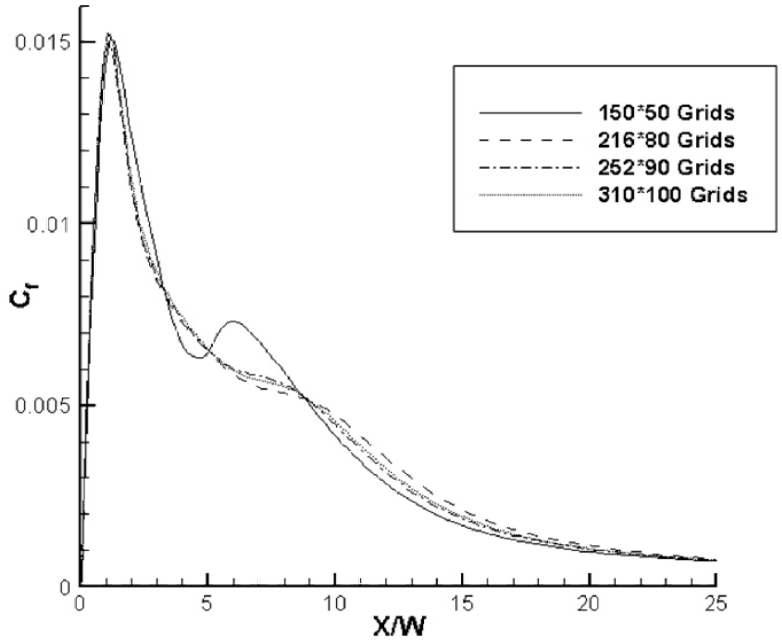

Figure 5.11: Effect of grid size on the predicted skin friction coefficient for Impinging jet $k-\varepsilon$ model, Re=10,400, H/W=2.6.

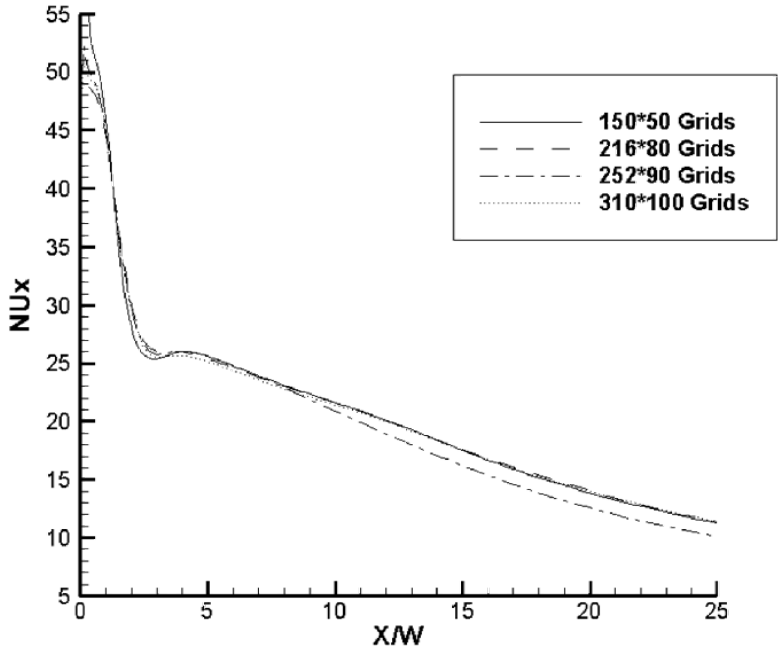

Figure 5.12: Effect of grid size on the predicted Nusselt number for Impinging jet $k-\omega$ model, Re=10,400, H/W=2.6.

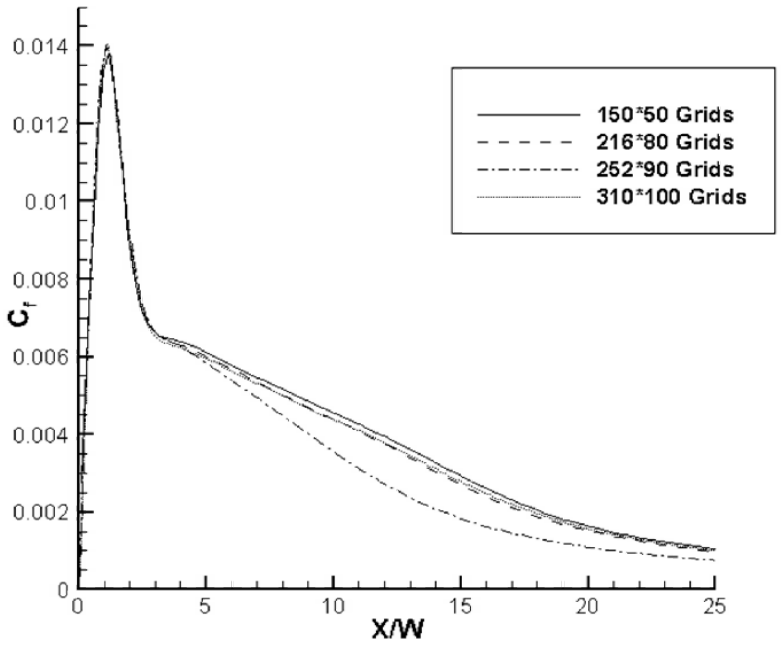

Figure 5.13: Effect of grid size on the predicted skin friction coefficient for Impinging jet $k-\omega$ model, Re=10,400, H/W=2.6.

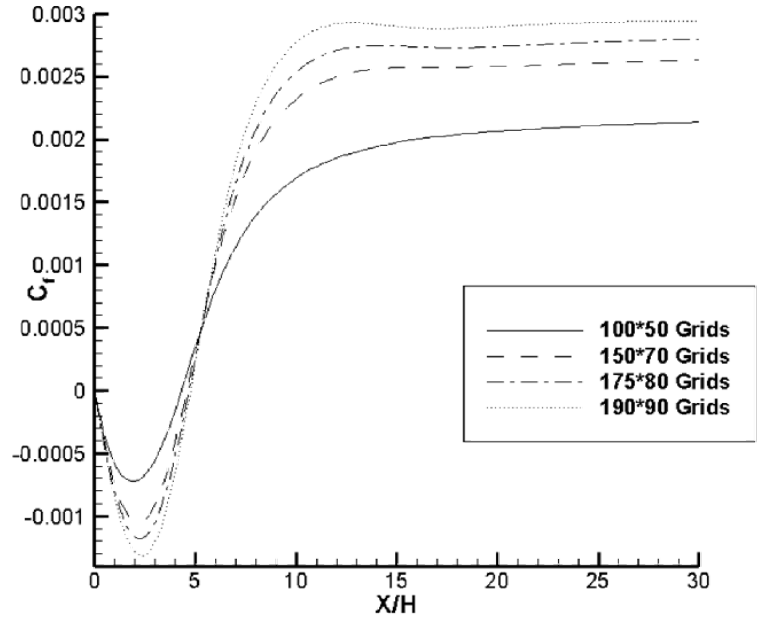

Figure 5.14: Effect of grid size on the predicted skin friction coefficient for Backward facing step $k-\varepsilon$ model, $\mathrm{Re}_H = 28,000$.

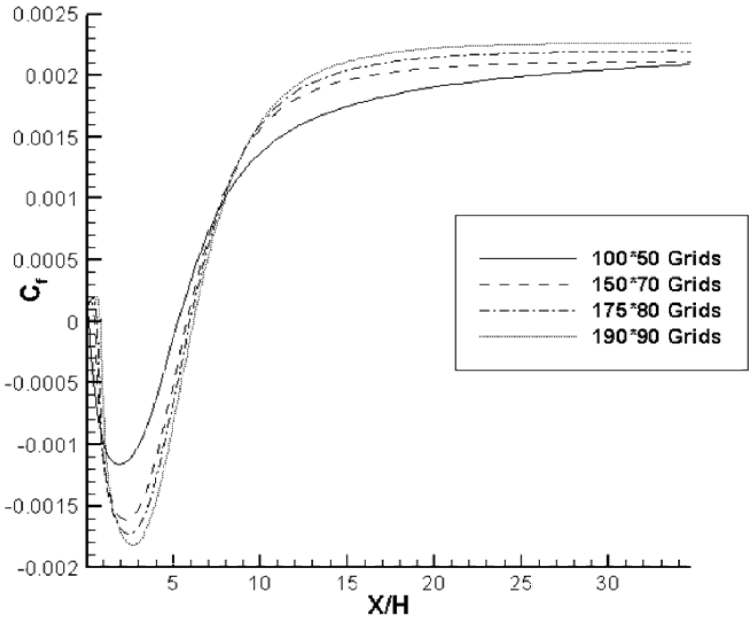

Figure 5.15: Effect of grid size on the predicted skin friction coefficient for Backward facing step $k-\omega$ model, $\mathrm{Re}_H = 28,000$.

5.4 Velocity Streamlines

5.4.1 Impinging slot jet

Two cases of experimental data of the jet impingement flows were selected from the available literature based on how detailed the authors described the experimental setup and procedures and the boundary conditions required. First case with lower nozzle to plate spacing (H/W=2.6) and $\mathrm{Re}_W = 10,400$, second one with high nozzle to plate spacing (H/W=6.0) and $\mathrm{Re}_W = 8,100$ where the Reynolds numbers are based on inlet width of the jet.

Figure 5.16 andFigure 5.17 compare the velocity streamline patterns for different turbulence models. It is observed that $k-\omega$ models predict similar reattachment lengths for the vortex at the confinement plate which is about $X \approx 20$ (for H/W=2.6) and $X \approx 40$ (for H/W=6), while $k-\varepsilon$ LB model shows this distance about $X \approx 12$ (for H/W=2.6) and $X \approx 30$ (for H/W=6). It can be realized from the streamlines that

$k-\omega$ models can predict much more efficient cooling effects of the impinging jet than low Reynolds LB $k-\varepsilon$ model.

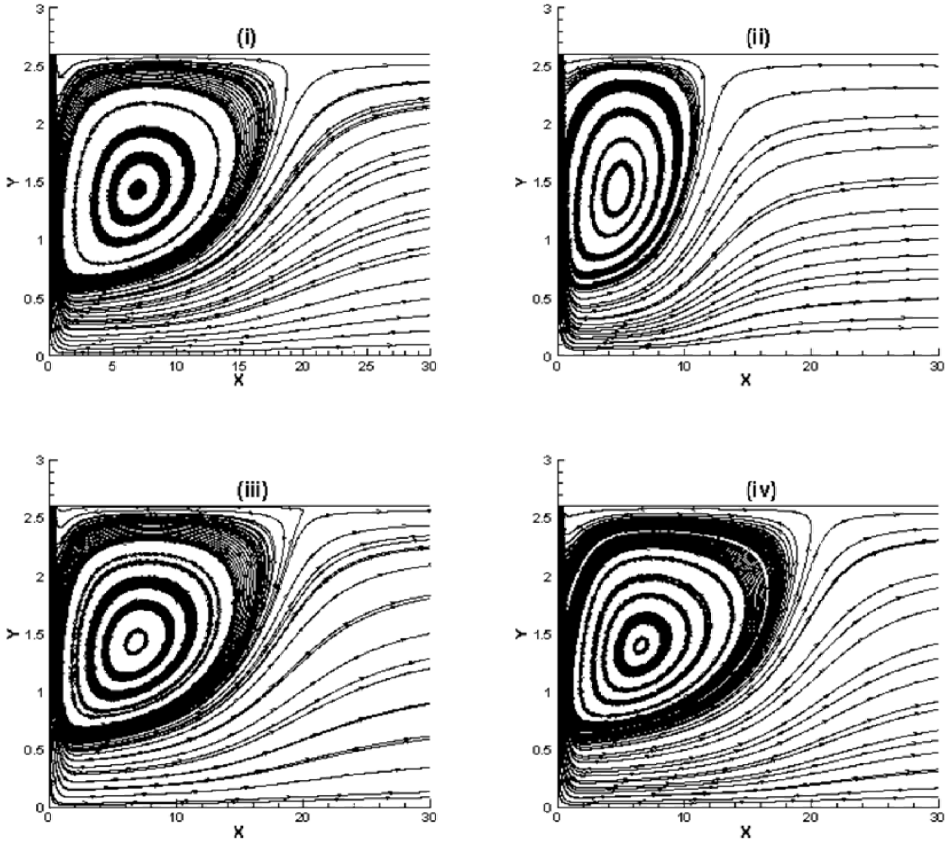

Figure 5.16: Magnified Streamlines comparison for Impinging slot jet, Re=10,400, H/W=2.6 ((i)Wilcox2006, (ii) $k-\varepsilon$ LB, (iii)Wilcox2006-LRN, (iv)Menter-SST)

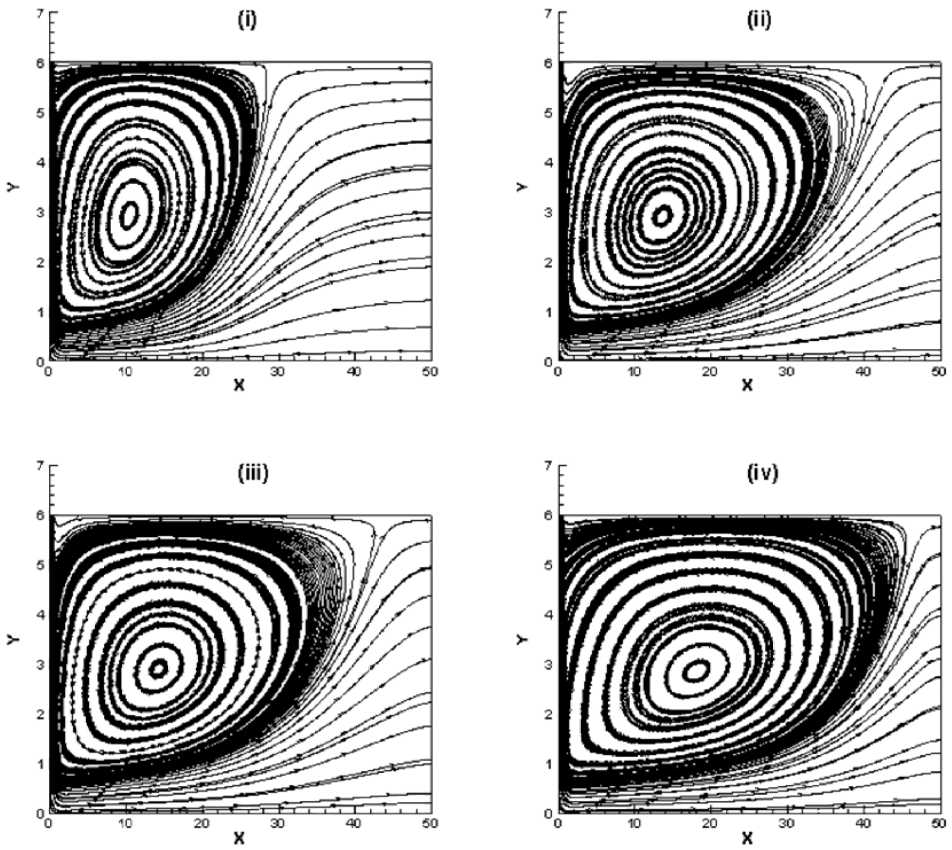

Figure 5.17: Streamlines comparison for Impinging slot jet, Re=8,100, H/W=6
((i)LB, (ii)Wilcox2006, (iii)Wilcox2006-LRN, (iv)Menter-SST)

5.4.2 Backward facing step

The backward facing step evaluates the quality of turbulence models for predicting a flow that involves reattachment of separated turbulent boundary level. All turbulence models have predicted the vortex behind the step in 2D, and the streamlines are shown in Figure 5.18.

In addition to the primary recirculation zone, there exists a secondary bubble in the step corner at approximately $0 \le X \le 1$ called as corner eddy that is hardly visible in streamlines of Figure 5.18 (iv)Menter-SST. Friedrich & Arnal (1990) reported that the rapid secondary recirculation regions located in the corner were three-dimensional bubbles.

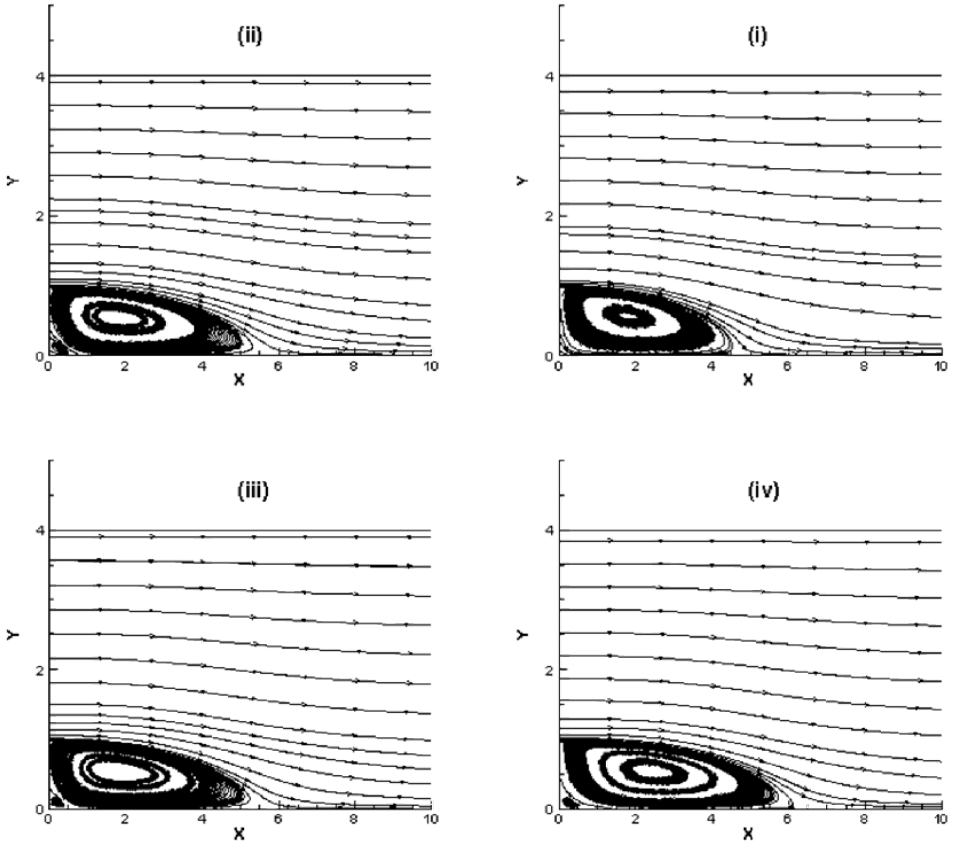

Figure 5.18: Streamlines comparison for Backward facing step, Re_H=28,000, $\delta / H = 1.1$. ((i)LB, (ii)Wilcox2006, (iii)Wilcox-LRN, (iv)Menter-SST)

5.5 Nusselt number and skin friction coefficient

5.5.1 Impinging slot jet

Figure 5.19 andFigure 5.20 compare the Nusselt numbers and friction coefficients predicted by the different turbulence models with the experimental data of Van Heiningen (1982), for first test case with Re=8,100 and H/W=6. It is observed that both Wilcox2006 and Menter of $k-\omega$ model family predict Nusselt number better in correlation with the experimental data. Although these two models slightly underpredict Nu around the secondary peak, where a boundary layer develops along the impingement plate, and is located at $X/W \approx 7$ in experimental data. The other two models (Wilcox-LRN and LB $k-\varepsilon$ model) overpredict excessively the value of the Nusselt number in the secondary peak. This is because of the fact that the

constants and the damping functions of $k-\varepsilon$ models are not tuned correctly at the wall and are tuned by free shear flow and wake flows, while $k-\omega$ family have a better agreement with the experimental data near the solid walls.

There exists a stagnation region along the impingement plate, which forms a wall jet. All models have a high correlation with the experimental data in stagnation region. At the stagnation point, $C_f = 0$ and Nu is a maximum (≈ 48). This is because of the impingement of large-scale eddies that form during jet development. Around the stagnation point, the fluid is caused to alter its direction, experiencing strong acceleration, which results in a rapid increase in C_f downstream impingement. Decreases in the values of C_f and Nu result from flow deceleration with distances farther removed from impingement with a gradual decrease with $\mathrm{Nu} \approx 15$ at $X/W \approx 20$.

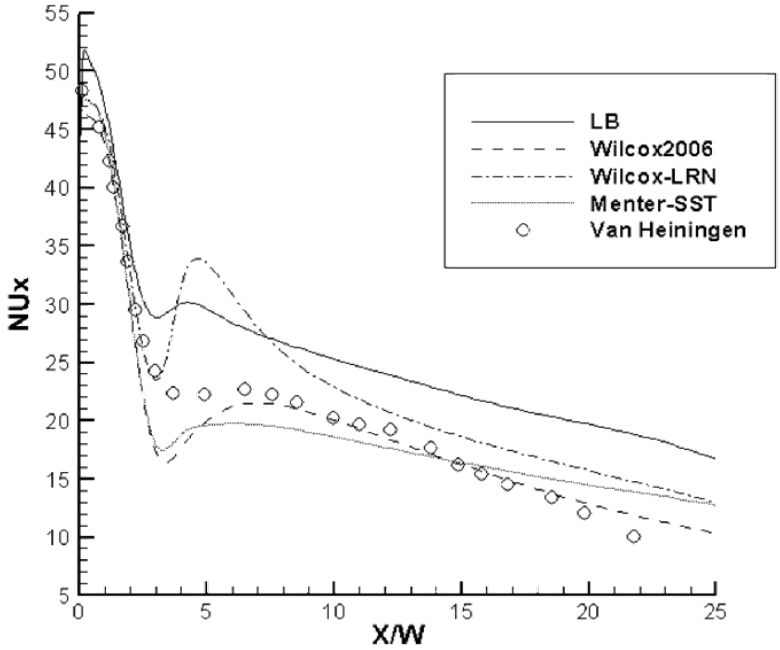

Figure 5.19: Comparison of predicted Nusselt number, Re=8,100, H/W=6.

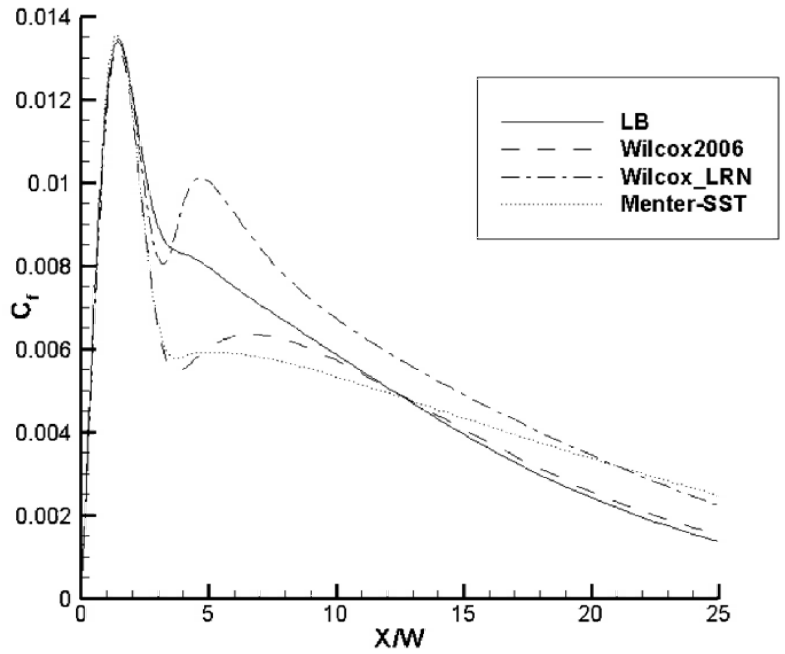

Figure 5.20: Comparison of predicted skin friction coefficient, Re=8,100, H/W=6.

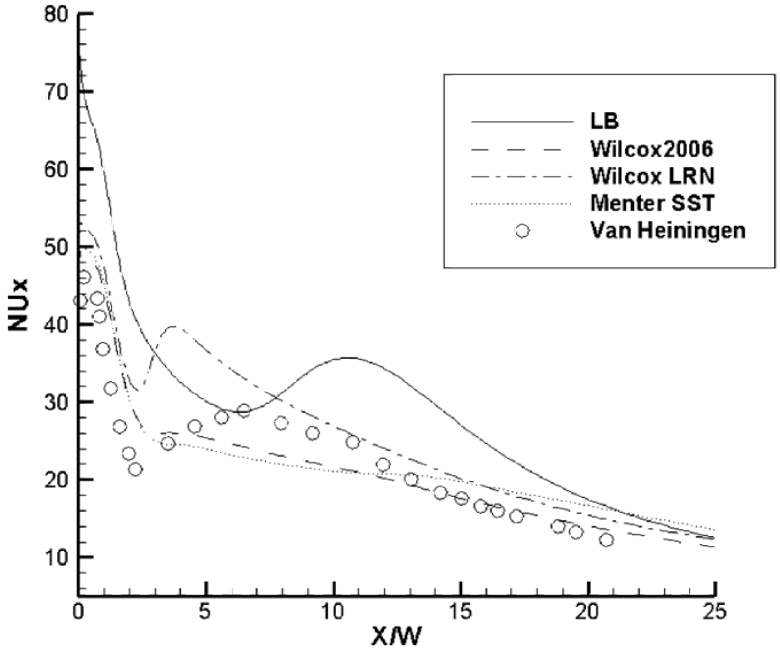

Figure 5.21: Comparison of predicted Nusselt number, Re=10,400, H/W=2.6.

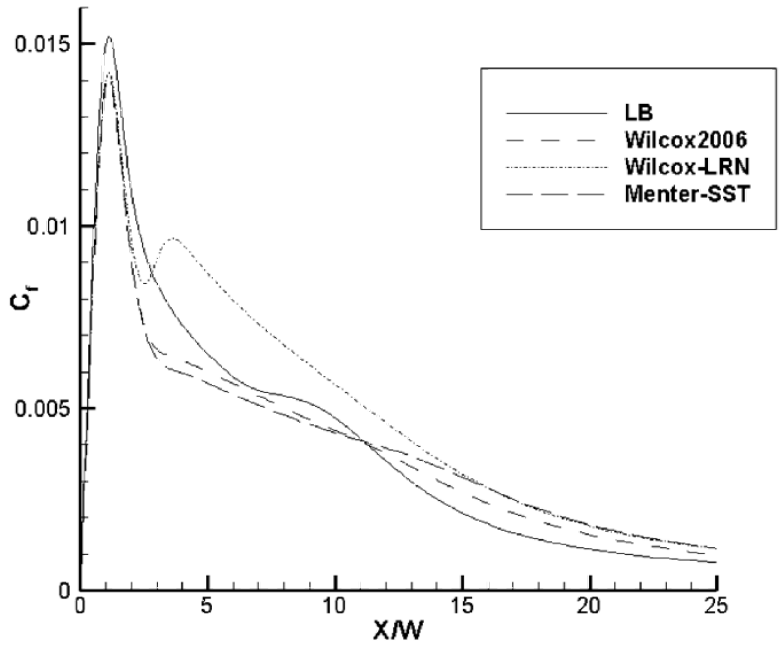

Figure 5.22: Comparison of predicted skin friction coefficient, Re=10,400, H/W=2.6.

Figure 5.19 toFigure 5.22 compare the local Nusselt numbers and friction coefficient distributions for Re=10,400, H/W=2.6 case. The results are somehow similar with the previous case that obviously Nu profile of Menter-SST $k-\omega$ model has better agreement to the data set. Lam & Bremhorst model extremely overpredicts Nu at the stagnation point. The Nu profiles might be influenced by the initial step rise and the stagnation peak is shown by the profiles in C_f diagram. Therefore, Low Reynolds number $k-\varepsilon$ model is not appropriate for heat transfer prediction near a stagnation point especially in lower distances of impingement to plate.

All models predict poorly both the magnitude and location of the secondary peak in Nu distribution; considering that the profiles of Nu and C_f are similar. Once more, Menter-SST model has the strongest correlation among others to the data set. It predicts Nu in this region better than other models while Wilcox2006 model has similar result.

Far downstream (X/W>20) the predicted C_f and Nu profiles of all models converge to a similar value. It appears that C_f and Nu predictions in this area are strongly affected by the capability of a model to catch the physical behavior upstream of this region.

The impinging slot jet test case shows that among the models taken into account; only the Menter-SST $k-\omega$ turbulent model gives a satisfying prediction of convection heat transfer in a flow deceleration. In addition, $k-\varepsilon$ low Reynolds number models that calculate the near-wall turbulence based on distance from the wall perform poorly and are not recommended for this type of flow.

5.5.2 Backward facing step

Skin-friction coefficient predictions for different models are presented in Figure 5.23. The simulated flow domain here along the wall can be divided in three general regions with alternating C_f signs: forward flow region (positive C_f, Approx. X/H>7.0); recirculation region or reverse flow (negative C_f, Approx. 0.0< X/H<6.0); secondary bubble which is not visible in LB $k-\varepsilon$ model (positive C_f, Approx. 0.0<X/H<1.0);

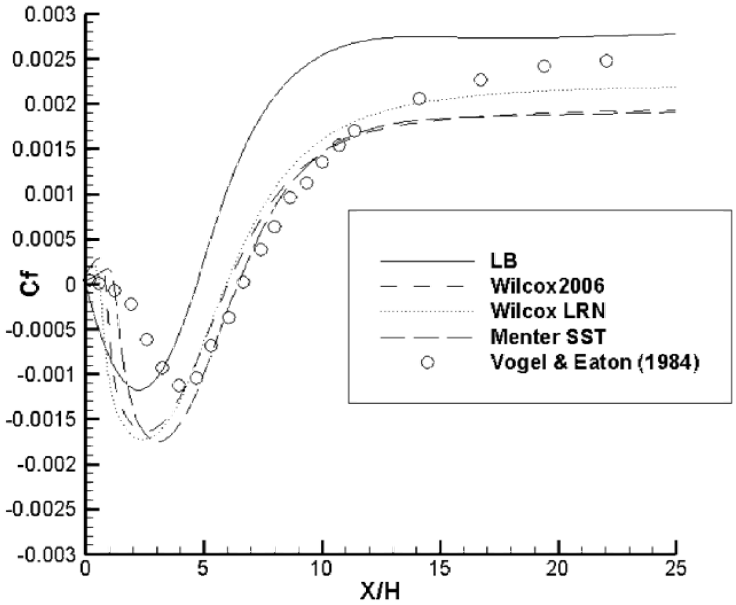

Figure 5.23: Comparison of the predicted skin friction coefficient with experimental data, $\mathrm{Re}_H = 28,000$.

Reattachment length is a commonly used parameter to determine the ability of a turbulence model for simulating the flow correctly over backward facing step. Prediction of the reattachment point is a key measure of the computational accuracy of any numerical scheme. It is the distance from the step to the position at downstream of the channel, where the velocity sign changes from negative to positive. Table 5.1 illustrates the comparison of predicted reattachment lengths by various turbulence models with the Vogel and Eaton (1984) experimental data. The experimental reattachment point is located at 6.67H downstream of separation. At reattachment C_f changes the sign from negative to zero and positive, then increases downstream.

Table 5.1: Reattachment length based on step height for different turbulence models backward facing step, $\mathrm{Re}_H = 28{,}000$

Turbulence Model Used	Reattachment length (H = step height)
LB	4.69 H
Wilcox2006	6.05 H
Wilcox LRN	5.97 H
Menter-SST	6.47 H
Experimental data (Vogel & Eaton 1984)	6.67 H

Figure 5.23 and Table 5.1 indicates that the Low Reynolds number $k-\varepsilon$ model fails to predict backward facing step flow in terms of C_f and reattachment length. It substantially overpredicts C_f after the reattachment region and underpredict in recirculating flow region. Other $k-\omega$ models have similar correlation to the data set as they have poor performance in predicting C_f in the recirculation zone. According to Table 5.1 Menter-SST model, calculates the reattachment length most accurately. All three $k-\omega$ models predict C_f well beyond reattachment along the impingement plate where a boundary layer starts to develop; however, Wilcox-LRN gives a better correlation in the redeveloping region.

The backward facing step test proves that among the test cases, $k-\omega$ models predict the flow better while Menter-SST has better correlation similar to the impinging test case while $k-\varepsilon$ models have poor prediction in both cases.

5.6 Effects of turbulence intensity

Figure 5.24 toFigure 5.33 show the effect of inlet turbulence intensity on the Nu and C_f distribution for impinging jet and backward-facing step configurations. In all cases, the turbulence intensity is varied between 1% and 8%. Mean value of 1m/s is assumed according to Figure 5.1 andFigure 5.4. All models are sensitive to turbulence intensity value. In impinging jets test cases, it is much more noticeable that in $k-\omega$ models skin friction coefficient and local Nusselt number increase around stagnation section, and the secondary peaks tend to disappear. Still, on $k-\varepsilon$ models, the change is less observable. The Nusselt number and skin friction coefficient value increases in the stagnation region until the secondary peak and right after secondary peak the values decrease. As a final point, it must be considered that in experimental measurements, the turbulent intensity can be easily determined for impinging jet cases.

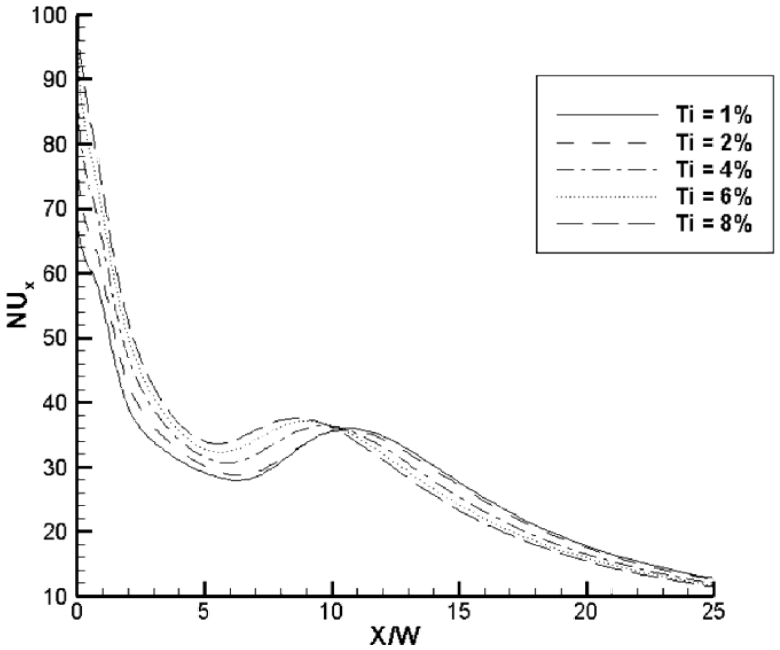

Figure 5.24: Turbulence Intensity effects on impinging slot jet Nusselt number, Re=10,400, H/W=2.6, $k-\varepsilon$ model.

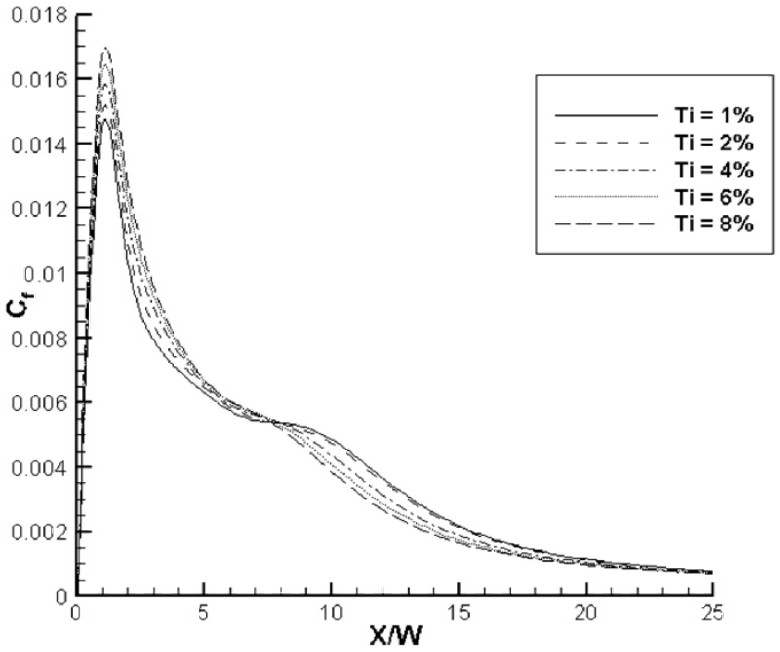

Figure 5.25: Turbulence Intensity effects on impinging slot jet skin friction coefficient, Re=10,400, H/W=2.6, $k-\varepsilon$ model.

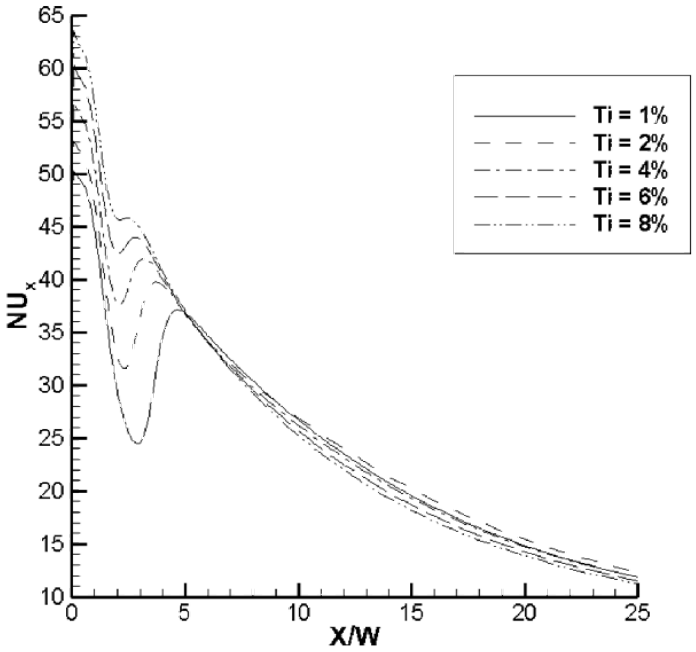

Figure 5.26: Turbulence Intensity effects on impinging slot jet Nusselt number, Re=10,400, H/W=2.6, $k-\omega$ model.

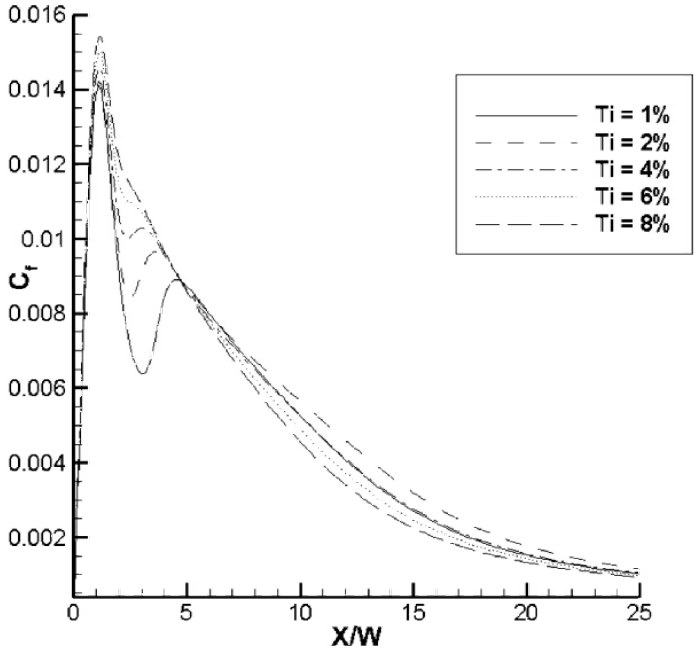

Figure 5.27: Turbulence Intensity effects on impinging slot jet skin friction coefficient, Re=10,400, H/W=2.6, $k-\omega$ model.

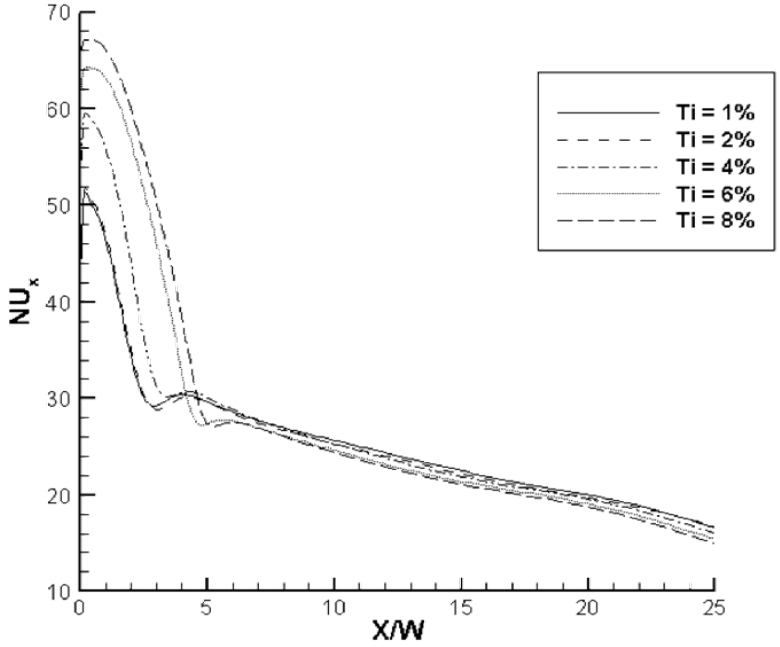

Figure 5.28: Turbulence Intensity effects on impinging slot jet Nusselt number, Re=8,100, H/W=6, $k-\varepsilon$ model.

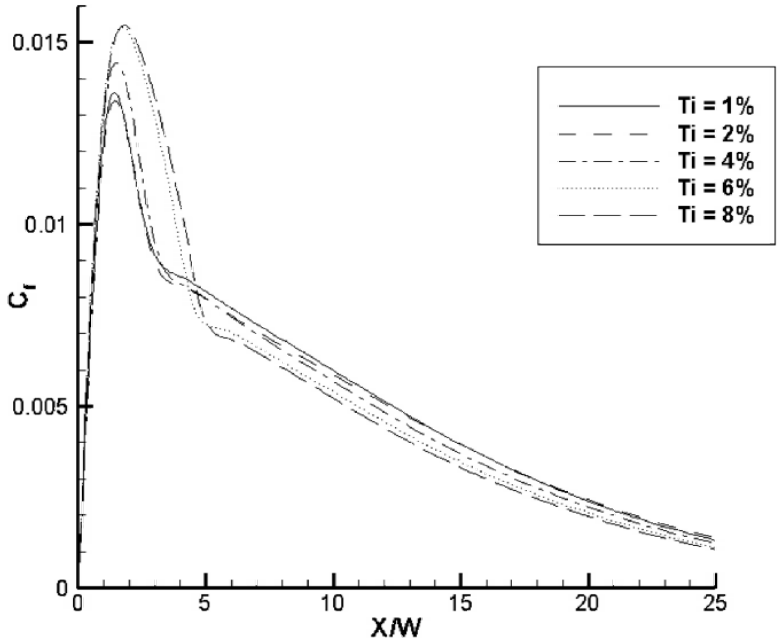

Figure 5.29: Turbulence Intensity effects on impinging slot jet skin friction coefficient, Re=8,100, H/W=6, $k-\varepsilon$ model.

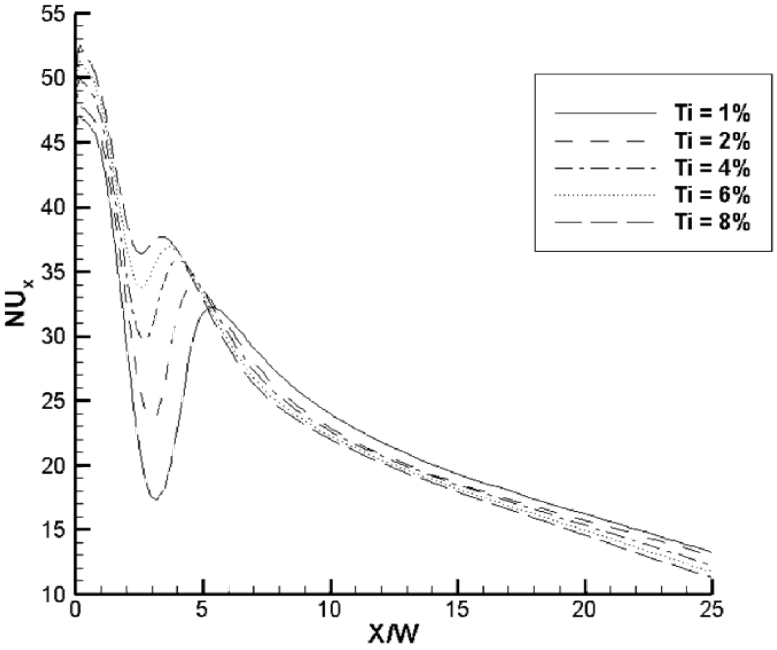

Figure 5.30: Turbulence Intensity effects on impinging slot jet Nusselt number, Re=8,100, H/W=6, $k-\omega$ model.

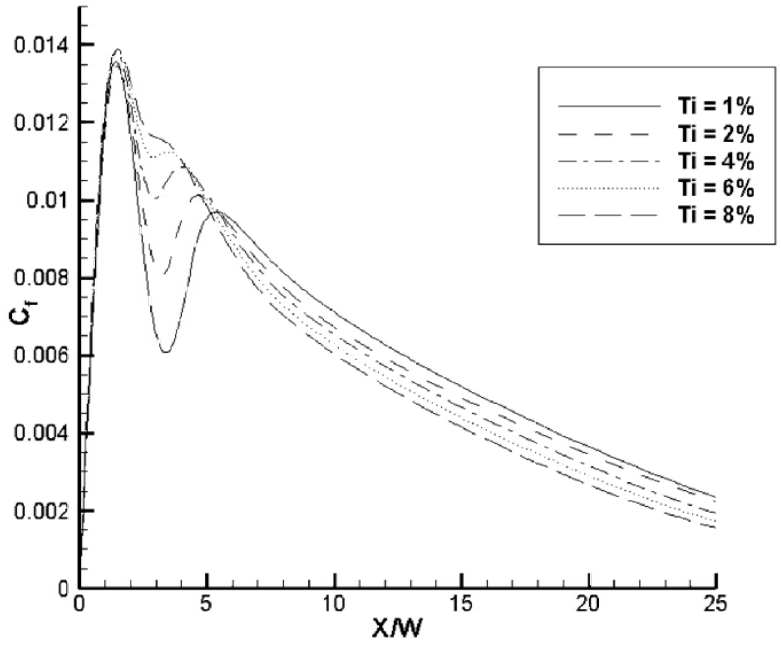

Figure 5.31: Turbulence Intensity effects on impinging slot jet skin friction coefficient, Re=8,100, H/W=6, $k-\omega$ model.

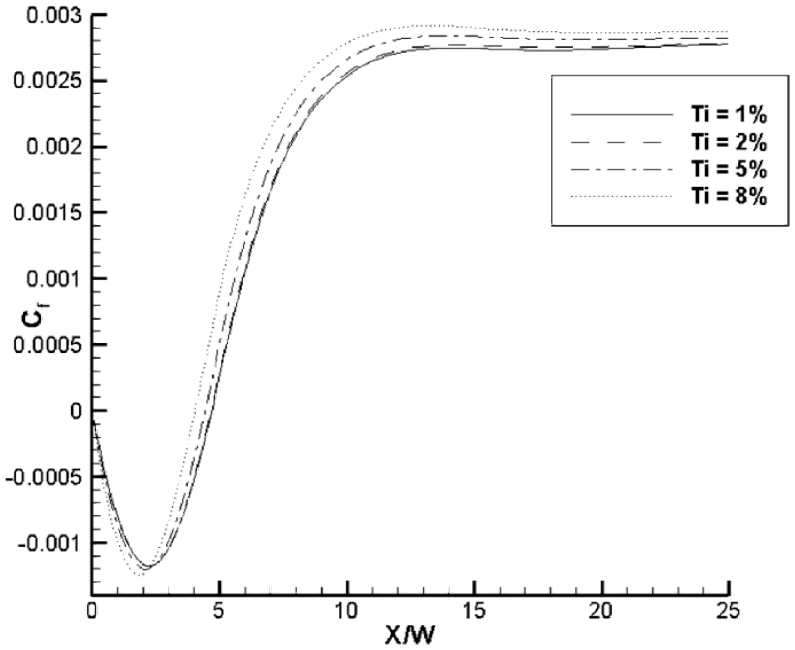

Figure 5.32: Turbulence intensity effects on backward facing step skin friction coefficient, $k-\varepsilon$ model

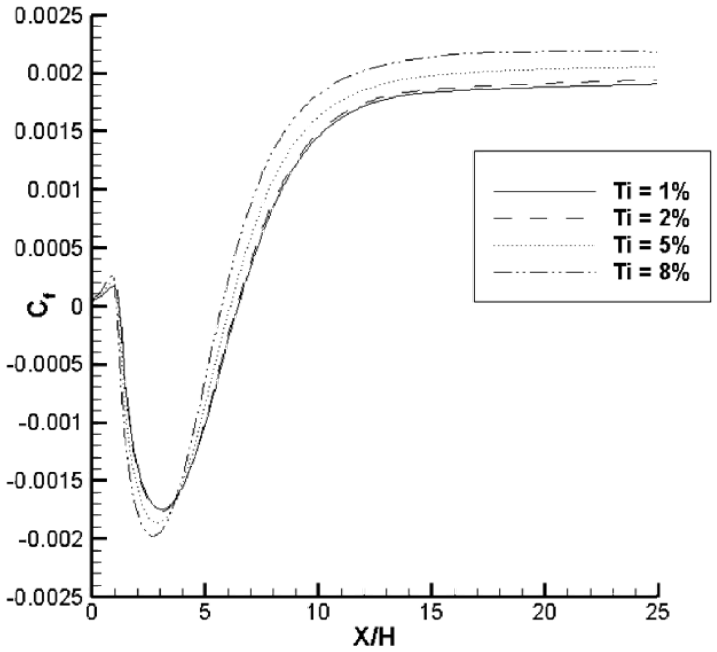

Figure 5.33: Turbulence intensity effects on backward facing step skin friction coefficient, $k-\omega$ model

In Figure 5.32 andFigure 5.33 the effects of varied T_i on friction coefficient in backward-facing step can be observed. It is clear that values of skin friction coefficient and the reattachment length are transformed as the reattachment length decreases in both $k-\varepsilon$ and $k-\omega$ models, the absolute value of skin friction increases. Finally, it is observed that in both turbulent models, turbulent intensity increments overpredict the friction factor coefficient value while underpredicting the reattachment length.

5.7 Programming consideration

As a programmer, the $k-\omega$ models have several advantages. It does not include extra terms as in $k-\varepsilon$ models. Thus, it decreases the amount of coding. The Menter-SST $k-\omega$ model converged faster than other available models. One of the reasons can be the ω-equation boundary condition (i.e. ω is static at the wall) or the reason of better performance of the damping functions used for LRN models. It is more vital in

a very close region to the wall (i.e. $y^+ < 5$ where y^+ is the dimensionless distance $y^+ = \rho u_\tau y / \mu$). The main asset of $k-\omega$ models is that the damping functions are all bounded between 'reasonable' values. Moreover, the damping function f_μ used in LB model is not bounded. In the process of solution, R_t becomes very small and this results to a greater than unity value for f_μ, which results in unrealistic values of μ_t. The boundary condition of ε-equation that is used in conjunction with LB is a zero gradient boundary condition at outlet, symmetry and solid walls. The value of ε_w is determined during the solution process and does not have the stabilizing effect of a statically fixed wall boundary condition. In addition, the LB model's f_1 term is not bounded. Therefore, f_μ become very small resulting in a large value of f_1, causing a large positive source term for ε-equation.

Chapter 6

CONCLUSION AND FUTURE WORKS

The main concern of this study is the accuracy assessment of several LRN $k-\varepsilon$ and $k-\omega$ turbulence models by various Reynolds numbers on several test cases, which are popular due to their complex separating and impinging flow characteristics using the Finite Volume Method (FVM) unstructured discretization in a FORTRAN code developed in Mechanical Engineering department. The results were compared to available experimental data. It was concluded that Menter-SST (2003) $k-\omega$ turbulence model gave better correlation in predicting of heat transfer in turbulent separating and reattaching flows compared to their related experimental data.

Menter-SST model also gives faster convergence among other models and produces less oscillation in residuals during simulation. It can be reasoned to the bounded near wall damping functions and the Dirichlet wall boundary condition applied to the ω equation.

It is also sensible that the evaluation of BFS looks somehow vague. There are some inconsistencies between shear stress wall distributions and mean velocities in some models. In details, according to skin friction data, the reattachment length is predicted as to occur at $6.05H$ for Wilcox2006 model. However, the velocity streamlines suggest this location is at approximately $5.5H$.

The schemes used here for discretizing momentum convection equations are upwind and Linear-Upwind-Differencing. These are first order schemes, and the results are not very accurate. The reason is that the turbulence models are highly unstable to higher order schemes, though using them resulted in unstable results and convergence did not occur. This problem might overcome by refining the mesh (especially in boundary layers), but it will consume more time and resources.

Compared to $k-\varepsilon$ models, implementing and programming the Wilcox $k-\omega$ model is easier, since it is not required to consider the wall shear stress, additional equation terms or distance from the wall.

Lam & Bremhorst (1981) has a poor performance in all test cases and is not recommended in these kinds of flows.

It is also planned to extend this work on Three-Dimensional models since there have been numerous new experimental data published for 3D models of these test cases and can be validated with the available code.

Additional results might also be added to the current work by varying the Reynolds number and visualizing the effects on the cases, as well as illustrating the effects of increasing or decreasing jet-to-impingement distance (H/D) on heat transfer coefficient.

The same simulations are also achieved by Ansys Fluent as the most popular commercial CFD solver to compare the results with available FORTRAN code.

Furthermore, there is an ongoing process of simulating the same models on OPENFOAM (an open source CFD solver) as future work for comparison.

A novel model, which is recently developed by F. R. Menter (2010) as the Scale Adaptive Simulation (SAS) model. The model is a transformed form of Menter-SST framework with an additional source term, which results in lower levels of eddy viscosity and leads to the resolution of turbulent fluctuations. It is of interest to assess the capabilities of this model on different complex transient models since this model is already implemented in the available FORTRAN code.

An adaptive grid system is recommended to be developed to obtain the required y^+ along the walls, or the obstacles. In addition, the stability of the multiblock grid system should be studied to secure stable convergence.

REFERENCES

Abe, K., Kondoh, T., & Nagano, Y. (1995). A new turbulence model for predicting fluid flow and heat transfer in separating and reattaching flows—II. Thermal field calculations. *International Journal of Heat and Mass Transfer*, *38*(8), 1467–1481.

Abid, R. (1993). Evaluation of two-equation turbulence models for predicting transitional flows. *International Journal of Engineering Science*, *31*(6), 831–840. doi:10.1016/0020-7225(93)90096-D

Abu-Mulaweh, H. I. (2003). A review of research on laminar mixed convection flow over backward- and forward-facing steps. *International Journal of Thermal Sciences*, *42*(9), 897–909. doi:10.1016/S1290-0729(03)00062-0

Adams, E. W., & Eaton, J. K. (1988). An LDA Study of the Backward-Facing Step Flow, Including the Effects of Velocity Bias. *Journal of Fluids Engineering*, *110*(3), 275–282. doi:10.1115/1.3243545

Adams, E. W., & Johnston, J. P. (1988). Effects of the separating shear layer on the reattachment flow structure part 2: Reattachment length and wall shear stress. *Experiments in Fluids*, *6*(7), 493–499. doi:10.1007/BF00196511

Al-aqal Osama MA. (2003). Heat transfer distributions on the walls of a narrow channel with jet impingement and cross flow. University of Pittsburgh

Anderson, J. D., & others. (1995). *Computational fluid dynamics* (Vol. 206). Springer.

Angioletti, M., Di Tommaso, R. M., Nino, E., & Ruocco, G. (2003). Simultaneous visualization of flow field and evaluation of local heat transfer by transitional impinging jets. *International Journal of Heat and Mass Transfer*, *46*(10), 1703–1713. doi:10.1016/S0017-9310(02)00479-9

Anwar-ul-Haque, F. A., Yamada, S., & Chaudhry, S. R. (2007). Assessment of Turbulence Models for Turbulent Flow over Backward Facing Step. In *Proceedings of the World Congress on Engineering* (Vol. 2). Citeseer.

Armaly, B. F., Durst, F., Pereira, J. C. F., & Schönung, B. (1983). Experimental and theoretical investigation of backward-facing step flow. *Journal of Fluid Mechanics*, *127*, 473–496. doi:10.1017/S0022112083002839

Barkley, D., Gomes, M. G. M., & Henderson, R. D. (2002). Three-dimensional instability in flow over a backward-facing step. *Journal of Fluid Mechanics*, *473*, 167–190. doi:10.1017/S002211200200232X

Behnia, M., Parneix, S., & Durbin, P. A. (1998). Prediction of heat transfer in an axisymmetric turbulent jet impinging on a flat plate. *International Journal of Heat and Mass Transfer*, *41*(12), 1845–1855. doi:10.1016/S0017-9310(97)00254-8

Behnia, M., Parneix, S., Shabany, Y., & Durbin, P. A. (1999). Numerical study of turbulent heat transfer in confined and unconfined impinging jets. *International Journal of Heat and Fluid Flow*, *20*(1), 1–9. doi:10.1016/S0142-727X(98)10040-1

Biswas, G., Breuer, M., & Durst, F. (2004). Backward-facing step flows for various expansion ratios at low and moderate Reynolds numbers. *Journal of Fluids Engineering*, *126*(3), 362–374.

Boussinesq J. 1877. Essai sur la theorie des eaux courantes. Memories presentes par divers savants a l' Academie des Sciences de l'Institut National de France XXIII.

Bradshaw, P., & Wong, F. Y. F. (1972). The reattachment and relaxation of a turbulent shear layer. *Journal of Fluid Mechanics*, *52*(01), 113–135. doi:10.1017/S002211207200299X

Bredberg, J., Peng, S.-H., & Davidson, L. (2002). An improved< i> k</i>-< i> $ømega$</i> turbulence model applied to recirculating flows. *International Journal of Heat and Fluid Flow*, *23*(6), 731–743.

C. L. M. H. Navier (1827). Mémoire sur les lois du mouvement des fluides.Mem. Acad. Sci. Inst. France 6, 38–440.

Chang, P. K., & RA, S. H. (1990). Effects of pressure gradient on reattaching flow downstream of a rearward-facing step. *Journal of Aircraft*, *27*(1), 93–95. doi:10.2514/3.45901

Chiang, T. P., & Sheu, T. W. H. (1999). A numerical revisit of backward-facing step flow problem. *Physics of Fluids (1994-Present)*, *11*(4), 862–874. doi:10.1063/1.869958

Chien, K.-Y. (1982). Predictions of Channel and Boundary-Layer Flows with a Low-Reynolds-Number Turbulence Model. *AIAA Journal*, *20*(1), 33–38. doi:10.2514/3.51043

Chiriac, V. A., & Ortega, A. (2002). A numerical study of the unsteady flow and heat transfer in a transitional confined slot jet impinging on an isothermal surface. *International Journal of Heat and Mass Transfer*, *45*(6), 1237–1248.

Craft, T. J., Launder, B. E., & Suga, K. (1996). Development and application of a cubic eddy-viscosity model of turbulence. *International Journal of Heat and Fluid Flow*, *17*(2), 108–115. doi:10.1016/0142-727X(95)00079-6

Cziesla, T., Biswas, G., Chattopadhyay, H., & Mitra, N. K. (2001). Large-eddy simulation of flow and heat transfer in an impinging slot jet. *International Journal of Heat and Fluid Flow*, *22*(5), 500–508.

David, C. (1993). Wilcox. Turbulence Modeling for CFD DCW Industries. *Inc. California*.

Davidson, L. (1990). Calculation of the turbulent buoyancy-driven flow in a rectangular cavity using an efficient solver and two different low reynolds number κ-

ε turbulence models. *Numerical Heat Transfer, Part A: Applications*, *18*(2), 129–147. doi:10.1080/10407789008944787

Downs, S. J., & James, E. H. (1987). Jet impingement heat transfer - A literature survey. In *ASME, AIChE, and ANS, 24th National Heat Transfer Conference and Exhibition* (Vol. -1).

Driver, D. M., Seegmiller, H. L., & Marvin, J. G. (1987). Time-dependent behavior of a reattaching shear layer. AIAA Journal, 25(7), 914–919.

Driver, D. M., & Seegmiller, H. L. (1985). Features of a reattaching turbulent shear layer in divergent channelflow. *AIAA Journal*, *23*(2), 163–171.

Duda, B. M., Menter, F. R., Deck, S., Bézard, H., Hansen, T., & Estève, M.-J. (2012). Application of the Scale-Adaptive Simulation to a Hot Jet in Cross Flow. *AIAA Journal*, *51*(3), 674–685.

Duda, B. M., Menter, F. R., Hansen, T., & Esteve, M. J. (2011). Scale-adaptive simulation of a hot jet in cross flow. In *Journal of Physics: Conference Series* (Vol. 318, p. 042050). IOP Publishing.

Durst, F., & Pereira, J. C. F. (1988). Time-Dependent Laminar Backward-Facing Step Flow in a Two-Dimensional Duct. *Journal of Fluids Engineering*, *110*(3), 289–296. doi:10.1115/1.3243547

Durst, F., & Tropea, C. (1981). Turbulent, backward-facing step flows in two-dimensional ducts and channels. *Proc. 3rd Int. Symp. On Turbulent Shear Flows*, 9–11.

Eaton, J. K., & Johnston, J. P. (1980). *Turbulent Flow Reattachment: An Experimental Study of the Flow and Structure Behind a Backward-facing Step*. Stanford University.

Feynman, R. P. "Turbulence theory gets a bit choppy". USA Today. September 10, 2006.

Friedrich, R., & Arnal, M. (1990). Analysing turbulent backward-facing step flow with the lowpass-filtered navier-stokes equations. *Journal of Wind Engineering and Industrial Aerodynamics*, *35*, 101–128. doi:10.1016/0167-6105(90)90212-U

Gardon, R., & Akfirat, J. C. (1966). Heat Transfer Characteristics of Impinging Two-Dimensional Air Jets. *Journal of Heat Transfer*, *88*(1), 101–107. doi:10.1115/1.3691449

Hall, S. D., & Barber, T. J. (n.d.). A Detailed CFD and Experimental Investigation of a Benchmark Turbulent Backward Facing Step Flow.

Hällqvist, T. (2006). *Large eddy simulation of impinging jets with heat transfer*. Royal Institute of Technology.

Hellsten, A. (n.d.). Some improvements in Menter's k-omega SST turbulence model. In *29th AIAA, Fluid Dynamics Conference*. American Institute of Aeronautics and Astronautics. Retrieved from http://arc.aiaa.org/doi/abs/10.2514/6.1998-2554

Heyerichs, K., & Pollard, A. (1996). Heat transfer in separated and impinging turbulent flows. *International Journal of Heat and Mass Transfer*, *39*(12), 2385–2400.

Isomoto, K., & Honami, S. (1989). The Effect of Inlet Turbulence Intensity on the Reattachment Process Over a Backward-Facing Step. *Journal of Fluids Engineering*, *111*(1), 87–92. doi:10.1115/1.3243604

Jaramillo, J. E., Perez-Segarra, C. D., Oliva, A., & Claramunt, K. (2007). Analysis of different RANS models applied to turbulent forced convection. *International Journal of Heat and Mass Transfer*, *50*(19), 3749–3766.

Jones, W. P., & Launder, B. E. (1973). The calculation of low-Reynolds-number phenomena with a two-equation model of turbulence. *International Journal of Heat and Mass Transfer*, *16*(6), 1119–1130. doi:10.1016/0017-9310(73)90125-7

Jongebloed, L. (2008). *Numerical study using FLUENT of the separation and reattachment points for backwards-facing step flow*. Rensselaer Polytechnic Institute.

Jovic, S., & Driver, D. (1995). Reynolds number effect on the skin friction in separated flows behind a backward-facing step. *Experiments in Fluids*, *18*(6), 464–467.

Jovic, S., & Driver, D. M. (1994). *Backward-facing step measurements at low Reynolds number, Re(sub h)=5000*. Retrieved from http://ntrs.nasa.gov/search.jsp?R=19940028784

Kaiktsis, L., Karniadakis, G. E., & Orszag, S. A. (1991). Onset of three-dimensionality, equilibria, and early transition in flow over a backward-facing step. *Journal of Fluid Mechanics*, *231*, 501–528. doi:10.1017/S0022112091003488

Katti, V., & Prabhu, S. V. (2008). Experimental study and theoretical analysis of local heat transfer distribution between smooth flat surface and impinging air jet from a circular straight pipe nozzle. *International Journal of Heat and Mass Transfer*, *51*(17), 4480–4495.

Kim, J., Kline, S. J., & Johnston, J. P. (1980). Investigation of a reattaching turbulent shear layer: flow over a backward-facing step. *Journal of Fluids Engineering*, *102*(3), 302–308.

Kobayashi, T., & Kitoh, K. (1992). *A Review of CFD Methods and Their Application to Automobile Aerodynamics* (SAE Technical Paper No. 920338). Warrendale, PA: SAE International. Retrieved from http://papers.sae.org/920338/

Krishnamoorthy, C. (2007). *Numerical Analysis of Backward-facing Step Flow Preceeding a Porous Medium Using FLUENT*. ProQuest.

Kuehn, D. A. D. (1980). Effects of Adverse Pressure Gradient on the Incompressible Reattaching Flow over a Rearward-Facing Step. *AIAA Journal*, *18*(3), 343–344. doi:10.2514/3.50765

Lam, C. K. G., & Bremhorst, K. (1981). A Modified Form of the k-ε Model for Predicting Wall Turbulence. *Journal of Fluids Engineering*, *103*(3), 456–460. doi:10.1115/1.3240815

Lan, H., Armaly, B. F., & Drallmeier, J. A. (2009). Three-dimensional simulation of turbulent forced convection in a duct with backward-facing step. *International Journal of Heat and Mass Transfer*, *52*(7), 1690–1700.

Le, H., Moin, P., & Kim, J. (1997). Direct numerical simulation of turbulent flow over a backward-facing step. *Journal of Fluid Mechanics*, *330*, 349–374.

Lee, J., & Lee, S.-J. (2000). The effect of nozzle configuration on stagnation region heat transfer enhancement of axisymmetric jet impingement. *International Journal of Heat and Mass Transfer*, *43*(18), 3497–3509.

Lien, F. S., & Leschziner, M. A. (1994). Assessment of turbulence-transport models including non-linear rng eddy-viscosity formulation and second-moment closure for flow over a backward-facing step. *Computers & Fluids*, *23*(8), 983–1004. doi:10.1016/0045-7930(94)90001-9

Liu, X., Lienhard, V., J. H., & Lombara, J. S. (1991). Convective Heat Transfer by Impingement of Circular Liquid Jets. *Journal of Heat Transfer*, *113*(3), 571–582. doi:10.1115/1.2910604

Looney, M. K., & Walsh, J. J. (1984). Mean-flow and turbulent characteristics of free and impinging jet flows. *Journal of Fluid Mechanics*, *147*, 397–429. doi:10.1017/S0022112084002147

Mangani, L., & Bianchini, C. (2007). Heat transfer applications in turbomachinery. In *Proceedings of the OpenFOAM International Conference. OpenFOAM Conference, London, Reino Unido*.

Mani, M., Ladd, J. A., & Bower, W. W. (2004). Rotation and curvature correction assessment for one-and two-equation turbulence models. *Journal of Aircraft*, *41*(2), 268–273.

Martin, H. (1977). Heat and Mass Transfer between Impinging Gas Jets and Solid Surfaces. In James P. Hartnett and Thomas F. Irvine (Ed.), *Advances in Heat Transfer* (Vol. Volume 13, pp. 1–60). Elsevier. Retrieved from http://www.sciencedirect.com/science/article/pii/S0065271708702211

Menter, F., Ferreira, J. C., Esch, T., & Konno, B. (2003). The SST turbulence model with improved wall treatment for heat transfer predictions in gas turbines. In *Proceedings of the international gas turbine congress* (pp. 2–7).

Menter, F. R. (1992). Improved two-equation k-omega turbulence models for aerodynamic flows. *NASA STI/Recon Technical Report N*, *93*, 22809.

Menter, F. R. (1992). Influence of freestream values on k-omega turbulence model predictions. *AIAA Journal*, *30*(6), 1657–1659.

Menter, F. R. (1994). Two-equation eddy-viscosity turbulence models for engineering applications. *AIAA Journal*, *32*(8), 1598–1605.

Menter, F. R. (2009). Review of the shear-stress transport turbulence model experience from an industrial perspective. *International Journal of Computational Fluid Dynamics*, *23*(4), 305–316.

Menter, F. R., & Egorov, Y. (2010). The Scale-Adaptive Simulation Method for Unsteady Turbulent Flow Predictions. Part 1: Theory and Model Description. *Flow, Turbulence and Combustion*, *85*(1), 113–138. doi:10.1007/s10494-010-9264-5

Menter, F. R., Kuntz, M., & Langtry, R. (2003). Ten years of industrial experience with the SST turbulence model. *Turbulence, Heat and Mass Transfer*, *4*, 625–632.

Morgans, R. C., Dally, B. B., Nathan, G. J., Lanspeary, P. V., & Fletcher, D. F. (1999). Application of the revised Wilcox (1998) k-$ømega$ turbulence model to a jet in co-flow. In *Second International Conference on CFD in the Mineral and Process Industries, Melbourne, Australia*.

Nagano, Y., & Kim, C. (1988). A Two-Equation Model for Heat Transport in Wall Turbulent Shear Flows. *Journal of Heat Transfer*, *110*(3), 583–589. doi:10.1115/1.3250532

Nagano, Y., & Tagawa, M. (1990). An Improved k-ε Model for Boundary Layer Flows. *Journal of Fluids Engineering*, *112*(1), 33–39. doi:10.1115/1.2909365

O'Donovan, T. S. (2005). Fluid flow and heat transfer of an impinging air jet. *Department of Mechanical and Manufacturing Engineering*, 145.

Ötügen, M. V. (1991). Expansion ratio effects on the separated shear layer and reattachment downstream of a backward-facing step. *Experiments in Fluids*, *10*(5), 273–280. doi:10.1007/BF00202460

P. Y. Tzeng, C. D. H., C. Y. Soong. (1999). Numerical Investigation of Heat Transfer Under Confined Impinging Turbulent Slot Jets. *Numerical Heat Transfer, Part A: Applications*, *35*(8), 903–924. doi:10.1080/104077899274976

Papadopoulos, G., & Ötügen, M. V. (1995). Separating and Reattaching Flow Structure in a Suddenly Expanding Rectangular Duct. *Journal of Fluids Engineering*, *117*(1), 17–23. doi:10.1115/1.2816809

Park, T. H., Choi, H. G., Yoo, J. Y., & Kim, S. J. (2003). Streamline upwind numerical simulation of two-dimensional confined impinging slot jets. *International Journal of Heat and Mass Transfer*, *46*(2), 251–262.

Park, T. S., & Sung, H. J. (1995). A nonlinear low-Reynolds-number κ-ε model for turbulent separated and reattaching flows—I. Flow field computations. *International Journal of Heat and Mass Transfer*, *38*(14), 2657–2666. doi:10.1016/0017-9310(95)00009-X

Polat, S., Huang, B., Mujumdar, A. S., & Douglas, W. J. M. (1989). Numerical flow and heat transfer under impinging jets: A review. *Annual Review of Heat Transfer*, *2*(2), 157–197. doi:10.1615/AnnualRevHeatTransfer.v2.60

Popovac, M., & Hanjalic, K. (2007). Compound wall treatment for RANS computation of complex turbulent flows and heat transfer. *Flow, Turbulence and Combustion*, *78*(2), 177–202.

Rajasekaran, J. (2011). *On the flow characteristics behind a backward-facing step and the design of a new axisymmetric model for their study*. University of Toronto.

Roos, F. W., & Kegelman, J. T. (1986). Control of coherent structures in reattaching laminar and turbulent shear layers. *AIAA Journal*, *24*(12), 1956–1963. doi:10.2514/3.9553

Saad, Y. (2003). *Iterative methods for sparse linear systems*. Siam.

Sahoo, D., & Sharif, M. A. R. (2004). Mixed-convective cooling of an isothermal hot surface by confined slot jet impingement. *Numerical Heat Transfer, Part A: Applications*, *45*(9), 887–909.

Scarano, F., & Riethmuller, M. L. (1999). Iterative multigrid approach in PIV image processing with discrete window offset. *Experiments in Fluids*, *26*(6), 513–523. doi:10.1007/s003480050318

Seyedein, S. H., Hasan, M., & Mujumdar, A. S. (1994). Modelling of a single confined turbulent slot jet impingement using various< i> k</i>—ϵ turbulence models. *Applied Mathematical Modelling*, *18*(10), 526–537.

Sezai, I. (2013, May). Implementation of boundary conditions. Mechanical Engineering Department, Eastern Mediterranean University.

Sezai, I., & Mohamad, A. A. (1999). Three-Dimensional Simulation of Laminar Rectangular Impinging Jets, Flow Structure, and Heat Transfer. *Journal of Heat Transfer*, *121*(1), 50–56. doi:10.1115/1.2825965

Sharif, M. A. R., & Mothe, K. K. (2009). Evaluation of turbulence models in the prediction of heat transfer due to slot jet impingement on plane and concave surfaces. *Numerical Heat Transfer, Part B: Fundamentals*, *55*(4), 273–294.

Shi, Y., Ray, M. B., & Mujumdar, A. S. (2002). Computational Study of Impingement Heat Transfer under a Turbulent Slot Jet. *Industrial & Engineering Chemistry Research*, *41*(18), 4643–4651. doi:10.1021/ie020120a

Sinha, S. N., Gupta, A. K., & Oberai, M. (1981). Laminar separating flow over backsteps and cavities. I - Backsteps. *AIAA Journal*, *19*(12), 1527–1530. doi:10.2514/3.7885

Sivasamy, A., Selladurai, V., & Rajesh Kanna, P. (2007). Numerical simulation of two-dimensional laminar slot-jet impingement flows confined by a parallel wall. *International Journal for Numerical Methods in Fluids*, *55*(10), 965–983.

Sjolander, R. L. S., & Langtry, R. (2002). Prediction of transition for attached and separated shear layers in turbomachinery. In *38 th AIAA/ASME/SAE/ASEE Joint Propulsion Conference and Exhibit, Indianapolis, IN*.

Smirnov, P. E., & Menter, F. R. (2009). Sensitization of the SST turbulence model to rotation and curvature by applying the Spalart–Shur correction term. *Journal of Turbomachinery*, *131*(4), 041010.

Spalart, P. R., & Rumsey, C. L. (2007). Effective inflow conditions for turbulence models in aerodynamic calculations. *AIAA Journal*, *45*(10), 2544–2553.

Sparrow, E. M., & Wong, T. C. (1975). Impingement transfer coefficients due to initially laminar slot jets. *International Journal of Heat and Mass Transfer*, *18*(5), 597–605. doi:10.1016/0017-9310(75)90271-9

Stevens, J., & Webb, B. W. (1991). Local Heat Transfer Coefficients Under an Axisymmetric, Single-Phase Liquid Jet. *Journal of Heat Transfer*, *113*(1), 71–78. doi:10.1115/1.2910554

Sundén, B. (2001). Numerical investigation of impingement heat transfer using linear and nonlinear two-equation turbulence models. *Numerical Heat Transfer: Part A: Applications*, *40*(6), 563–578.

Thangam, S., & Hur, N. (1991). A highly-resolved numerical study of turbulent separated flow past a backward-facing step. *International Journal of Engineering Science*, *29*(5), 607–615. doi:10.1016/0020-7225(91)90065-B

Thangam, S., & Knight, D. D. (1989). Effect of stepheight on the separated flow past a backward facing step. *Physics of Fluids A: Fluid Dynamics (1989-1993)*, *1*(3), 604–606. doi:10.1063/1.857430

Thangam, S., & Speziale, C. G. (1992). Turbulent flow past a backward-facing step - A critical evaluation of two-equation models. *AIAA Journal*, *30*(5), 1314–1320. doi:10.2514/3.11066

Tylli, N. (2003). *Induced Global Unsteadiness and Sidewall Effects in the Backward-facing Step Flow: Experiments and Numerical Simulations*.

Van Heiningen, A. R. (1984). *Heat transfer under an impinging slot jet*.

Van Heiningen, A. R. P., Mujumdar, A. S., & Douglas, W. J. M. (1976). Numerical prediction of the flow field and impingement heat transfer caused by a laminar slot jet. *Journal of Heat Transfer*, *98*(4), 654–658.

Versteeg, H. K., & Malalasekera, W. (2007). *An introduction to computational fluid dynamics: the finite volume method*. Pearson Education.

Vieser, W., Esch, T., & Menter, F. (2002). Heat transfer predictions using advanced two-equation turbulence models. *CFX Validation Report. CFX-VAL*, *10*, 1002.

Vishnuvardhanarao, E., & Das, M. K. (2007). Computation of mean flow and thermal characteristics of incompressible turbulent offset jet flows. *Numerical Heat Transfer, Part A: Applications*, *53*(8), 843–869.

Vogel, J. C. (1984). *Heat Transfer and Fluid Mechanics Measurements in the Turbulent Reattaching Flow Behind a Backward-facing Step*. Stanford University.

Vogel, J. C., & Eaton, J. K. (1985). Combined Heat Transfer and Fluid Dynamic Measurements Downstream of a Backward-Facing Step. *Journal of Heat Transfer*, *107*(4), 922–929. doi:10.1115/1.3247522

Wang, S. J., & Mujumdar, A. S. (2005). A comparative study of five low Reynolds number< i> k</i>–< i> ε</i> models for impingement heat transfer. *Applied Thermal Engineering*, *25*(1), 31–44.

Westphal, R. V., & Johnston, J. P. (1984). Effect of initial conditions on turbulent reattachment downstream ofa backward-facing step. *AIAA Journal*, *22*(12), 1727–1732. doi:10.2514/3.8844

Wilcox, D. A. (1994). Simulation of transition with a two-equation turbulence model. *AIAA Journal*, *32*(2), 247–255.

Wilcox, D. C. (1988). Reassessment of the scale-determining equation for advanced turbulence models. *AIAA Journal*, *26*(11), 1299–1310.

Wilcox, D. C. (2008). Formulation of the kw Turbulence Model Revisited. *AIAA Journal*, *46*(11), 2823–2838.

Williams, P. T., & Baker, A. J. (1997). Numerical simulations of laminar flow over a 3D backward-facing step. *International Journal for Numerical Methods in Fluids*, *24*(11), 1159–1183. doi:10.1002/(SICI)1097-0363(19970615)24:11<1159::AID-FLD534>3.0.CO;2-R

Yin. Y., Nagano, Y., and Tsuji, T., 1990, "Numerical prediction of turbulent convection boundary lines," Heat Transfer : Japanese Rresearch. Vol.19, #6.pp. 584-601.

Zuckerman, N., & Lior, N. (2006). Jet impingement heat transfer: Physics, correlations, and numerical modeling. *Advances in Heat Transfer*, *39*(06), 565–631.